01 Oct 2019

ASACUSA PROPOSAL FOR ELENA

Plans for experiments during LS2 and in the ELENA era

CERN-SPSC-2019-035 / SPSC-P-307-ADD-2
01/10/2019

ASACUSA collaboration

C. Amsler[a], D. Barna[b], H. Breuker[c], M. Fleck[c,d], A. Gligorova[a], H. Higaki[e], M. Hori[f*], Y. Kanai[g], B. Kolbinger[a], N. Kuroda[d], A. Lanz[a], M. Leali[h], E. Lodi-Rizzini[h], V. Mäckel[c], C. Malbrunot[i], V. Mascagna[j], Y. Matsuda[d], D. J. Murtagh[a], Y. Nagata[k], A. Nanda[a], L. Nowak[i], N. Ogawa[f,l], M. C. Simon[a], M. Tajima[g], Y. Tanaka[m], S. Ulmer[c], U. Uggerhøj[n], L. Venturelli[h], E. Widmann[a*], A. Weiser[a], T. Wolz[i], Y. Yamazaki[c], J. Zmeskal[a]

[a]Stefan Meyer Institute, [b]Wigner Research Centre for Physics, [c]Ulmer Fundamental Symmetries Laboratory, RIKEN, [d]Institute of Physics, the University of Tokyo, [e]Graduate School of Advanced Sciences of Matter, Hiroshima University, [f]Max-Planck-Institut für Quantenoptik, [g]Nishina Center for Accelerator-Based Science, RIKEN, [h]Dipartimento di Ingegneria dell'Informazione, Università degli Studi di Brescia, and INFN, [i]Experimental Physics Department, CERN [j]Dipartimento di Scienza e Alta Tecnologia, Università degli Studi dell'Insubria and INFN, [k]Department of Physics, Tokyo University of Science, [l]Department of Physics, The University of Tokyo, [m]GSI Helmholtzzentrum für Schwerionenforschung, [n]Department of Physics and Astronomy, Aarhus University
* Co-spokespersons

Executive summary

The ELENA era marks a new phase for the ASACUSA collaboration. The leap forward is made possible by the new availability of electron-cooled beams of 100 keV antiprotons with a small emittance and energy spread which will be transported to two beamlines in our experimental area. The latter allows the permanent installation of the antiprotonic helium and antihydrogen spectroscopy experiments. The resulting continuous availability of the installations for off-line R&D will allow a more rapid progress than before.

Antiprotonic helium ($\overline{p}\mathrm{He}^+$) atoms containing a helium nucleus, a ground-state electron, and an antiproton in a Rydberg state constitutes the hadron-antihadron quantum bound system with the longest experimentally-known lifetime. We propose to utilize the unprecedented high-quality beam provided by ELENA to carry out sub-Doppler two-photon laser spectroscopy and measure the energy intervals of several heretofore unobserved transitions in $\overline{p}^3\mathrm{He}^+$ and $\overline{p}^4\mathrm{He}^+$ of especially narrow natural width to a fractional precision of $\sim 10^{-11}$. For this a spectroscopy technique involving five laser beams will be used. This enables us to test the calculations of quantum electrodynamics (QED) which remains the most accurately understood variety of relativistic quantum field theory that forms the basis of the Standard Model. This will yield a precise value of the (anti)proton-to-electron mass ratio that forms the basis of the International System of Units, as well as a test of the consistency of CPT symmetry in a hadron-antihadron system. The spectroscopic data can also be used to establish upper limits on some beyond-the-Standard-Model physics such as fifth forces that may arise at Angstrom length scales or exotic spin-dependent forces mediated by unknown spin-0 or spin-1 bosons with eV-scale masses. In the latter phases of the project, we will utilize an induction decelerator to slow down the antiprotons, and experimental techniques to cool down the temperature of the $\overline{p}\mathrm{He}^+$ to sub-Kelvin temperatures. The latest advances in metrological laser techniques will be employed. This is an evolutive effort of many years to understand the systematic effects of the measurement. Various enhancements to the experiment may in principle even allow us to reach an even higher precision in the far future.

For the **Cusp** experiment aiming at the formation of a polarized antihydrogen beam to perform hyperfine spectroscopy in a field-free region, we plan the following:

- The overall goal of the experiment is to perform a ppm-scale measurement of the antihydrogen ground-state hyperfine structure using Rabi spectrometry in run 3, and 10 ppb using the Ramsey technique during run 4.
- In order to advance the experiment, three postdoctoral researchers will be stationed permanently at CERN. Two positions are currently open for recruitment.
- Several hardware upgrades will be performed: the positron source will be replaced by a commercial source contributed by Aarhus University. The cold bore and multi-ring electrodes (MRE) trap in the Cusp mixing magnet will be upgraded to reach lower temperatures, better control of trap potentials, a larger solid angle for the spectroscopy apparatus, and optical access for deexcitation studies using photons. The antihydrogen detector will be upgraded to improve the differentiation between low-field seekers (signal) and high-field seekers (background) annihilating close to the central BGO calorimeter.

- During LS2, antihydrogen formation ("mixing") studies will be carried out using matter. To this end a proton source will be installed, Rydberg hydrogen that is formed will be detected by a MCP. This will allow us to test several mixing schemes. The principal quantum number distribution will be measured using an existing field ionizer.

- In three-body recombination, the temperature of positrons is a crucial parameter for the formation rate and ground-state fraction of (anti)hydrogen. A measurement scheme for positrons has been implemented, the temperature will be lowered to $\sim$ 20 K by evaporative cooling. This is expected to significantly increase the (anti)hydrogen formation rate and ground-state fraction.

- To further increase of the ground-state fraction, two deexcitation schemes are going to be tested: deexcitation with a plasma and photon-stimulated deexcitation.

- Funding will be applied to construct a reservoir trap for antiprotons to allow for a more flexible usage in mixing schemes.

- In parallel to experiments in the ELENA area, studies using the hydrogen beam in Bat. 275 will continue. Experiments will be performed measuring coefficients of the non-minimal SME for the first time. The Ramsey method of separated oscillatory fields will be implemented and tested with hydrogen and deuterium, to have a setup ready for antihydrogen in run 4. In addition excited hydrogen beams will be used for testing detection schemes used for off-line mixing with matter and to investigate the proposed deexcitation methods for Rydberg antihydrogen.

- The implementation of a reservoir trap for antiprotons, if funded, would open up the possibility of installing a permanent slow-extraction beam line. As a first step, the studies of antiproton annihilation in various targets that we have donee in the last years could continue. On the longer term, other experiments needing continuous beam, e.g. measurements of Pontecorvo reactions or of X-ray spectroscopy of antiprotonic atoms for QED studies, could be added, provided a community can be formed to bring in the necessary personnel and equipment.

Contents

Part I
ASACUSA experimental area with ELENA

The ASACUSA area for the ELENA era will undergo significant changes due to the fact that two beam lines will be available. This allows for the permanent installation of both the antiprotonic helium setup (upstream) as well as the Cusp experiment aiming at formation of an antihydrogen beam for hyperfine spectroscopy (downstream). This will allow for a permanent installation of all the experimental equipment. Especially for the antihydrogen experiment it will be a game changer, as before the complex multi-trap system had to be disassembled and reassembled on a yearly basis, and was not available outside of beam time periods for R&D. From now on the apparatus can be installed permanently at the beam position, allowing a more solid grounding and cabling scheme than before. Also, the setup will available for the whole year for development work, except for the time when CERN services are shut down for maintenance. The continuous accessibility of the apparatus will allow much faster progress than before, a fact that we plan to exploit during LS2 in studies with matter as outlined in Part II.

The layout of the area is shown in Fig. 1. The new beamlines are drawn on green (antiprotonic helium) and purple (Cusp experiment). The existing Cusp apparatus is drawn in red, comprising the $\overline{\mathrm{p}}$ catching trap MUSASHI, the mixing trap Cusp, a new positron source provided by Aarhus University, and the hyperfine spectroscopy beam line consisting of a microwave cavity, a sextupole magnet, and our antihydrogen detector. In orange a new reservoir trap is shown, described in sec. 5.3.4, that we plan to construct in the shutdown between 2021 and 2022 if the necessary funding can be secured. It would make use of an existing superconducting magnet, requiring only manpower and modest investment. The reservoir trap would greatly improve the flexibility in implementing mixing schemes. In addition it would allow to install a permanent beam line for slow extracted antiprotons discussed in sec. 9.

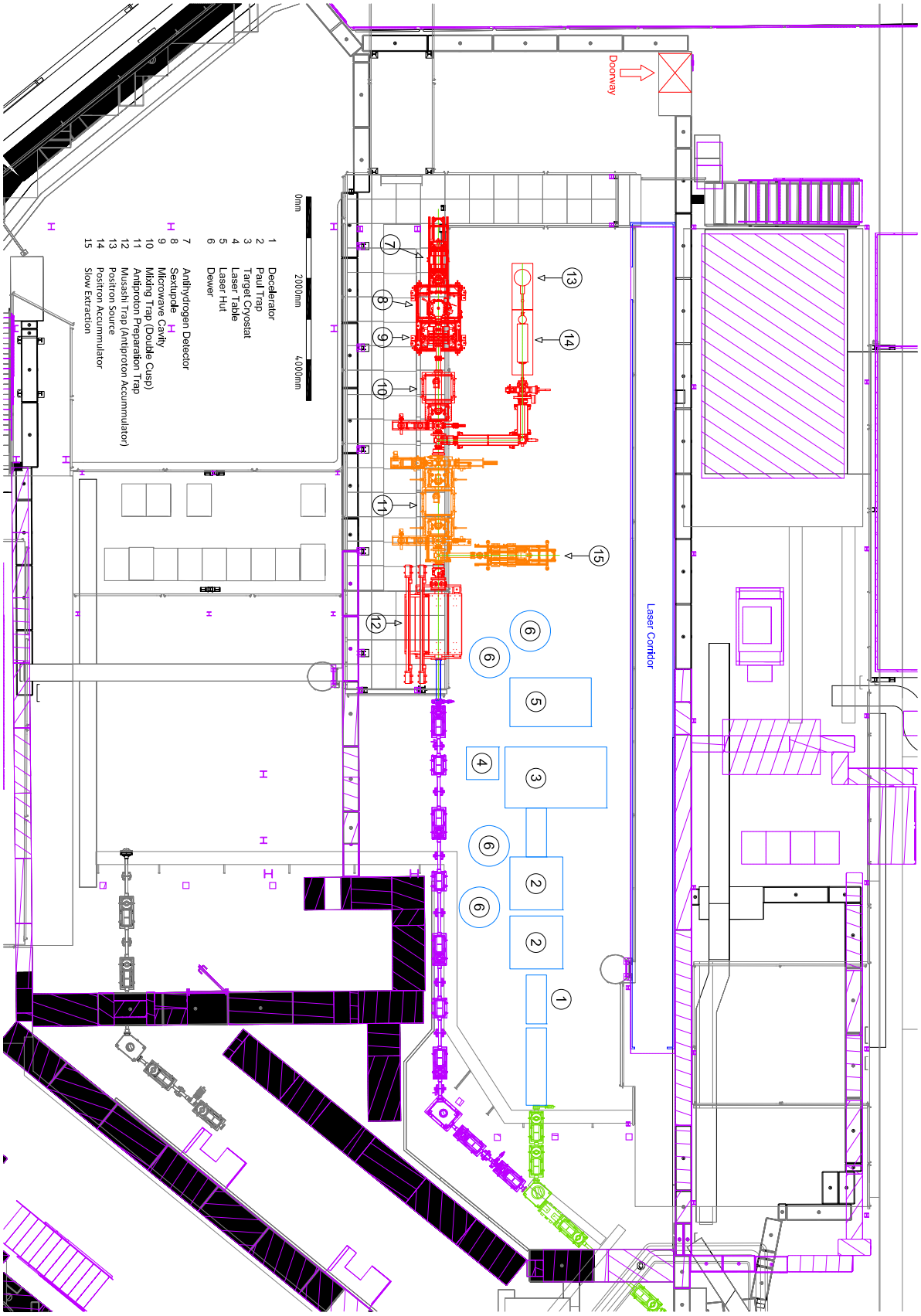

Figure 1 – ASACUSA area layout for ELENA.

Part II
Antiprotonic Helium

1 Physics case

1.1 Introduction

Metastable antiprotonic helium ($\overline{p}\mathrm{He}^+ \equiv \overline{p} + \mathrm{He}^{2+} + e^-$ (see Fig. 2) is a three-body exotic atom that contains a helium nucleus, an electron occupying the 1s state, and an antiproton in a Rydberg state of large principal ($n \sim 38$) and orbital angular momentum ($\ell \sim n-1$) quantum numbers [1–6]. Whereas spectroscopy of antihydrogen atoms [7, 8] probes the interaction between an antihadron and antilepton, the $\overline{p}\mathrm{He}^+$ atom is a **hadron-antihadron quantum bound system having the longest known lifetime**, and remains an important complementary atom for high-precision spectroscopic study [9, 10] in the ELENA era (Fig. 3).

We propose [11] to utilize the unprecedented high-quality beam provided by ELENA to carry out sub-Doppler two photon laser spectroscopy of narrow resonances of $\overline{p}\mathrm{He}^+$. The motivations for this experiment include,

1. **Tests of three-body quantum electrodynamics (QED) calculations at $\sim 10^{-11}$ scale precision.** QED remains the most accurately understood variety of relativistic quantum field theory that forms the basis of the Standard Model. Along with H_2^+ and HD^+ molecular ions [12–14], $\overline{p}\mathrm{He}^+$ is among the small number of fundamental three-body atoms composed of two heavy particles that have been precisely studied by theory and by laser spectroscopy. Its transition frequencies ν_{exp} have so far been measured to a fractional precision of $(2.3-16)\times 10^{-9}$, and this has agreed with the QED values. Whereas a priori QED calculations of the 1s-2s energy interval of (anti)hydrogen currently have a precision of better than $\sim 1\times 10^{-10}$ that is limited by the so-called "proton size puzzle", i.e., the $\sim 4\%$ uncertainty on the known proton charge radius r_p [15–17] that must be included as a parameter, the transition frequencies of $\overline{p}\mathrm{He}^+$ are far less sensitive ($\sim 10^{-12}$) to the uncertainty that arises from the antiproton charge radius $r_{\overline{p}}$ [2, 3]. This is due to the fact that the antiproton and electron orbitals in the atom repel each other and do not strongly overlap. This insensitivity to $r_{\overline{p}}$ removes the dominant source of uncertainty in the QED calculations and allows us to potentially test the accuracy of higher-order corrections. Recent estimations indicate that the transition frequencies of $\overline{p}\mathrm{He}^+$ may in a few years be calculated to a precision of $\sim 6\times 10^{-12}$, which is > 400 times better

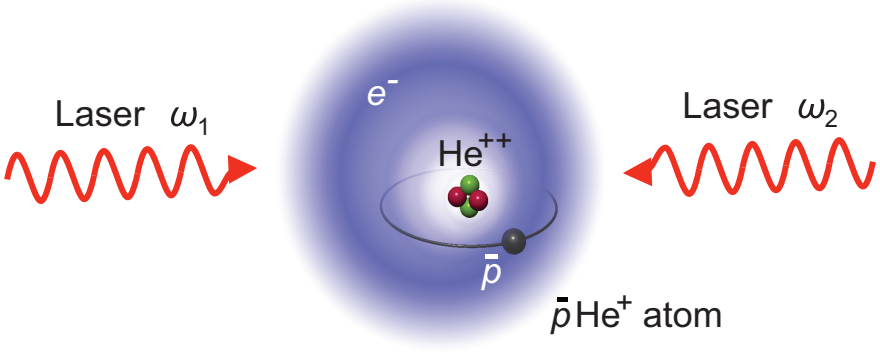

Figure 2 – Schematic drawing of a $\overline{p}\mathrm{He}^+$ atom excited by two counter-propagating laser beams of optical frequencies ω_1 and ω_2.

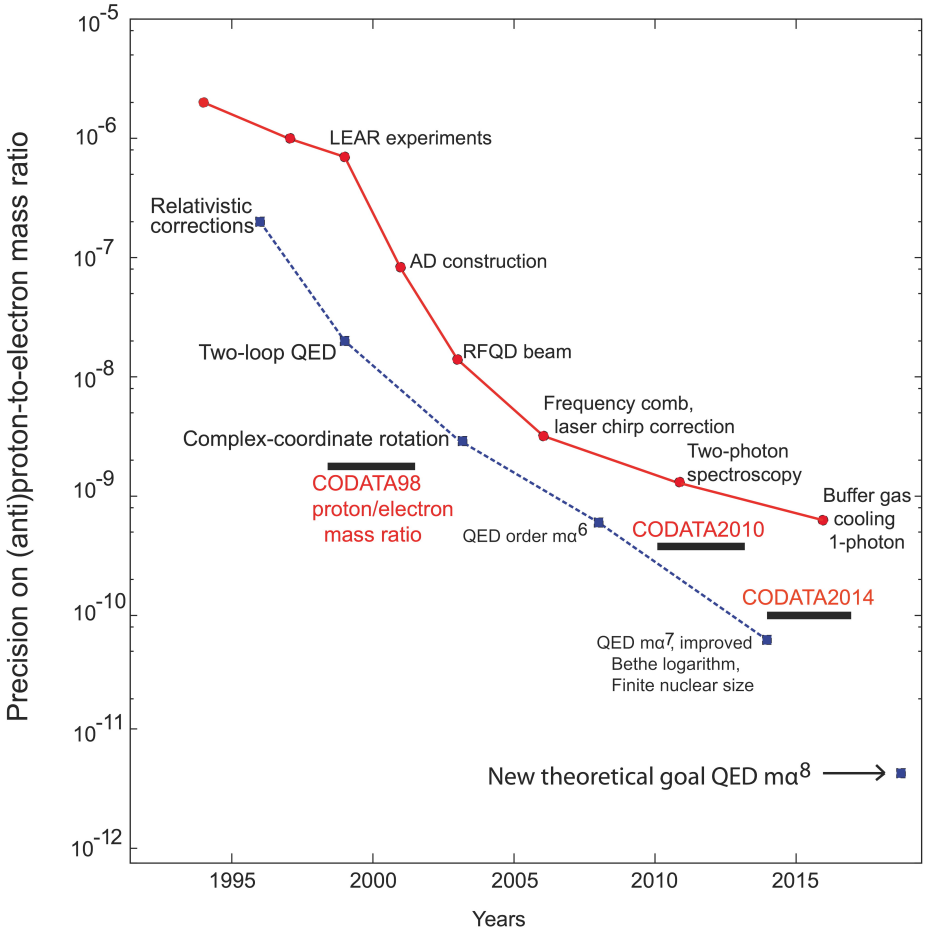

Figure 3 – Experimental precision on the antiproton-to-electron mass ratio determined by laser spectroscopy of $\overline{p}\mathrm{He}^+$ over the years (solid red line), compared with the uncertainty of theoretical QED calculations (broken blue line). The theoretical precision on the $\overline{p}\mathrm{He}^+$ transition frequencies are expected to reach $\sim 6 \times 10^{-12}$ within a few years. This corresponds to a factor > 400 higher precision compared to the best published results of ASACUSA in 2016.

than our experimental results that have been published so far in 2016 [9]. This motivates us to further improve the experiment.

2. **Determination of the antiproton-to-electron mass ratio to $\sim 10^{-11}$ precision.** The proton-to-electron mass ratio M_p/m_e, together with the fine structure constant α, is one of the dimensionless fundamental constants of nature which can be measured to especially high precision and forms the basis of the International System of Units [18, 19]. The latest Penning trap experiments [20, 21] have determined the ratio as $M_p/m_e = 1836.152673346(81)$. Due to its importance M_p/m_e should be measured using as many independent methods as possible. Since atomic mass is defined relative to the mass of a ^{12}C atom, such a measurement can also be regarded as the determination of the electron mass. Our past ASACUSA experiments by comparison have determined the antiproton-to-electron mass ratio as $M_{\overline{p}}/m_e = 1836.1526734(15)$. We propose to improve this precision to $\sim 10^{-11}$, though it is hard to predict what new systematic errors can arise, and things must proceed over many years in a step-by-step manner as we learn to use the new ELENA machine. This should

then rival the best determinations of M_p/m_e from Penning trap experiments and provide an important consistency test.

3. **Test of CPT symmetry in a bound hadron-antihadron system.** Spectroscopy of $\overline{p}\mathrm{He}^+$ also provides a consistency test of CPT symmetry in a hadron-antihadron system. The atomic transition frequencies ν_{exp} measured by ASACUSA are proportional to $Q_{\overline{p}}^2 M_{\overline{p}}$, wherein the cyclotron frequency of a single antiproton confined in a Penning trap measured by the BASE and TRAP experiments have a dependency $\propto Q_{\overline{p}}/M_{\overline{p}}$ [22–24]. By combining the results from these two types of experiments [25], we have set an upper limit of 5×10^{-10} on any deviation between the proton and antiproton masses and charges [9]. We plan to greatly improve this limit using ELENA.

4. **Fifth forces at Angstrom length scales.** The $\overline{p}\mathrm{He}^+$ data can also be used to set upper limits on any hypothetical fifth forces that may arise between hadrons and antihadrons at atomic length scales between $l = 10^{-11}$ and 10^{-9} m [26–28]. This Angstrom scale lies between the sub-picometer ranges that are explored by collider experiments, and the nanometer-to-micron scale ranges probed by experiments that utilize the Casimer force or cryogenic cantilevers of high sensitivity.

5. **Upper limits on exotic velocity and spin-dependent, semi-leptonic forces** that may arise between antihadrons and electrons [29,30] due to axions or other undiscovered spin-0 or spin-1 bosons such as familons, Majorons, or arions. A non-zero coupling of these hypothetical particles to normal leptons or quarks may give rise to anomalous dipolar interactions. The typical Angstrom-scale distances between the constituent particles make atoms particularly sensitive to the virtual exchange of such exotic bosons if they should exist in the mass range $m = 0.01$–1000 eV. There is recent interest in using high precision spectroscopy of atoms and molecules to indirectly constrain the bosons' couplings. Our experimental data on $\overline{p}\mathrm{He}^+$ was used in 2018 to set upper limits on forces that may arise between an electron and antiproton [28–30].

6. **Comparisons with precision spectroscopy experiments on metastable pionic helium atoms.** Recently part of our collaboration used the 590 MeV ring cyclotron facility of Paul Scherrer Institute (PSI) to attempt laser spectroscopy of $\pi\mathrm{He}^+ \equiv \pi^- + \mathrm{He}^{2+} + e^-$. This is a heretofore hypothetical three-body atom composed of a helium nucleus, a 1s electron, and a negatively-charged pion occupying a Rydberg state of principal and angular momentum quantum numbers $\ell \sim n - 1 \sim 15$ [31–33]. This would constitute the first laser excitation and spectroscopy of an atom containing a meson. The experimental and theoretical techniques developed for $\overline{p}\mathrm{He}^+$ at CERN are crucial for this PSI experiment involving $\pi\mathrm{He}^+$.

7. **Studies of chemical physics reactions of $\overline{p}\mathrm{He}^+$.** Parasitically to the above high precision experiments, we also plan to continue our long-standing studies on the chemical physics properties of $\overline{p}\mathrm{He}^+$. These experiments provide important feedback to phenomenological models of electromagnetic cascade processes that are widely used in various astrophysical, hypernuclei, meson spectroscopy, and X-ray spectroscopy experiments involving the formation of exotic atoms. The measurements include a determination of the yield of antiprotons populating each state (n, ℓ) of the atom [34], radiative and Auger lifetimes [35–38], and collisional effects [39, 40] between $\overline{p}\mathrm{He}^+$ and other helium atoms in the target which destroy the populations in these states. The ELENA beam allows us to study these at much lower densities of the experimental target than before, which may lead to the formation of atoms populating higher n levels. Another interesting topic is the two-body antiprotonic helium ion ($\overline{p}\mathrm{He}^{2+}$)

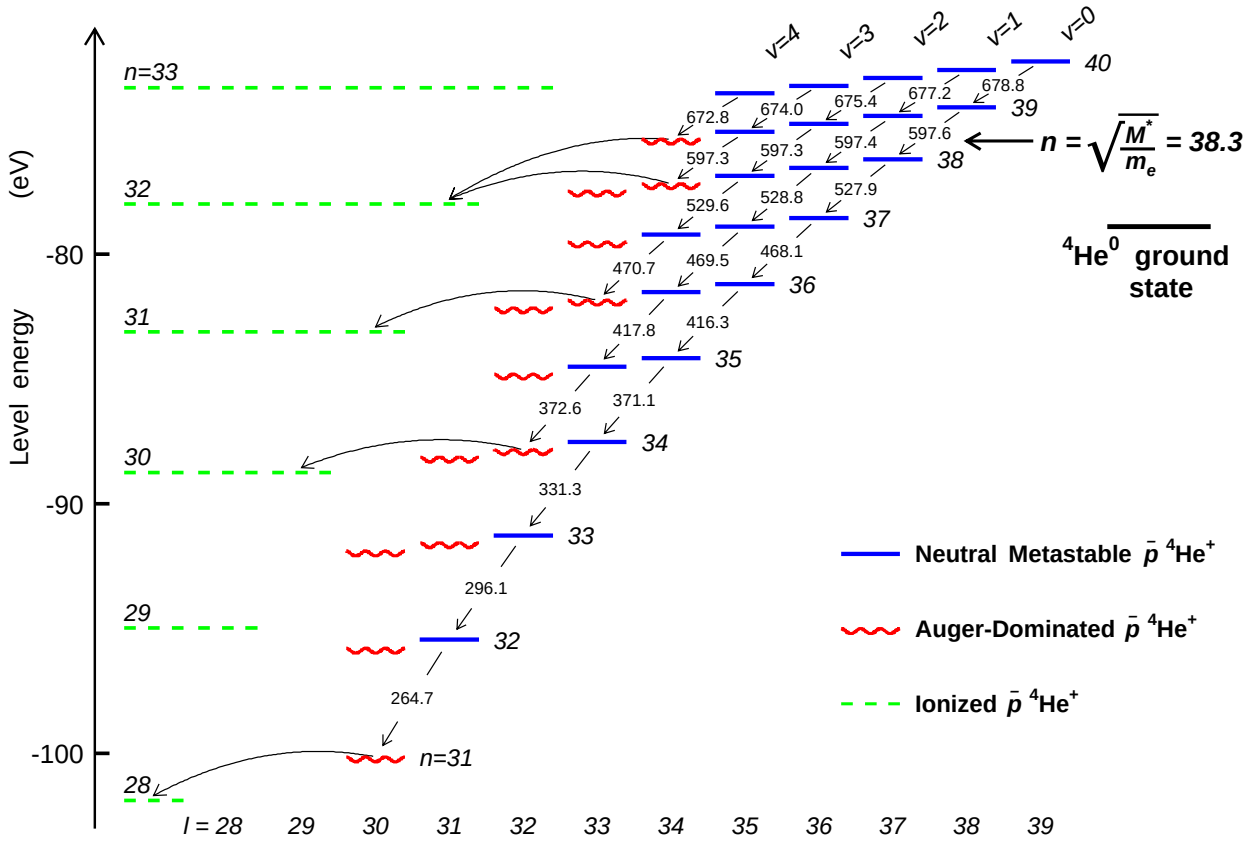

Figure 4 – Level structure of the $\overline{p}^4\mathrm{He}^+$ atom. The solid lines indicate the radiation-dominated metastable levels with lifetimes of 1–2 μs, the wavy lines Auger-dominated short-lived states. The broken lines show the final $\overline{p}\mathrm{He}^{2+}$ ionic states formed after Auger e^- emission. The curved arrows indicate Auger transitions with minimum $|\Delta\ell|$. On the left-hand scale the theoretical absolute energy of each state (n, ℓ) is plotted relative to the three-body-breakup threshold. The calculated resonance wavelengths of radiative transitions following the constant-v propensity rule are given in nanometers. Figure from Ref. [37].

which is a singly-charged, two-body system composed of only the antiproton and helium nucleus. We have previously synthesized cold (temperature $T \sim 10$ K) $\overline{p}^4\mathrm{He}^{2+}$ and $\overline{p}^3\mathrm{He}^{2+}$ ions with lifetimes $\tau_i \sim 100$ ns against annihilation [41–43]. Owing to the simple atomic structure, the ion may be a candidate for future precision laser spectroscopy experiments.

Antiprotonic atoms can be readily synthesized in a given element X by replacing the atomic electrons with a negatively-charged antiproton. The substitution takes place spontaneously when antiprotons are brought to rest in the substance concerned. ASACUSA synthesises $\overline{p}\mathrm{He}^+$ via the reaction,

$$\overline{p} + \mathrm{He} \rightarrow \overline{p}\mathrm{He}^+_{(n,\ell)} + e^-, \tag{1}$$

which occurs when an antiproton beam comes to rest in a helium target. Some of the antiprotons are then captured [34] into states with n-values of around,

$$n \sim n_0 = \sqrt{M^*/m_e}, \tag{2}$$

where M^* denotes the reduced mass of the antiproton-helium nucleus system, and m_e the electron

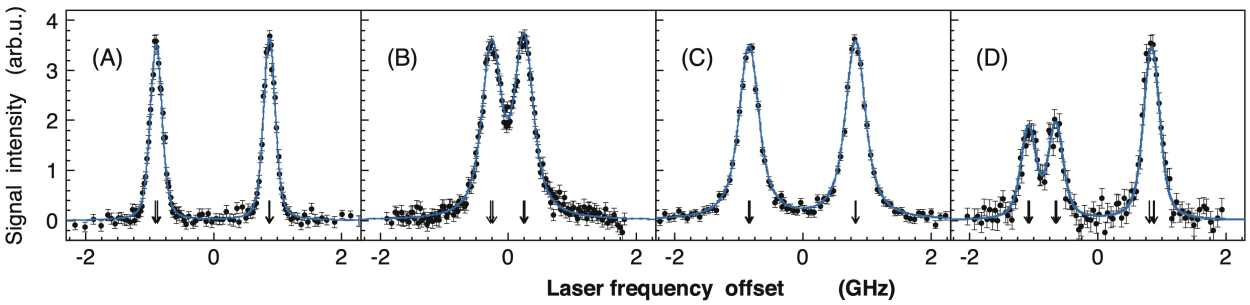

Figure 5 – Resonance profiles of the single-photon transitions (A) $(n,l) = (37,35)\rightarrow(38,34)$, (B) $(39,35)\rightarrow(38,34)$, and (C) $(38,35)\rightarrow(39,34)$ of buffer-gas cooled $\overline{p}^4\mathrm{He}^+$ atoms. The narrow, intense spectral lines are compatible with the Doppler widths of atoms cooled to $T = 1.5-1.7$ K, relative to the corresponding transition frequencies between $\nu = 356$ and 502 THz and when the Auger widths of the resonance daughter states are subtracted. The arrows indicate the theoretical positions of the hyperfine lines caused by the spin-spin interaction between the antiproton and electron [44–47]; the (B) and (C) splittings had not been observed previously (D) The profile $(36,34)\rightarrow(37,33)$ of cooled $\overline{p}^3\mathrm{He}^+$ shows a further splitting due to the 3He nuclear spin. The x-abscissa indicates the offset of the optical frequency of the laser relative to the resonance centroid. Blue curves indicate the best fit of an ab initio model based on the optical Bloch equation [11].

mass. This corresponds to the antiproton orbital with the same radius and binding energy as that of the displaced 1s electron. The n_0 values for the $\overline{p}^4\mathrm{He}^+$ and $\overline{p}^3\mathrm{He}^+$ isotopes are respectively 38.3 and 37.1 (Fig. 4).

Other varieties of antiprotonic atoms are usually destroyed within picoseconds by electromagnetic cascade mechanisms that result in the annihilation of the antiprotons in the nucleus. The $\overline{p}\mathrm{He}^+$ atom alone retains microsecond-scale lifetimes even in dense helium targets. The extreme longevity is due to the fact that the antiprotons trapped in the above-mentioned Rydberg states have almost no overlap with the nucleus, and furthermore cannot easily deexcite by Auger emission of the electron owing to its large ($I \sim 25$ eV) binding energy and the large multiplicity ($\Delta\ell > 3$) of the necessary transition. The electron protects the antiproton during collisions with other helium atoms. The relative ease in synthesising large numbers of $\overline{p}\mathrm{He}^+$ and its long lifetime makes this atom amenable to high precision laser spectroscopy (Fig. 5). In the proceeding sections, we will discuss each of the above physics motivations in more detail.

1.2 Higher-order QED

The $\overline{p}\mathrm{He}^+$ transition frequencies have recently been calculated to a precision of $< 5\times10^{-11}$ by evaluating the complete set of QED corrections up to order α^6 (Table 1). These a priori calculations used the CODATA2014 [18] recommended values of the fundamental constants, including the fine structure constant α, the ^{3}He- and ^{4}He-to-electron mass ratios, the Bohr radius, and the Rydberg constant. This involved first solving the non-relativistic Hamiltonian of the three-body system expressed in natural units of $m_e = \hbar = e = 1$,

$$E_{\mathrm{nr}} = \left\langle -\frac{1}{2m_{13}}\nabla^2_{\mathbf{r}_1} - \frac{1}{2m_{23}}\nabla^2_{\mathbf{r}_2} - \frac{1}{m_3}\nabla_{\mathbf{r}_1}\nabla_{\mathbf{r}_2} + \frac{Z_1Z_3}{r_1} + \frac{Z_2Z_3}{r_2} + \frac{Z_1Z_2}{R}, \right\rangle . \tag{3}$$

using numerical variational methods. Here the indices 1, 2, and 3 correspond respectively to the helium nucleus, antiproton, and electron. In fact, in the case of the ground state of normal

ΔE_{nr}	=	2 145 088 265.34
ΔE_{α^2}	=	−39 349.33
ΔE_{α^3}	=	5 857.84
ΔE_{α^4}	=	92.97
ΔE_{α^5}	=	-8.25(2)
ΔE_{α^6}	=	-0.10(10)
ΔE_{total}	=	2 145 054 858.50(10)

Table 1 – Contributions from different relativistic and QED corrections to the transition frequency of the $\overline{p}^4\mathrm{He}^+$ transition $(n, \ell) = (33, 32) \rightarrow (31, 30)$ in MHz. The precision of the QED calculations reached $< 5 \times 10^{-11}$ in 2015. From Ref. [4].

helium atoms, the non-relativistic binding energy $E_{\mathrm{nr}} = -2.903724377034119598296$ a.u. has been calculated to 19–22 digits of precision by several theoretical groups [48–50] using a variety of trial functions containing a few thousand basis sets. The case of $\overline{p}\mathrm{He}^+$ is in principle more difficult since the states are resonances that can decay by Auger emission of the electron. Nevertheless for some $\overline{p}\mathrm{He}^+$ states with microsecond-scale lifetimes against Auger and radiative decay, the non-relativistic energy E_{nr} have been calculated with a claimed precision of 15–16 digits. More recently, even states with nanosecond-scale Auger lifetimes have been calculated to 14–15 digits of precision [3] by the complex-coordinate rotation (CCR) method.

Perturbative calculations [1, 2] were then carried out to determine the relativistic corrections arising from the 1s electron and He nucleus, and the anomalous magnetic moment of the electron. Also calculated were QED corrections due to the one-transverse-photon exchange; the one-loop self-energy and vacuum polarization; the recoil correction of order $R_\infty \alpha^3 m_e/M_{\overline{p}}$; and one- and two-loop corrections of orders $R_\infty \alpha^4$ and $R_\infty \alpha^5$. The charge radii of the ^{3}He and ^{4}He nuclei give small corrections of 4–7 MHz, whereas that of the antiproton $r_{\overline{p}}$ is even smaller (< 1 MHz).

This insensitivity to the (anti)proton charge radius is due to the fact that the antiproton and electron orbitals in $\overline{p}\mathrm{He}^+$ repel each other and do not strongly overlap. This makes $\overline{p}\mathrm{He}^+$ particularly suitable for studying bound-state QED at the highest precision. Whereas calculations of the 1s-2s energy interval of (anti)hydrogen are currently limited to a precision of better than $\sim 1 \times 10^{-10}$ by the so-called "proton size puzzle", i.e., the $\sim 4\%$ uncertainty on the known proton charge radius r_p [15–17] that must be included as a parameter in the calculation, the transition frequencies of $\overline{p}\mathrm{He}^+$ are far less sensitive ($\sim 10^{-12}$) to $r_{\overline{p}}$ [2, 3].

Theoretical groups have continued to steadily improve the precision of the $\overline{p}\mathrm{He}^+$ calculations by evaluating QED terms of order α^6 and higher. Estimations indicate that a precision of $\sim 6 \times 10^{-12}$ may eventually become possible, which is > 400 times higher than our best experimental results that have been published so far in 2016 (Fig. 6). This motivates us to continue these experiments to improve the precision on the $\overline{p}\mathrm{He}^+$ transition frequencies to a similar level using the high-quality antiproton beam available from ELENA.

A particularly difficult theoretical challenge at even higher precisions of $< 6 \times 10^{-12}$ would be the calculation of the so-called two-loop self energy correction. The uncertainties in these types of QED corrections currently limit the precision in determining many other physical constants, including the g-factor of hydrogenlike ions which are necessary to determine the electron mass m_e and the proton-to-electron mass ratio m_p/m_e.

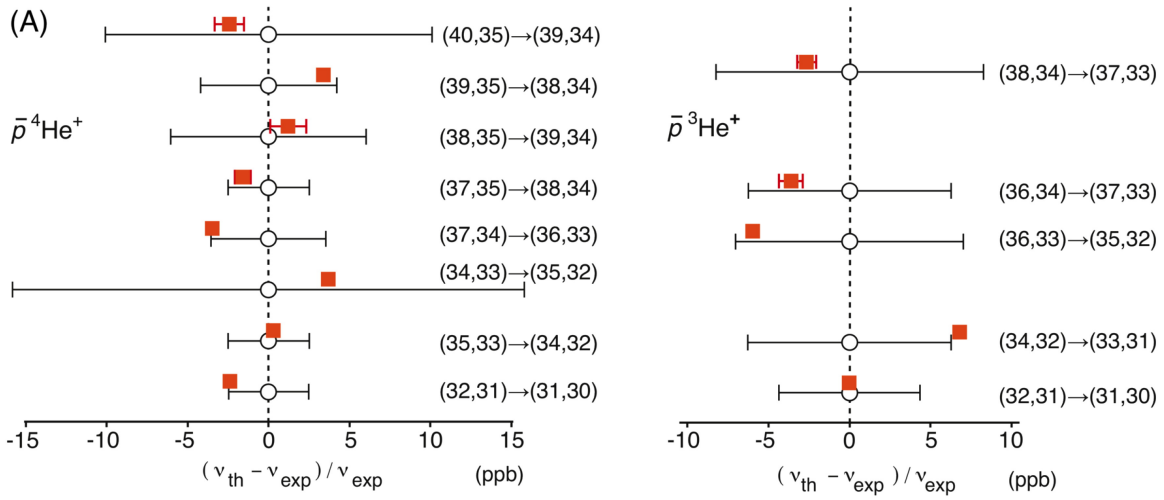

Figure 6 – Comparison of experimental and calculated transition frequencies. Shown are the fractional differences between the experimental (open circles) and theoretical (squares) values of 13 transition frequencies of $\overline{p}^4\mathrm{He}^+$ and $\overline{p}^3\mathrm{He}^+$ atoms cooled to $T = 1.5 - 1.7$ K.

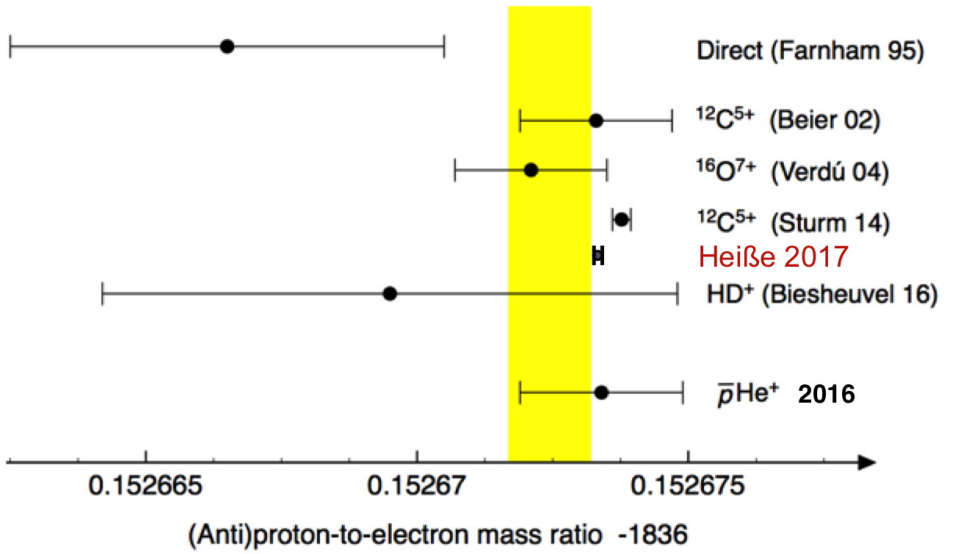

Figure 7 – M_p/m_e mass ratios measured in Penning traps and laser spectroscopy of HD^+ molecular ions, compared with the $M_{\overline{p}}/m_e$ mass ratio determined by laser spectroscopy of $\overline{p}\mathrm{He}^+$ [9]. Shaded area represents the CODATA 2010 recommended value.

1.3 Determination of the antiproton-to-electron mass ratio

The (anti)proton-to-electron mass ratio is a vital input parameter in setting up the international system of scientific units, as it corresponds to the ratio between the only stable charged lepton and hadron that can be experimentally measured with high precision. So far the ASACUSA collaboration published the measurements of thirteen single-photon transition frequencies of $\overline{p}\mathrm{He}^+$ to a fractional precision of $(2.5 - 16) \times 10^{-9}$ [9]. By comparing the result with three-body QED

calculations the antiproton-to-electron mass ratio was determined as,

$$M_{\overline{p}}/m_e = 1836.1526734(15). \tag{4}$$

In 2017, the atomic mass of the proton [20] was determined with a relative precision of 3×10^{-11} by precisely measuring the characteristic frequencies of a single proton and a hydrogenic $^{12}C^{6+}$ ion confined in a magnetic Penning trap. The published result,

$$M_p = 1.007276466583(15)(29)\text{u} \tag{5}$$

differs by 3 standard deviations from the latest CODATA2014 value. This follows a measurement of 2014, in which the atomic mass of the electron [21] was determined with a relative precision of 3×10^{-11} by confining a $^{12}C^{5+}$ ion in a Penning trap. The cyclotron frequency of its motion in a magnetic field and the precession frequency of the electron spin was measured, and the results compared with QED calculations of its g-factor. The published value,

$$m_e = 0.000548579909067(14)(9)(2)\text{u} \tag{6}$$

differs from the CODATA 2010 value by 2 standard deviations. From the two values, the latest proton-to-electron mass ratio was determined as,

$$M_p/m_e = 1836.152673346(81). \tag{7}$$

In Fig. 7, these M_p/m_e mass ratios are shown together with the previous experimental values that were determined by comparing the cyclotron frequencies of protons and electrons in a Penning trap [51], laser spectroscopy of HD^+ molecular ions [12], and the CODATA 2010 recommended value [19].

From high-precision spectroscopy of $\overline{p}He^+$ described in this proposal, $M_{\overline{p}}/m_e$ can in principle be determined with a relative precision of $\sim 10^{-11}$, though it is hard to predict what new systematic errors can arise, and things must proceed over many years in a step-by-step manner as we learn to use the new machine. If our efforts are successful, the value should rival the above cited determinations of M_p/m_e from Penning trap experiments [20, 21] and laser spectroscopy of HD^+ molecular ions [12–14]. We would then have a very robust value of M_p/m_e (or $M_{\overline{p}}/m_e$) and the electron mass.

1.4 CPT symmetry

Spectroscopy of $\overline{p}He^+$ also provides a consistency test of CPT symmetry in a hadron-antihadron bound system. For this we use the analysis method of Hughes and Deutch [22–25] to constrain the equality between the antiproton and proton masses and charges,

$$\delta_M = (M_p - M_{\overline{p}})/M_p, \quad \delta_Q = (Q_p + Q_{\overline{p}})/Q_p. \tag{8}$$

The $\overline{p}^4He^+$ atomic transition frequencies are proportional to $Q_{\overline{p}}^2 M_{\overline{p}}$ and have linear dependencies $\delta_M \kappa_M + \delta_Q \kappa_Q < |\nu_{\text{exp}} - \nu_{\text{th}}|/\nu_{\text{th}}$, where the sensitivities κ_M and κ_Q have been calculated by three-body calculations. The right side of the equation was evaluated as $< (3 \pm 15) \times 10^{-10}$ by averaging over the transitions and considering the statistical and systematic uncertainties. The TRAP and BASE collaborations [22–24] have on the other hand measured the cyclotron frequency,

$$\omega_c \propto Q_{\overline{p}}/M_{\overline{p}}, \tag{9}$$

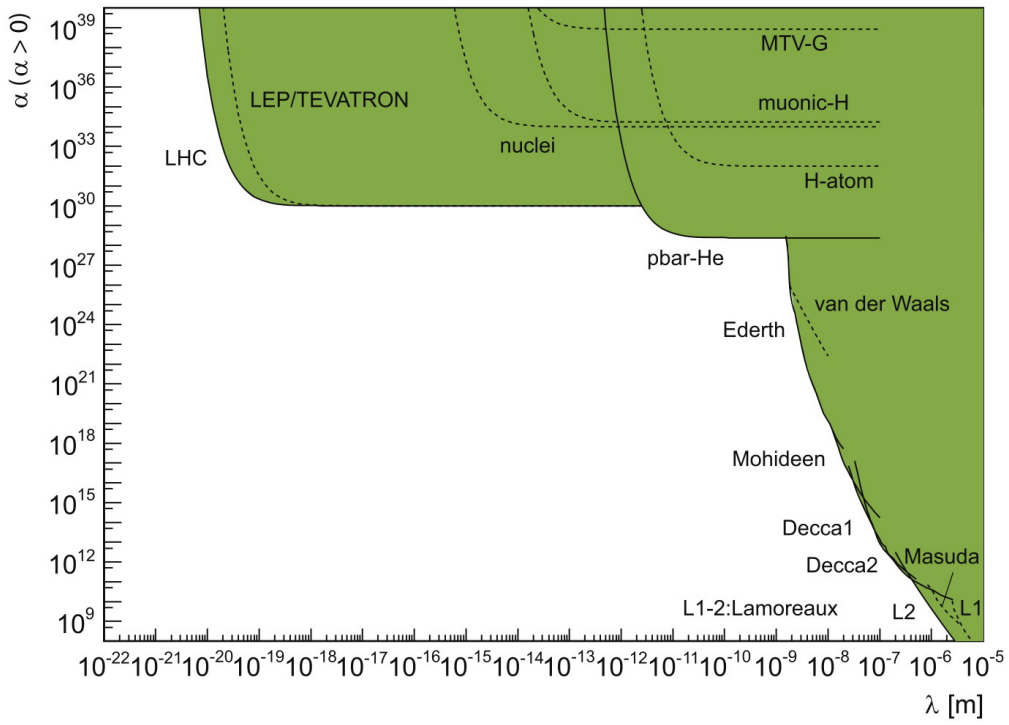

Figure 8 – Exclusion plot on the constraints between the length scale λ and the fifth force coupling parameter α obtained from collider experiments, atomic spectroscopy, Casimir force, and cryogenic cantilever experiments concerning a possible fifth force with a Yukawa-type potential. Note the constraint obtained from the $\overline{p}\mathrm{He}^+$ experimental data. From Ref. [27].

of antiprotons confined in Penning traps as $(Q_{\overline{p}}/M_{\overline{p}})/(Q_p/M_p) + 1 = 1.6(9) \times 10^{-10}$ [22, 23] and $1(69) \times 10^{-12}$ [24] which implies that $\delta_Q \sim \delta_M$. By combining the two types of experimental results, we conclude that any deviation between the proton and antiproton masses and charges are $< 5 \times 10^{-10}$ at the 90% confidence level. The ALPHA experiment has provided a limit $< 7 \times 10^{-10}$ on any residual charge of antihydrogen [7], by analyzing its movement in a magnetic bottle trap; when combined with the $\overline{p}\mathrm{He}^+$ results, this constrains the equality of the electron and positron charges to a similar level. The high precision spectroscopic studies outlined in this proposal would in principle improve this limit to $\sim 10^{-11}$ or better, though many years of systematic studies are needed to achieve this.

1.5 Upper limits on fifth forces

The most stringent constraint on any deviation from the inverse square law of gravity,

$$F_{\mathrm{g}} = G_{\infty} \frac{Mm}{r^2}, \tag{10}$$

that arise between two point particles of mass M and m separated by a distance r is currently derived from laser ranging measurements which search for any anomaly in the precession rate of the moon's orbit around the earth [52, 53]. From these experiments, Eq. 10 has been tested to a fractional precision of $< 2 \times 10^{-11}$ for length scales $r \sim 10^8$ m that are similar to the earth-moon system. On the other hand the gravitational force F_{g} at short length scales $r \sim 100$ μm has been measured using mechanical torsion balances of remarkable sensitivity. At still shorter length scales

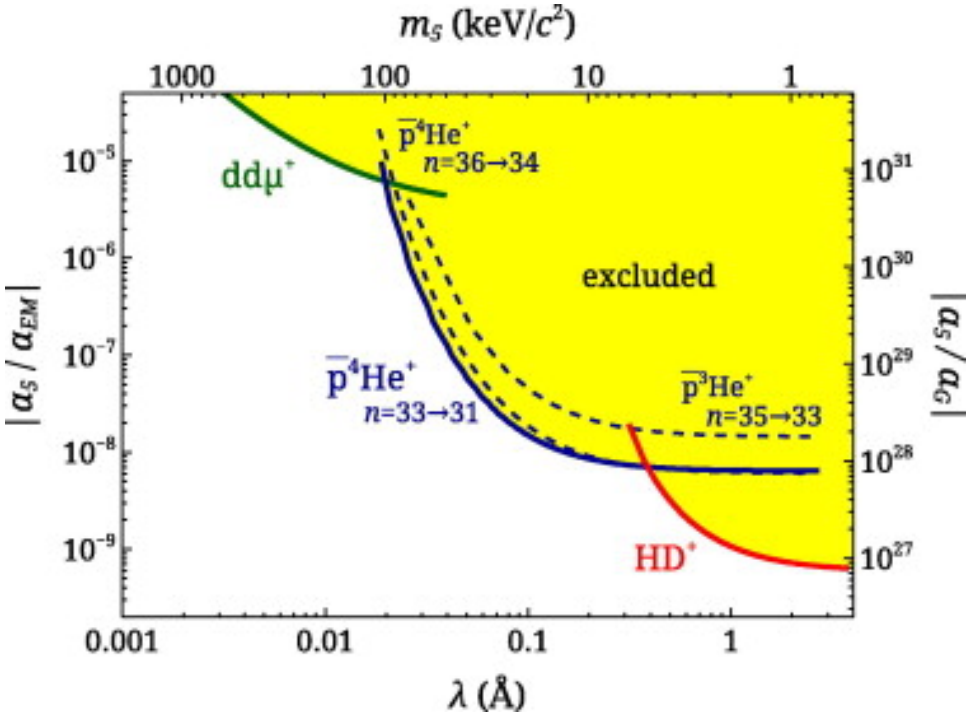

Figure 9 – Exclusion plot on a possible fifth force at Angstrom length scales provided by experiments on muonic $dd\mu^+$, antiprotonic $\overline{p}He^+$ and HD^+. From Ref. [26].

< 100 μm cryogenic mechanical cantilevers that detect forces of order $< 10^{-16}$ N are used, but it is no longer straightforward to shield the apparatus from the dominant effect of the Coulomb interaction. Only upper limits on F_g which are orders of magnitude larger than the gravitational force can be determined.

As the inverse square law of F_g has not been directly verified for microscopic length scales < 100 μm, numerous models allowing some deviation due to a hypothetical fifth force have been proposed for many years. One standard parameterization of such a potential $V(r)$ of Yukawa-type can be expressed in the form,

$$V(r) = -G_\infty \frac{Mm}{r}\left(1 + \alpha e^{-r/\lambda}\right), \tag{11}$$

wherein α denotes the coupling strength of the new interaction, and $\lambda = \hbar/m_b c$ the so-called Yukawa range corresponding to a hypothetical boson of mass m_b being exchanged. An exclusion plot on the constraints between the length scale λ and the fifth-force coupling parameter α obtained from collider experiments, atomic spectroscopy, and Casimir force experiments are shown Fig. 8. Our $\overline{p}He^+$ experiments constrain $V(r)$ at a length scale between 10^{-11} and 10^{-9} m at a level of $\alpha \leq 10^{28}$. Further improvements in the experimental precision and theoretical refinements may provide a more stringent constraint. By comparison, according to Ref. 8 collider experiments provide a constraint $\alpha \leq 10^{30}$.

Another theoretical study [26] based on a possible fifth-force potential of the form,

$$V_5 = N_1 N_2 \alpha_5 \frac{\exp(-r/\lambda)}{r}\hbar c, \tag{12}$$

yielded the exclusion plot shown in Fig. 9. Here the absolute value of the fifth force coupling constant relative to that of the electromagnetic interaction, $|\alpha_5/\alpha_{\rm EM}|$, is shown at distance scales

between 0.001 and 1 Å. The complementary length scales relevant to the three molecules involving a muon ($dd\mu^+$), antiproton ($\overline{p}He^+$) and HD^+ arise from variations in the average distances between the two heavy particles in each atom.

1.6 Upper limits on exotic velocity and spin-dependent, semi-leptonic forces due to the exchange of exotic bosons

In the late 1970's to early 1980's, the spontaneous breaking of an anomalous global Peccei-Quinn symmetry of the QCD vacuum by a new scalar field was suggested as a possible and natural explanation of why the so-called θ parameter that should imply significant CP violation in the strong interaction is instead so very small. According to the latest experiment which searches for a permanent electric dipole moment (EDM) of the neutron [54], this parameter is constrained to a level of $\theta < 7 \times 10^{-12}$. This inability of experiments to observe any CP violating effect in strong interactions constitutes the "strong CP problem". It was soon realized that this symmetry breaking should give rise to an accompanying pseudo Nambu-Goldstone boson called an axion [55,56], which could interact with normal leptons and quarks through dipolar interactions [28,57,58]. Experiments

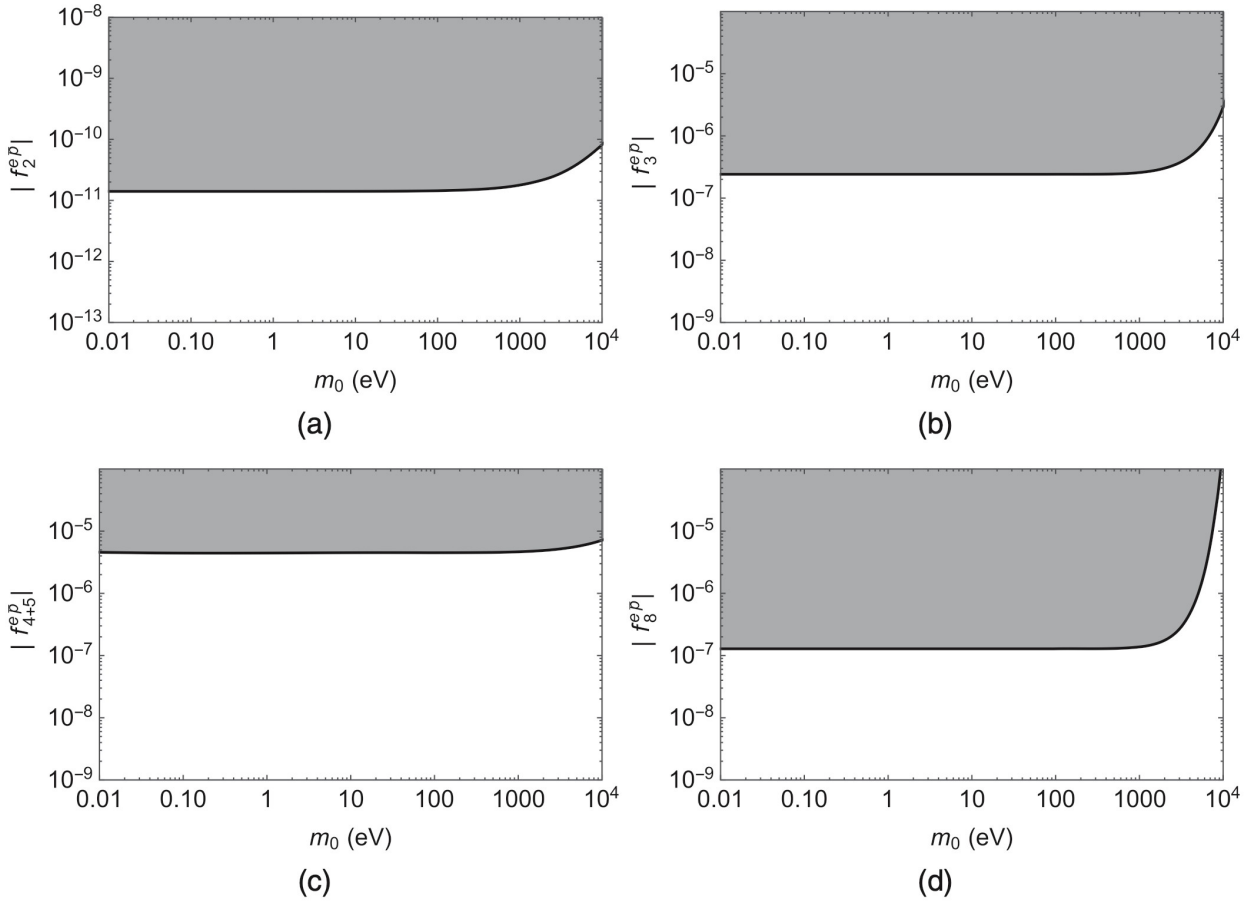

Figure 10 – Constraints at the 90% confidence level on the magnitude of the coupling constants for four types of possible spin- and velocity-dependent potentials arising between antiprotons and electrons in $\overline{p}He^+$, due to axions or other undiscovered spin-0 and spin-1 bosons, as a function of the mass of the possible exchange boson. From Ref. [29].

and astrophysical observations of, e.g., apparent anomalies in the cooling rate of white dwarfs appear to favour a weakly interacting "invisible" axion with a mass in the <milli-eV range, which could also be a candidate for dark matter [59].

By far the most promising methods for detection of an axion appear to be through its coupling to two photons, which should allow an axion to convert into a signal photon in a strong magnetic field. For this several large-scale experiments involving solar axion telescopes [60] or so-called light-shining-through-a-wall [61] measurements are currently underway at CERN and elsewhere. An alternative indirect approach which has gained interest in the last few years involves the use of atomic spectroscopy [28–30, 62, 63]. Here undiscovered spin-0 or spin-1 bosons such as axions, familons, Majorons, or arions are assumed to couple with the constituent particles within an atom, causing dipolar interactions that could then be detected as, e.g., shifts in the characteristic transition energy. Their Angstrom-scale sizes make atoms particularly sensitive to the virtual exchange of such exotic bosons in the mass range $m = 0.01$–1000 eV.

Figs. 10(a)–(d) show exclusion plots at the 90% confidence level on the magnitude of the coupling constants for four types of spin-dependent interactions between the antiproton and electron in $\overline{p}\mathrm{He}^+$ as a function of the mass of the hypothetical boson that was obtained from the ASACUSA experimental results. This work published in 2018 [29] was carried out by a Polish-German-American-Russian theoretical collaboration.

1.7 Comparisons with pionic helium atom experiments

Part of the ASACUSA collaboration has recently attempted to carry out laser spectroscopy [31] of metastable pionic helium ($\pi\mathrm{He}^+ \equiv \pi^- + \mathrm{He}^{2+} + e^-$) at the 590 MeV ring cyclotron facility of PSI. A successful experiment would constitute the first laser excitation and spectroscopy of an atom containing a meson. This hypothetical atom [64, 65] is formed by the process,

$$\pi^- + \mathrm{He} \rightarrow \pi\mathrm{He}^+ + e^-, \tag{13}$$

that spontaneously occurs when a beam of π^- is allowed to come to rest in a liquid helium target. According to the atomic capture model of Eq. 2, the π^- may populate Rydberg states of $n \sim 16$ that are expected to retain nanosecond-scale lifetimes against the absorption of the π^- into the helium nuclei and $\pi^- \rightarrow \mu^- + \overline{\nu}_\mu$ decay. As in the $\overline{p}\mathrm{He}^+$ case, this is because the π^- orbitals have very little overlap with the nucleus, whereas the electromagnetic cascade processes that normally lead to immediate nuclear absorption are suppressed. The large antiproton mass makes $\overline{p}\mathrm{He}^+$ resemble a diatomic molecule where the slow vibrational motion between the antiproton and helium nucleus can be adiabatically separated from the excitations of the electron. This contributes to the atom's stability. By comparison, the much smaller π^- mass makes $\pi\mathrm{He}^+$ far less stable against Auger decay.

The existence of $\pi\mathrm{He}^+$ has been indirectly inferred from several experiments carried out in the 1960's and 1990's that found some π^- that come to rest in helium targets retain a lifetime of ~ 0.3–7 ns. No atomic line of $\pi\mathrm{He}^+$ has been observed previously and nothing was experimentally known about the n and ℓ distribution of states which may be formed. In fact, the lifetimes of some $\pi\mathrm{He}^+$ states calculated recently [31] using the complex-coordinate rotation method differed by 1–2 orders of magnitude from earlier calculations made in the 1960's. A laser spectroscopic signal would conclusively demonstrate the existence of $\pi\mathrm{He}^+$, and experimental data from this first step have recently been submitted by us to a scientific journal. By comparing the transition frequencies of the atom measured in future experiments with the results of three-body QED calculations, the mass [66–69] and other properties of π^- can in principle be determined with a high precision, as in the $\overline{p}\mathrm{He}^+$ case.

Laser spectroscopy of $\pi\mathrm{He}^+$ is far more difficult than $\overline{p}\mathrm{He}^+$ for several reasons. Compared to the high quality antiproton beam available using AD and ELENA, it is difficult to efficiently decelerate or cool high-intensity beams of π^- due to its short (~ 26 ns) lifetime. Any spectroscopy experiment suffers from large beam-induced backgrounds which make it difficult to resolve the weak signal. The short lifetime of $\pi\mathrm{He}^+$ gives only a narrow time window where the resonance with the laser beam can be induced. For these reasons, the PSI experiment would not have been feasible without the spectroscopic and theoretical techniques developed at CERN using $\overline{p}\mathrm{He}^+$ over many years. Continued experimental study and comparisons between $\overline{p}\mathrm{He}^+$ and $\pi\mathrm{He}^+$ afford us a better understanding of various systematic effects needed to improve the precision in both measurements, e.g. collisional shifts of the atomic frequencies and the destruction of some atomic states during collisions with normal helium atoms.

1.8 Chemical physics

In parallel to the high-precision experiments, the chemical-physics properties of $\overline{p}\mathrm{He}^+$ have been studied for many years. These parasitic experiments provide important feedback to phenomenological models of electromagnetic cascade processes that are widely used in various astrophysics, hypernuclei, meson spectroscopy, and X-ray spectroscopy experiments involving exotic atoms. They are also vital in understanding the various systematic effects needed to improve the precision on the transition frequencies.

The number of antiprotons populating states (n, ℓ) was studied by measuring the intensity of the laser resonance involved in each state [34, 38]. Nearly all the $\overline{p}\mathrm{He}^+$ were found to lie in the region $n = 37$–40 immediately after the formation of the atom, with the $n = 38$ and 37 states having the largest population. This appears to support the estimation given in Eq. 2. Theoretical calculations also predict sizable populations in the $n > 40$ states, but experiments detected very few antiprotons in them. This may be due to collisions between $\overline{p}\mathrm{He}^+$ and other helium atoms in the target which destroy the populations in these states. Using the ELENA beam, it would become possible to efficiently produce the atoms in helium targets of low atomic density $\rho \leq 10^{16}$ cm^{-3} where the rate of such collisions would be highly reduced.

The Auger rates of $\overline{p}^3\mathrm{He}^+$ and $\overline{p}^4\mathrm{He}^+$ states were measured in Refs. [35,36]. Most of the results agreed with theoretical calculations, but state $(37, 33)$ in $\overline{p}^4\mathrm{He}^+$ revealed decay rates which were orders of magnitude larger than theoretical values. Calculations [39, 40] indicated that such a short lifetime is caused by a strong coupling to an electronically excited $\overline{p}^4\mathrm{He}^+$ state, where the electron occupies the $3d$ orbital, and the antiproton the state $(n, \ell) = (32, 31)$ [70]. The lifetime of $(37, 34)$ decreased from $\tau = 1.2$ μs to 130 ns, as ρ was increased from 1×10^{20} to 6×10^{21} cm^{-3}. Theoretical calculations [42, 71] have been unable to qualitatively explain the reason for this. Further experiments at ELENA would provide important information to refine these chemical physics models, which in turn is important for the high precision spectroscopy experiment.

The antiprotonic helium ion ($\overline{p}\mathrm{He}^{2+}$) is a singly-charged, two-body system composed of only the antiproton and helium nucleus. Cold (temperature $T \sim 10$ K) $\overline{p}^4\mathrm{He}^{2+}$ and $\overline{p}^3\mathrm{He}^{2+}$ ions with lifetimes $\tau_i \sim 100$ ns against annihilation were produced [41–43]. These states had principal and angular momentum quantum numbers $n_i = 28$–32 and $\ell_i = n_i - 1$, and constituted ideal semiclassical Bohr systems. Their spin-independent parts of the energy levels (left side of Fig. 4) can be calculated to high precision ($\sim 10^{-8}$) using the simple Bohr formula,

$$E_n = -\frac{4R_\infty hc}{n_i^2}\frac{M}{m_e}\frac{Q_{\overline{p}}^2}{e^2} \tag{14}$$

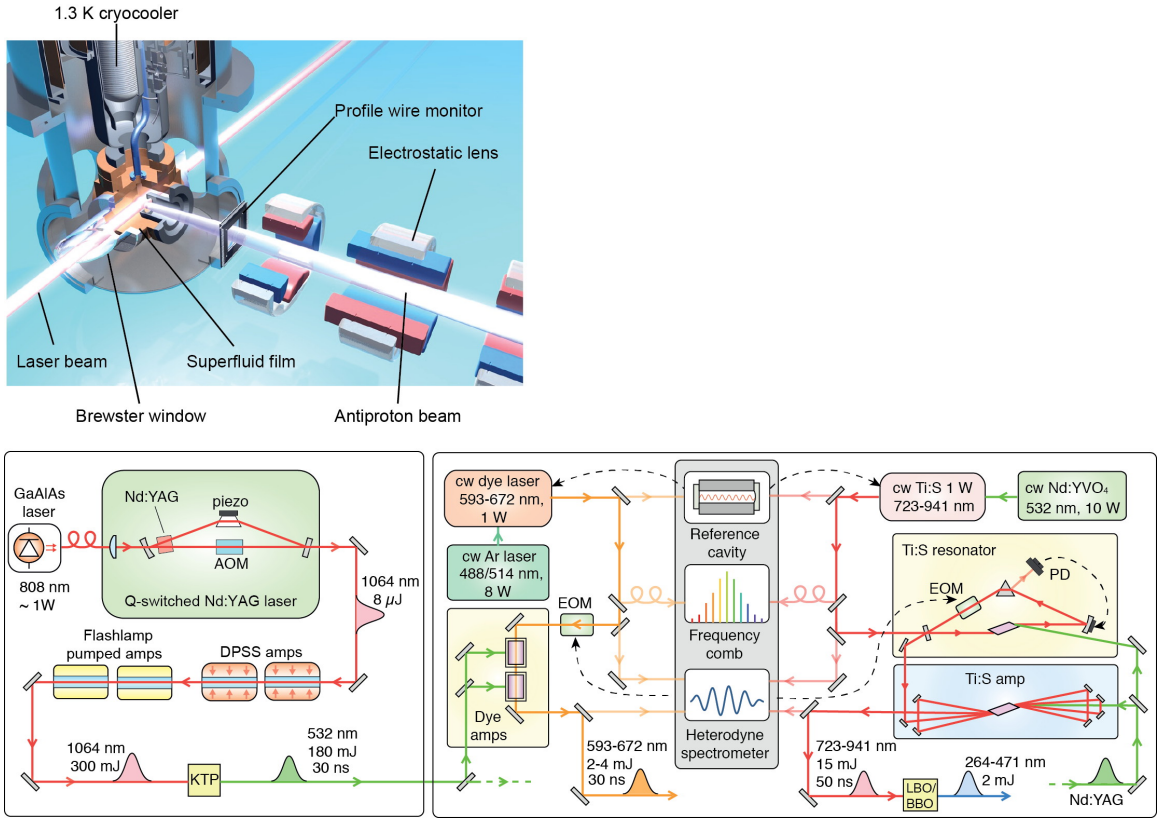

Figure 11 – Experimental layout of the experiment [9] using the RFQD beam to synthesize $\overline{p}\mathrm{He}^+$, which are then cooled to temperature $T = 1.5$–1.7 K (top). Laser system used for single-photon spectroscopy (bottom).

Owing to this simple structure, the ion may be a candidate for future precision laser spectroscopy experiments.

2 Experimental methods

2.1 Improvements due to the ELENA beam and new electrostatic beamline

The precision of past experiments was limited by systematic uncertainties and by statistics. Careful studies and the development of new techniques which increase the spectral resolution and signal-to-noise ratio are needed to improve the precision. The most recent published result (see Fig. 11) [9] of $\overline{p}\mathrm{He}^+$ was measured using a pulsed beam that contained between 4×10^6 and 6×10^6 antiprotons with an energy $E = 75$ keV. This involved slowing down the antiprotons ejected by AD in a 3 m long radiofrequency quadrupole decelerator (RFQD). The inherent limitations of the RFQD and the quality of the AD beam meant that on average $\sim 80\%$ of the antiprotons missed the longitudinal acceptance of the RFQD emerged with little deceleration, and were discarded in a beam dump. The remaining 20% fraction of 75 keV antiprotons were transported by a beamline and allowed to come to rest in a cryogenic helium gas target, thereby producing $\overline{p}\mathrm{He}^+$. The atoms were then irradiated by $\Delta t = 40$ to 100 ns long laser pulses [72] with peak powers $P = 0.5$ to 10 kW and wavelengths $\lambda = 264$ to 841 nm, which were generated by Ti:Sapphire or dye laser systems. This induced transitions between long-lived $\overline{p}\mathrm{He}^+$ states with microsecond-scale lifetimes, and short-lived states

Figure 12 – Photograph of the new ELENA beamline where the $\overline{p}\mathrm{He}^+$ experiment will be set up, as of September 2019.

with nanosecond-scale lifetimes against Auger emission of the 1s electron. The two-body $\overline{p}\mathrm{He}^{2+}$ ion that remained after Auger emission was rapidly destroyed by collisions with normal helium atoms in the experimental target. The resulting peak in the rate of antiproton annihilations signalled the resonance condition between the laser and atom.

Since the first measurements using the 21 MeV antiproton beam of LEAR, the construction of new decelerators (i.e., the 5.3 MeV beam of AD, the 100 keV beam of RFQD, and the improved magnetic-electrostatic transfer line downstream of RFQD) have consistently improved the experimental precision (see Fig. 3). Lower energy beams allow the production of $\overline{p}\mathrm{He}^+$ in low density targets where the rate of collisions with normal helium atoms that can shift the atomic frequency ν_{exp} is small. The cooled beam of ELENA will also lead to an improvement for several reasons,

1. **Beam emittance and size**, the RFQD beam that entered the experimental target had a large emittance ($\sim 100\pi$ mm mrad) and diameter ($d > 25$ mm), so that a laser beam of correspondingly large diameter (~ 30 mm) and energy (~ 1 MW) was needed to irradiate the volume occupied by the atoms and induce a significant number of resonant transitions. Many atoms diffused outside the laser beam and did not contribute to the signal. The ELENA beam by comparison has a smaller emittance ($< 5\pi$ mrad) and diameter (< 3 mm), so the laser energy can be reduced by 1–2 orders of magnitude, whereas the spatial overlap with the sample of atoms in the target will be greatly improved.

2. **Beam halo** arising from antiprotons that occupied the edge of the transverse acceptance of the RFQD during deceleration struck the walls of the experimental apparatus and produce a large background. The cooled ELENA beam by comparison has no large halo.

3. **Efficiency of deceleration**, on average $\sim 20\%$ of the antiprotons injected into the RFQD fit into its longitudinal acceptance and were decelerated, whereas the majority 80% emerged without full deceleration and did not reach the target. The ELENA beam has no such undecelerated component.

4. **Energy spread** of the $E = 75$ keV component of the RFQD beam was typically $\Delta E = \pm 10$ keV. This caused $> 30\%$ of the antiprotons to annihilate in the entrance window or walls of the experimental target without forming $\overline{p}\mathrm{He}^+$. The small momentum spread of the ELENA beam ($\sim 10^{-3}$) allows most of the antiprotons to come to rest in the helium target and contribute to the resonance signal.

5. **Beam microstructure**, the RFQD beam had a 200 MHz microstructure induced by the RF bunching cavity of the RFQD which can present an additional noise source to the experiment. The ELENA beam has no such RF microstructure.

6. **Fluctuations in the beam energy and position**, any small shift in the energy or orbit of the 5.3 MeV beam circulating in the AD became magnified during the deceleration in the RFQD. The electron-cooled beam of ELENA does not suffer from these large fluctuations.

Only a fraction of the antiprotons thus contributed to the $\overline{p}\mathrm{He}^+$ signal whereas the majority produced background. Analysis shows that the fluctuations in the laser resonance signal due to changes in the performance of AD are > 3 times larger than the statistically-expected ones calculated from the simple number of antiprotons arriving at the experiment. We therefore accumulated > 10 times more data to average over the shot-to-shot fluctuations and carefully check whether the beam has systematically shifted. The ELENA beam will not cause such large fluctuations or backgrounds, so it will be roughly equivalent to collecting > 10 times more experimental statistics. The S/N ratio is also expected to increase by factor 3–5.

The tuning of the 5.3 MeV AD beam through the RFQD and the maintenance of its > 1 MW RF amplifier tube which was prone to breakdowns complicated our past experiments. ASACUSA shared the RFQD between several sub-experiments that had to be set up and removed every year, so that on average only a few weeks of beamtime could be used for data taking. This made it difficult to carry out $\overline{p}\mathrm{He}^+$ experiments of high complexity involving many laser beams. These will be largely solved by the ELENA facility, as the $\overline{p}\mathrm{He}^+$ and antihydrogen experiments will reside in separate beamlines.

2.2 Two photon spectroscopy of narrow transitions of $\overline{p}\mathrm{He}^+$

As in normal atoms, the thermal motion of $\overline{p}\mathrm{He}^+$ at temperature T strongly broadens the measured width of the laser resonances by $\nu\sqrt{8k_BT\log 2/Mc^2}$, where ν denotes the transition frequency, k_B the Boltzmann constant, M the atom's mass and c the speed of light. The corresponding loss in spectral resolution limits the precision by which the resonance centroid can be determined. One way to reach a precision beyond this Doppler limit was provided by two-photon spectroscopy [10]. The atom was irradiated with two counter-propagating laser beams of UV wavelengths 296.1 nm and 264.7 nm indicated by arrows 1–2 in Fig. 13 (left). The small transition probability of the $(n,\ell)\rightarrow(n-2,\ell-2)$ resonance can be enhanced by factor $> 10^5$ if the counter-propagating laser beams are tuned such that the virtual intermediate state of the two-photon transition lies within $\nu_d \sim 10$ GHz of the real state $(n-1,\ell-1)$. The first-order Doppler width was is reduced by a factor $|\nu_1-\nu_2|/(\nu_1+\nu_2)$ revealing narrow spectral lines.

The limited statistics and signal-to-noise ratio of the experiments using the RFQD described in the previous section have largely limited our past measurements to intense but spectraly broad $\overline{p}\mathrm{He}^+$ transitions of natural width > 15 MHz. The simulated resonance profile of two such examples of two-photon transitions in $\overline{p}^4\mathrm{He}^+$ are shown in Fig. 14 (a)–(b) calculated using optical Bloch equations [11].

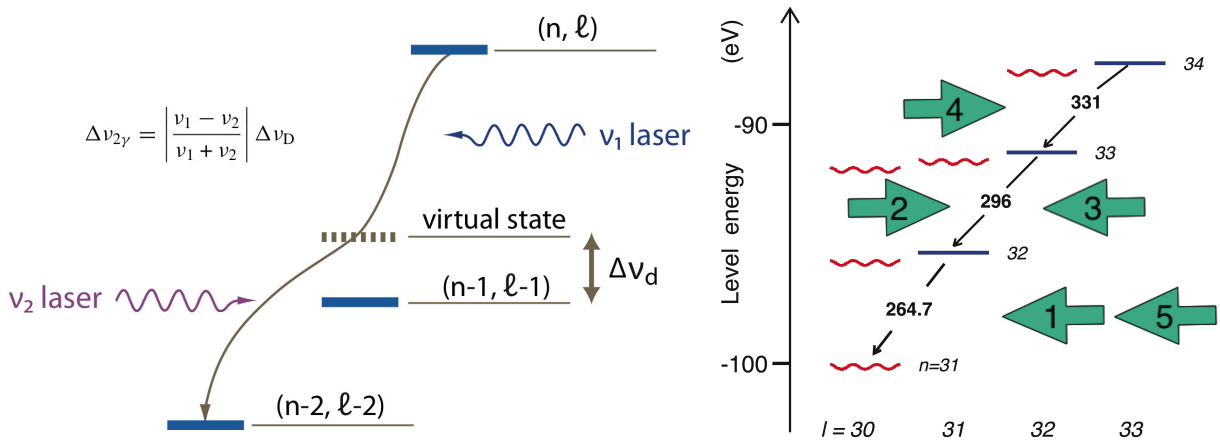

Figure 13 – **Left:** Schematic energy level diagram showing the principle of two-photon laser spectroscopy. The $\overline{p}\mathrm{He}^+$ atoms are irradiated with two counter-propagating laser beams, their optical frequencies ν_1 and ν_2 adjusted so that the virtual intermediate state lies close to a real state $(n-1, \ell-1)$. This increases the probability of a sub-Doppler two-photon transition occurring, wherein the atom emits two photons simultaneously and deexcites from the state (n, ℓ) to $(n-2, \ell-2)$. **Right:** Energy level diagrams of the $\overline{p}^4\mathrm{He}^+$ isotope indicating the position of the $(n, \ell) = (33, 32) \rightarrow (31, 30)$ two-photon transition measured in 2018. The principal n and angular momentum ℓ quantum numbers, and the level energy relative to the three-body breakup threshold is shown for each isotope. The transition wavelengths in nanometers are indicated. In 2018, the atom was irradiated by two counterpropagating beams labeled 1 and 2 above. In > 2021, we propose to measure the transition $(34, 33) \rightarrow (32, 31)$ using five laser beams 1–5 fired in sequence.

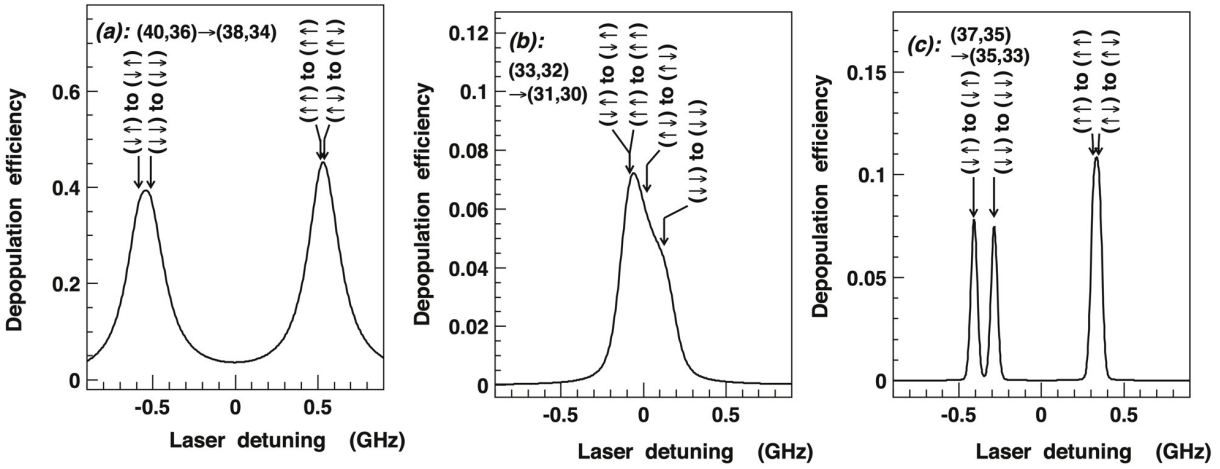

Figure 14 – Simulated resonance profiles of three two-photon transitions in $\overline{p}^4\mathrm{He}^+$ excited at laser intensities $p = 1$ mJ/cm^2. The virtual intermediate state was tuned $\Delta\omega_d/2\pi \sim -12$ GHz from a real state. The positions of the four hyperfine lines are indicated by arrows, together with the principal and angular momentum quantum numbers (n, L) and spin orientations $(S_e, S_{\overline{p}}) \rightarrow (S'_e, S'_{\overline{p}})$ of the resonance parent and daughter states. So far our experiments were concentrated on the broad but intense lines of the type (a)–(b). This proposal aims to utilize the ELENA beam to measure the weak but far narrower resonances of the type (c). From Ref. [11].

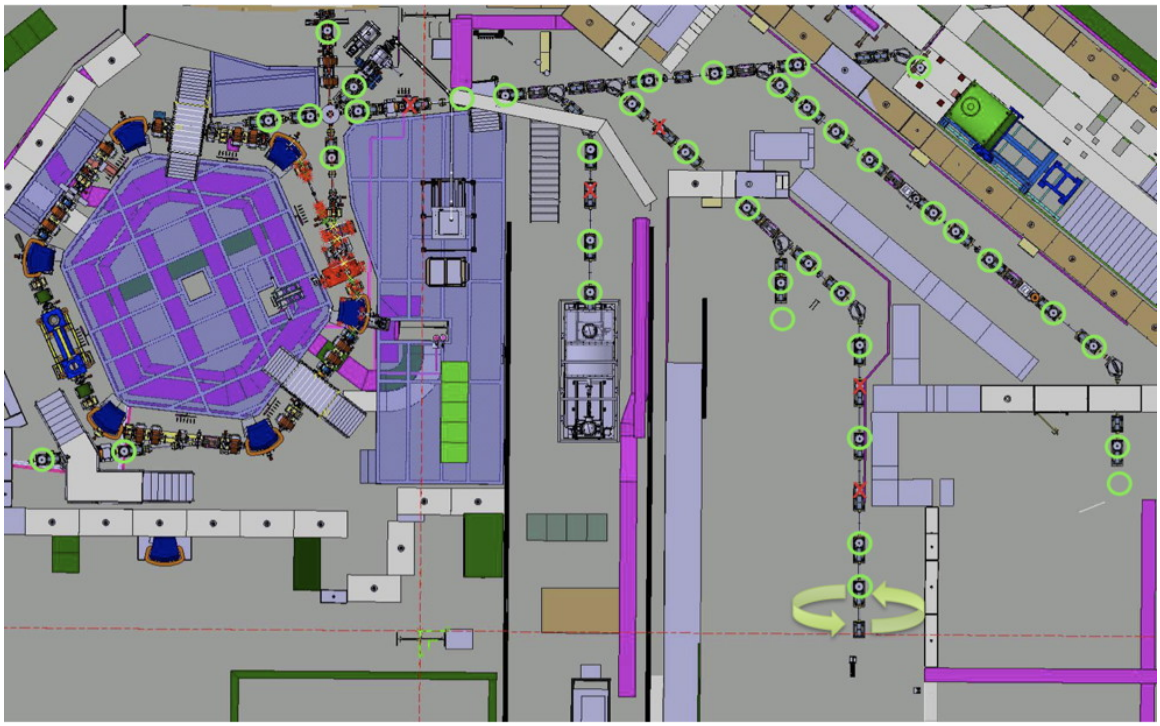

Figure 15 – Layout of ELENA facility indicating the positions of the 43 beam profile monitors which will be contributed by the ASACUSA collaboration.

Further large improvements would require laser resonances to be measured between pairs of metastable states with natural widths ($\sim$ 0.1 MHz) two orders of magnitude narrower than the transitions we have studied so far. This would require the use of 5 laser beams used in a so-called "pump-probe" geometry. In Fig. 13 (right), two laser pulses indicated by arrows 1–2 first depopulate the antiproton populations in states $(n, \ell) = (33, 32)$ and $(32, 31)$. This is followed by laser pulses 3–4 which induce the two-photon transition. The fifth laser pulse then probes for the resulting increase in the population of $(32, 31)$. The simulated signal of the new experiment is shown in Fig. 14 (c), indicating the highly improved spectral resolution.

2.3 Beam profile monitors for ELENA

As an in-kind contribution to the ELENA project of $\sim$ 2 MCHF, the ASACUSA $\bar{p}\mathrm{He}^+$ collaboration will supply 43 monitors to measure the spatial profiles of the antiproton and H^- beams in the injection, ejection, and user beamlines (see Fig. 15). The semi non-destructive nature of this monitor will be essential in ensuring that the four antiproton beam pulses circulating in ELENA of such low energy $E = 100$ keV and repetition rate $f \sim 0.01$ Hz can nevertheless be distributed in sequence to four simultaneous user experiments in an efficient and reliable way. On the other hand, the semi non-destructive design involves the detection of the femtocoulomb-scale electric charge induced by the small fraction of antiprotons intercepted by a series of thin wires in the high radiofrequency noise of the environment. Each device consists of,

1. 200 mm diameter vacuum chamber made of type 316L and 316LN stainless steel (Fig. 16). It was chemically cleaned and and heat treated to achieve a vacuum of $\sim 10^{-10}$ mb. All 43 monitor chambers have been delivered to CERN, most of which was installed in ELENA.

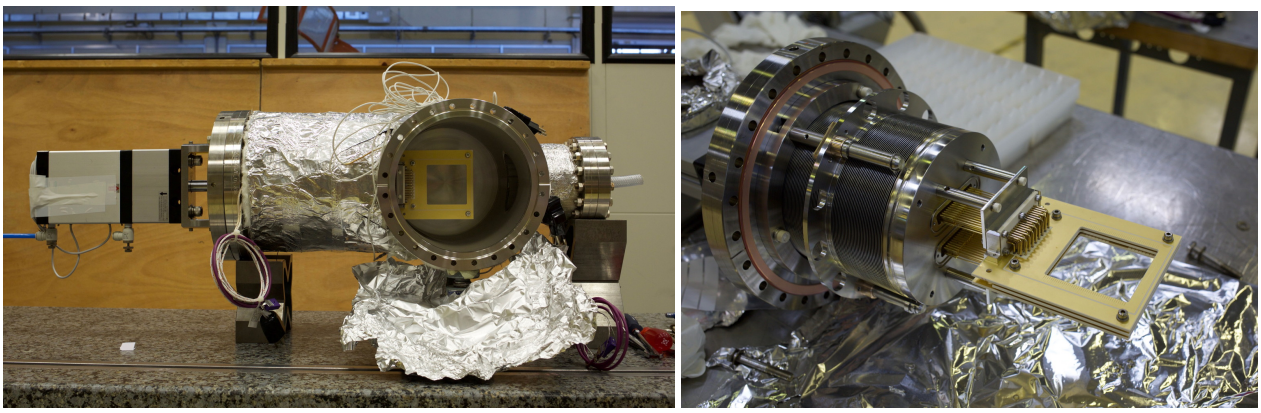

Figure 16 – Photographs of beam profile monitor, showing the vacuum chamber, the pneumatic translation stage with large-aperture bellows, and thick-film printed ceramic readout modules.

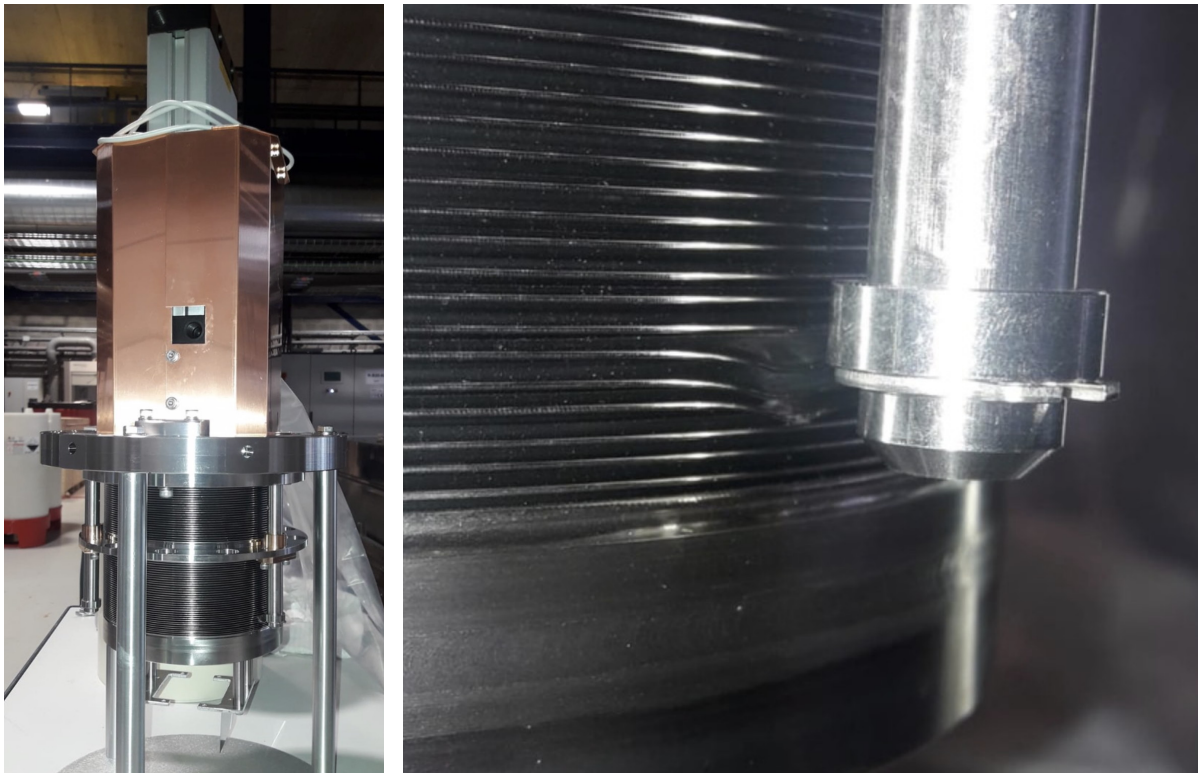

Figure 17 – Pneumatically actuated bellows unit of the beam profile monitor (left). Damage on the bellow presumably due to mechanical shocks during transport (right). Eleven units were found to have similar damage after 1 year of storage at CERN. The devices are now being repaired in Japan and will be returned soon.

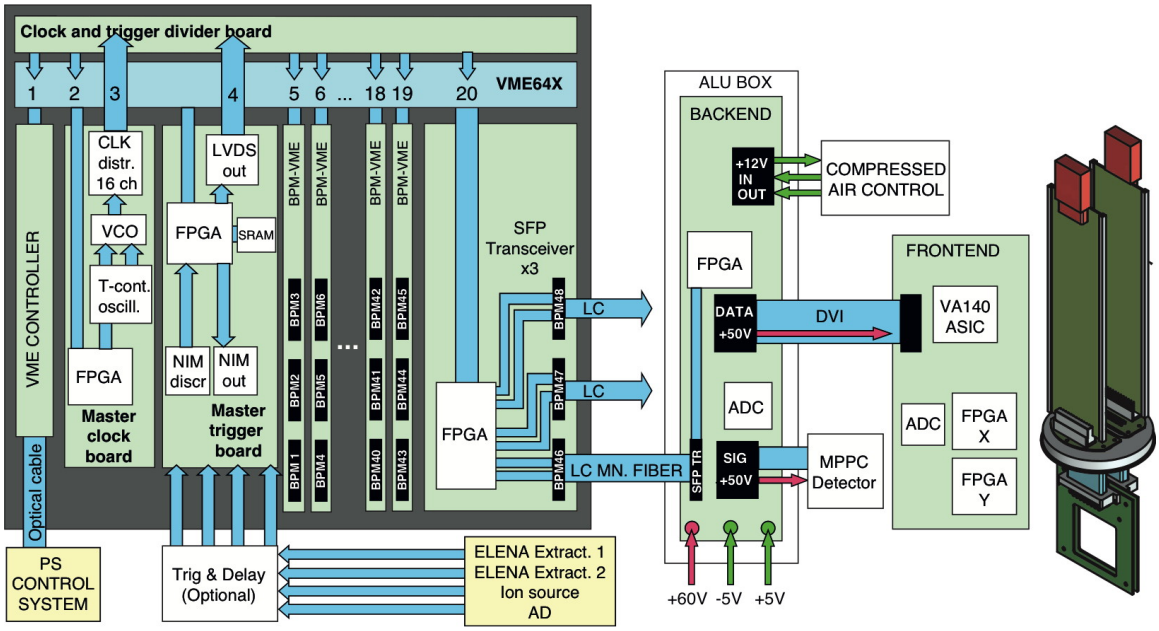

Figure 18 – Schematic diagram of the readout electronics of the beam profile monitor. The signals from the 48 horizontal and 48 vertical wires of the 42 monitors (i.e., 4032 readout channels in total) will be amplified by an application-specific integrated circuit (ASIC, IDEAS VA-140), digitized using a 12-bit analog-to-digital converter (ADC), and transmitted via optical fiber to a main VME64x crate located above the BASE experimental zone.

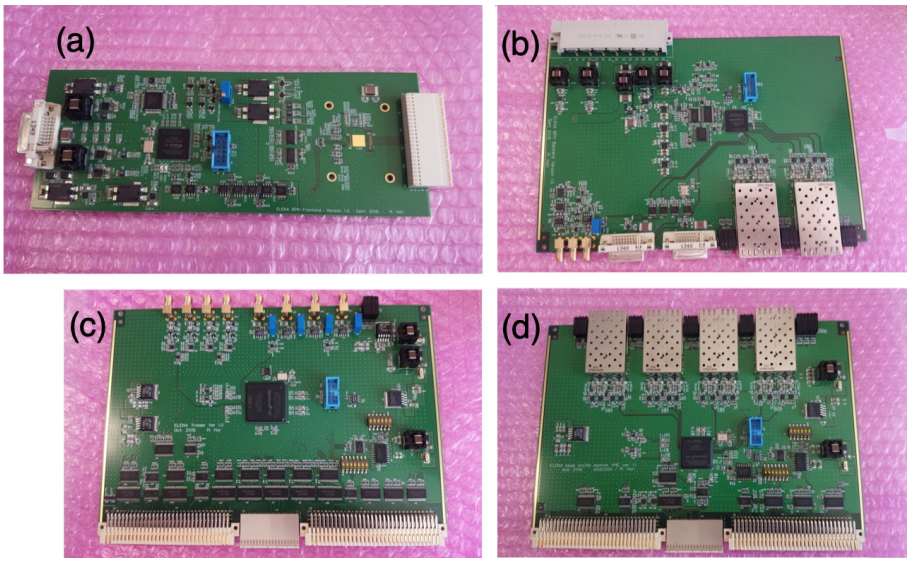

Figure 19 – Photos of the four printed circuit boards that comprise the beam profile monitor readout system. The charge induced on each of the 96 wires of the monitor are read out by an ASIC and ADC mounted on a preamplifier card (a). The profile data is then transmitted to an intermediate board (b) via LDVS signals and recorded in a FPGA. The data is then transmitted over 50–100 m via an optical fiber cable to a VME64x interface card (c). The triggers that signal the arrival of the antiproton or H^- beams are distributed by a separate VME64x card (d). The 45 boards of the type (b), 6 boards of the type (c), and 15 boards of the type (d) necessary for the facility have been delivered to CERN. The preamplifier board (a) is in a third iteration of prototyping following several modification requests from CERN accelerator specialists for features.

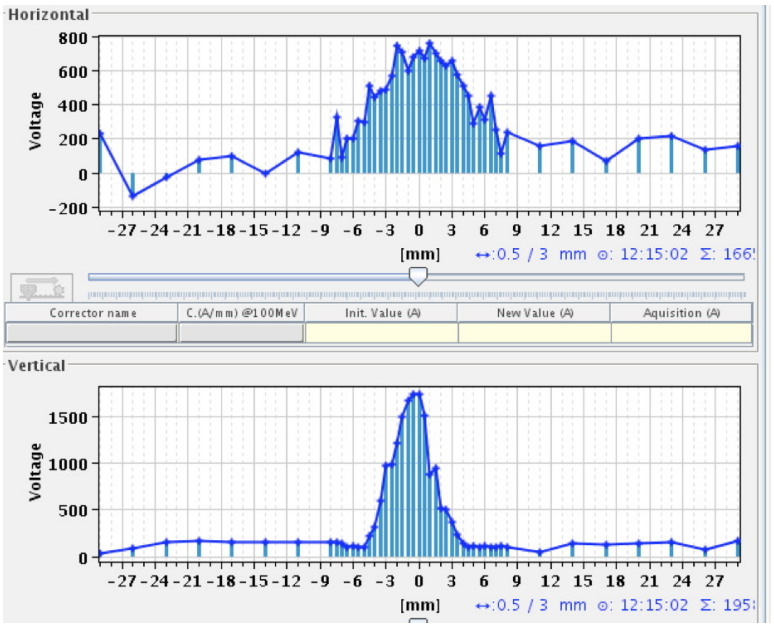

Figure 20 – Horizontal and vertical beam profiles of the 100 keV antiproton beam extracted from ELENA into the GBAR beamline measured by the BPM. The readout has been fully integrated into the PS control system.

2. Pneumatically-driven translation stage with large-diameter bellows, which allows the detector electrodes to be moved in and out of the beam path. Each device includes 100 feedthroughs to conduct the signals out from the vacuum chamber. After a 1 year storage at CERN, the vacuum bellows of 11 out of 43 devices were found to be mechanically damaged, possibly during transport (see Fig. 17). They are being repaired in Japan and will soon be returned to CERN.

3. Two position-sensitive cathode grids providing the X and Y projections of the beam, sandwiched between three anode grids with a distance $l = 2$ mm between them. The grids contained 48 gold-coated tungsten-rhenium wires of diameter 10–20 μm stretched over a ceramic frame, with a pitch 0.5–1.5 mm. 32 electrode sets corresponding to 5120 hand-welded wires were delivered to CERN so far. Some were found to have readout pins with loose contacts. The CERN specialist is investigating the possibility to repair the contacts using vacuum compatible silver adhesive.

Fig. 18 shows the readout system that measures the signals induced from the total 96 wires comprising each of the 43 monitors (i.e., 4128 channels in total). Each wire is read out by a 64-channel application-specific integrated circuit (ASIC, IDEAS VA-140) which includes a charge-sensitive preamplifier, shaping amplifier of time constant $\tau \sim 6.5$ μs, and a peak-hold circuit. The signals are digitized by a 12-bit analog-to-digital converter (ADC) and recorded by a field programmable gate array (FPGA). The spatial profile data are then transmitted over a pair of 50–100 m long optical fibers to two VME64x crates located above the BASE experimental zone. Front-end computers provides the interface to the CERN PS control system. Some 45 boards of the type (b), 6 boards of the type (c), and 15 boards of the type (d) necessary for the facility have been delivered to CERN. The preamplifier (a) is in a third iteration of prototyping, following several modification requests from CERN accelerator specialists for features.

In 2018 together with the CERN ELENA development team and the GBAR collaboration, we

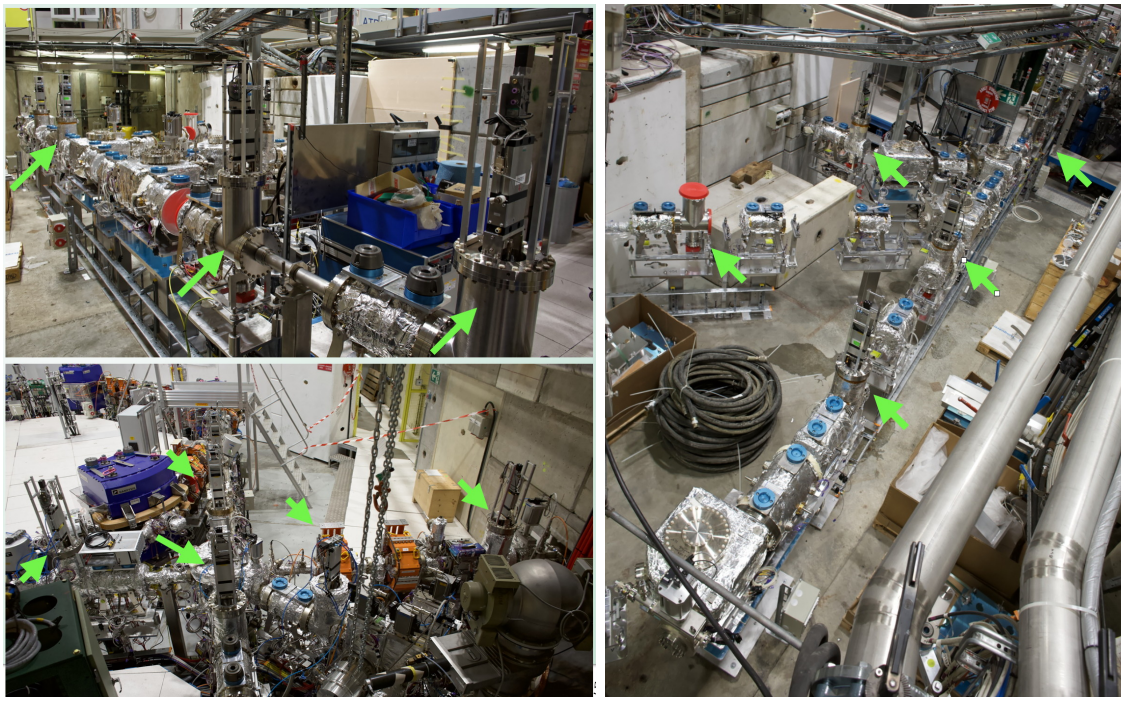

Figure 21 – Photographs of the electrostatic transport beamlines of ELENA in September 2019, with the positions of the beam profile monitors indicated by green arrows.

measured the spatial profiles of the 100 keV antiproton beam extracted from ELENA at three locations along the > 6 m long GBAR beamline. For this the readout of the devices were integrated into the PS control system architecture under nominal operational conditions. The typical horizontal and vertical profiles of the beam measured in this way are shown in Fig. 20. The beam was tentatively estimated to contain $\sim 5 \times 10^6$ antiprotons, with a beam emittance far smaller than $\sim 10\pi$ mm mrad. The fluctuation seen in the figure is partially due to the radiofrequency noise in the environment compared to the extremely low amplitude of the signal induced by the small number of antiprotons intercepted by the wire electrodes. Efforts to improve the S/N were carried out in 2019 by redesigning the preamplifier board with help from CERN specialists. The signal level is already sufficient to steer the beam through the beamline and operate the facility. We concluded that the $\overline{p}\mathrm{He}^+$ experiment will certainly be able to improve the precision on the transition frequencies using this beam as described in the previous section.

The drawings, FPGA programs, and maintenance and repair work for the beam profile monitors are being transferred to the appropriate specialists of CERN. ASACUSA thanks them for the collaboration.

2.4 Induction decelerator

For efficiently synthesizing $\overline{p}\mathrm{He}^+$ in the smallest possible volume within the experimental target, it is vital to carefully tune the energy of the antiproton beam that is allowed to traverse the entrance window of the target and come to rest in the helium gas. This tuning is currently achieved by varying an electrostatic potential applied to the electrodes of the radiofrequency quadrupole decelerator; a beam energy $E = 75$–80 keV is nominally used. The energy of the ELENA beam, on the other hand, will be fixed to $E = 100$ keV. While the experimental precision of the $\overline{p}\mathrm{He}^+$ spectroscopic measurements can be significantly improved by using the 100 keV ELENA beam in the initial

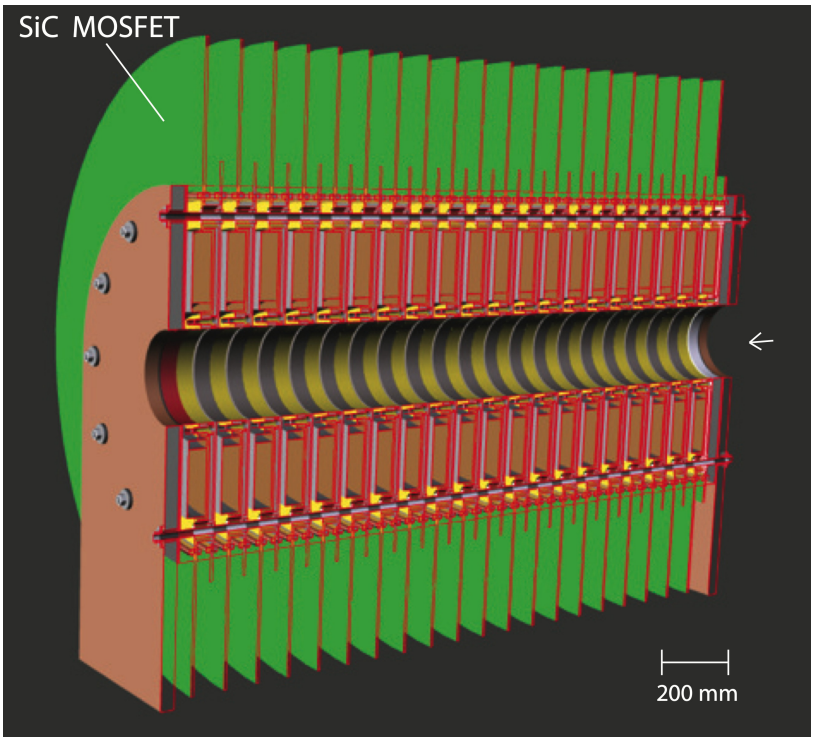

Figure 22 – Cross-section of the induction decelerator showing the 20 deceleration cells.

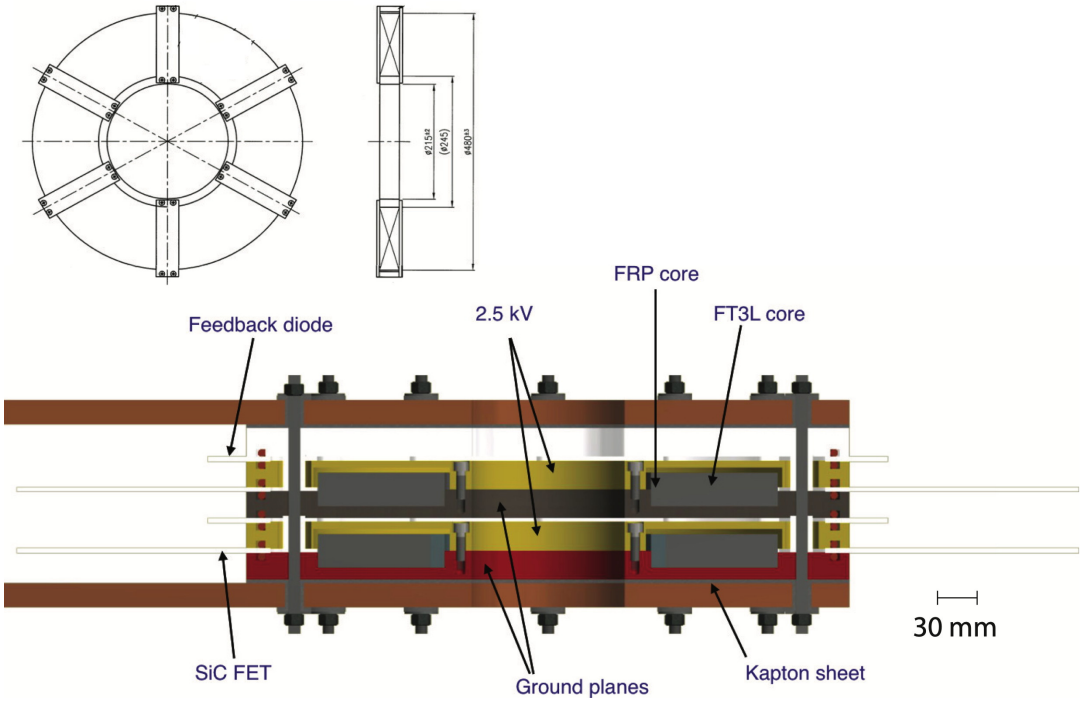

Figure 23 – Cross section of the prototype induction decelerator now under construction, for reducing the ELENA beam energy by ~ 4.6 keV

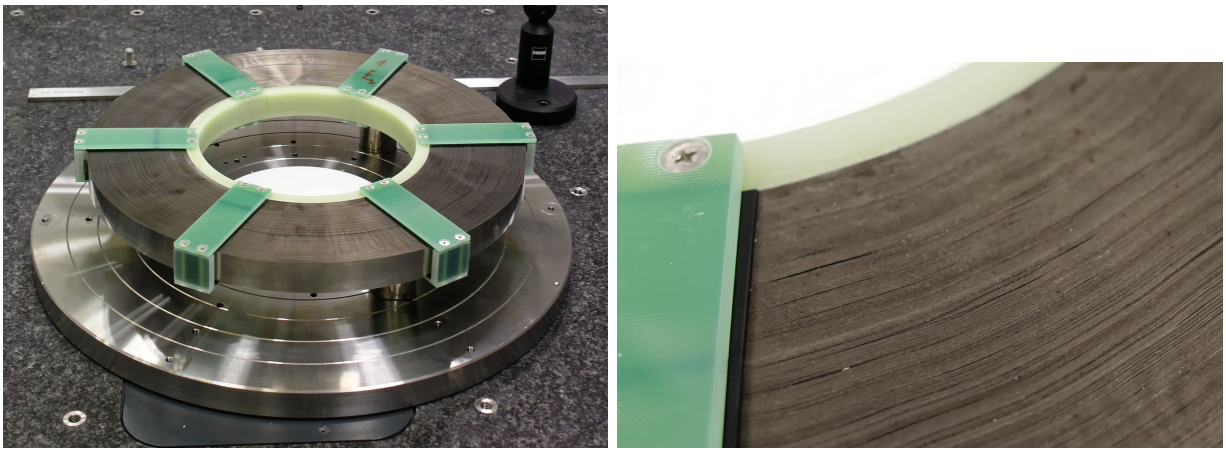

Figure 24 – Photograph of an induction core where nanocrystalline ferromagnetic material is deposited on the surface of a 18 μm thick ceramic strip and wound on a glass epoxy ring. 20–25 of these will eventually be used to decelerate the antiprotons to < 50 keV in Phase2b of the experiment.

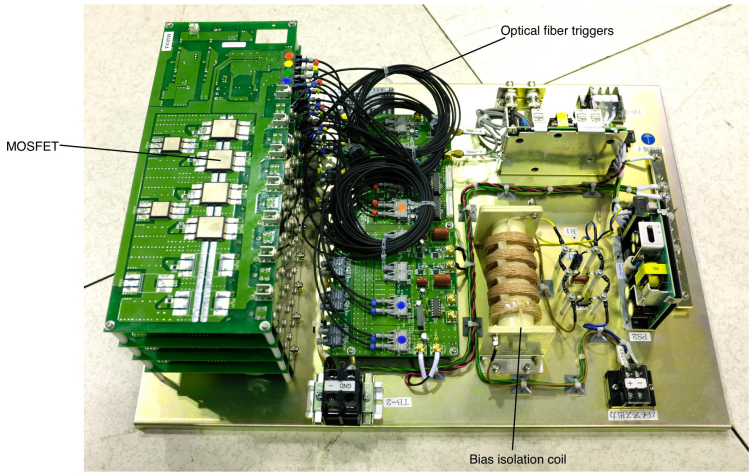

Figure 25 – Photograph of the test Marx high voltage pulsar which produces 500-ns-long current pulses of amplitude $V \sim 2.3$ kV and $I \sim 100$ A. The device is based on MOSFET semiconductors.

stage of experiments, even larger improvements can be realized by using a lower-energy (< 50 keV) antiproton beam in a latter series of experiments in > 2021.

We therefore began development of a linear induction decelerator to reduce the energy of the beam from 100 keV to < 50 keV. Following the first measurements using our ELENA beam profile monitors in 2018, we obtained the realistic dimensions, emittances, and pulse lengths of the antiproton beam on which the design of the induction decelerator could be based. The device consists of a series of $d \sim 500$ mm diameter magnetic cores of wound ceramic ribbons of width 35 mm and thickness 18 μm, onto which are deposited nanocrystalline alloys. The core is wound on a mechanical support ring made of glass epoxy. The cores are characterized by a high magnetizing inductance, low ohmic losses when energized, very low remanent (DC) magnetic field, and a relatively high saturating field. Each core [73–75]. is excited by 500-ns-long pulses of peak current $I \sim 200$–300 A and amplitude $V \sim 2$ kV using arrays of high-voltage semiconductor switches. This induces a decelerating electric field along the walls of a vacuum pipe positioned within the stacked magnetic cores. The device is triggered in synchronization with the arrival of the antiproton beam

from ELENA. As an example, 25 such cores would decelerate the antiprotons by 25×2 kV=50 keV, not counting some additional cores that would be needed to compensate for deviations in the pulsed current applied to the cores.

The advantages of an induction decelerator compared to other types of radiofrequency or electrostatic decelerator designs may include the simple structure of the in-vacuo components (i.e., a single vacuum pipe with no high voltage vacuum feedthroughs or internal electrodes) and the larger acceptance. All the complicated parts of the decelerator are located externally to the beampipe where they can be readily serviced. This may be important for $\overline{p}\mathrm{He}^+$ experiments which involve a cryogenic helium target that presents a gas load to the vacuum system that may cause, e.g., a radiofrequency or electrostatic device to discharge. Each core is excited with a relatively low (~ 2 kV) voltage, so that electromagnetic noise that could disturb our high-precision laser spectroscopy measurements would be minimized. The length of the device is relatively small $l \sim 1$ m, and divided into multiple subsections with a focusing element in between, helping to reduce the diameter of the decelerated beam. The disadvantages of an induction decelerator design include the high cost, large volume, and weight of the magnetic cores, and the difficulty in energizing the cores with a high current pulse of sufficiently uniform ($< 1\%$) amplitude. Any variance in the amplitude of the pulse would lead to an increase in the energy spread of the antiproton beam.

Semiconductor switches will be mounted about 300 mm from the magnetic cores to generate the high current pulses. Fig. 25 shows a 4-stage Marx-type pulsed power supply based on silicon N-type MOSFETs which was provisionally built in 2017 for the project. It is a modified version of a commercial design adopted by the JPARC 3-GeV rapid-cycling proton synchrotron (RCS) facility to drive some kicker elements in its secondary muon beamlines at $f = 25$ Hz rates. It produced 500-ns-long current pulses of amplitude $V \sim 2.3$ kV and $I \sim 105$ A, with close to the required pulse uniformity. This enabled us to test two cores of the induction decelerator. We are now constructing another power supply based on a 1200 V SiC MOSFETs.

2.5 Cryogenic target

The RFQD beam of large emittance could only be efficiently intercepted by a relatively large experimental target (see Fig. 26 (left)) where the samples of atoms were distributed over a ~ 30 mm diameter volume. A significant portion ($> 30\%$) of the antiprotons came to rest in the walls of the target instead of producing $\overline{p}\mathrm{He}^+$, and became a strong background source. High-power lasers were needed to irradiate this volume with a sufficient intensity of light to carry out the spectroscopy. The systematic experiments and theoretical calculations carried out in 2018 showed that some $\overline{p}\mathrm{He}^+$ atoms are produced in regions of the experimental target which are not irradiated by the laser. This leads to reductions in the signal-to-noise (S/N) ratio and the rate of accumulating events in the experiment.

By using the ELENA beam, the $\overline{p}\mathrm{He}^+$ can be formed in a smaller volume (simulations based on the roughly-measured ELENA beam characteristics imply < 7 mm diameter) so that a smaller target chamber (Fig. 26 (right)) can be used instead. This reduction in the sample volume of factor $\sim 1/20$ implies large improvements in the signal-to-noise ratio of the spectroscopic signal. Lasers of lower power and higher precision can then be used. The small thermal mass and smaller windows of the target also allows it to be cooled to lower temperatures than before. For this we began the design of a new cryostat in which $\overline{p}\mathrm{He}^+$ will be produced and cooled by collisional gas buffer cooling to temperature $T < 1$ K. Design of the three layers of thermal radiation shielding and vacuum chamber are underway. The total thermal load was calculated (see Fig. 27). These efforts are carried out in collaboration with J. Kuczynska and T. Koettig of CERN.

With theoretical help on the nuclear stopping powers and multiple scattering of antiprotons

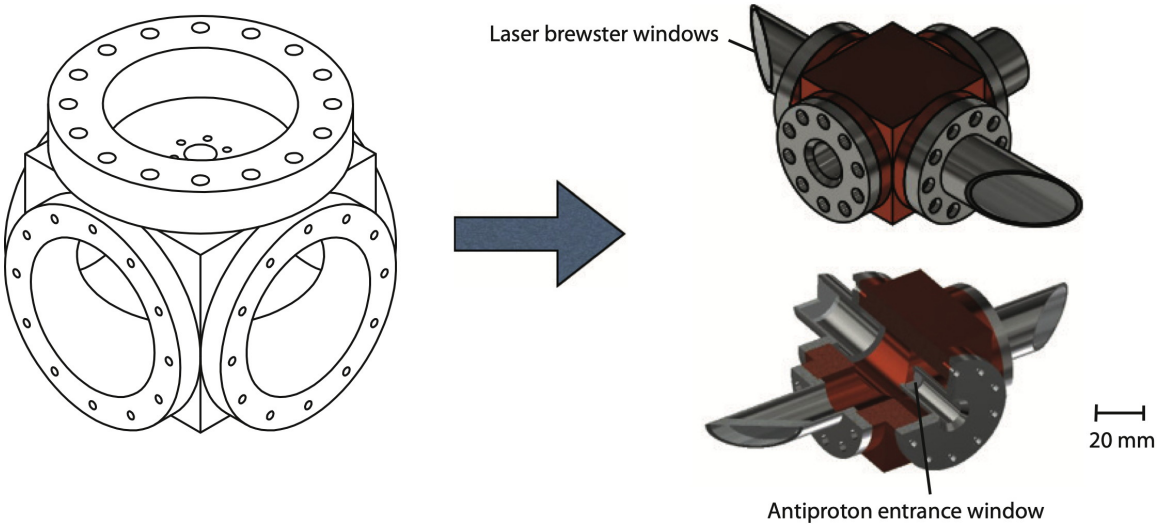

Figure 26 – Schematic diagrams of the cryogenic helium targets used for $\overline{p}\mathrm{He}^+$ spectroscopy experiments based on the antiproton beam provided by the RFQD (left) and the ELENA beam of much smaller emittance (right). Note how the atoms will be synthesized in a much smaller volume of gas in the latter case.

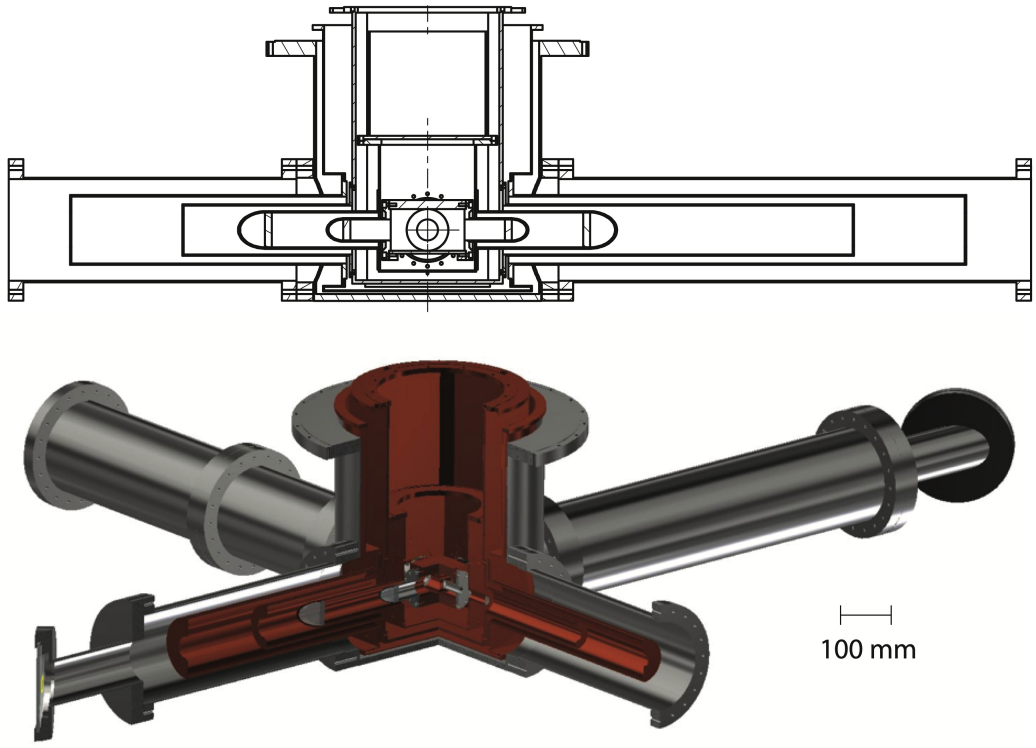

Figure 27 – Cross section of the new cryogenic helium target for ELENA. The target chamber is surrounded by three layers of radiation shielding.

traversing thin Mylar foils provided by the University of Helsinki, we carried out systematic studies to identify the experimental target conditions that would optimize the $\overline{p}\mathrm{He}^+$ spectroscopic signal at various antiproton beam energies. In the experiment, the energy of the antiprotons that emerged from the RFQD was varied between $E_{\overline{p}} = 63$ and 100 keV by biasing its electrodes. The signal-to-noise ratio and intensity of the resulting signal was compared with the theoretical expectations. Quantum chemical methods were used to determine the intraparticle potential between the antiprotons and the elements comprising the Mylar foil. From this the nuclear stopping power and data used to simulate the antiproton motion based on a molecular dynamics range calculation code MDRANGE was obtained [76]. The electronic stopping power was estimated by comparing the existing low-energy experimental values of other materials for antiproton and proton projectiles and obtaining an empirical ratio function.

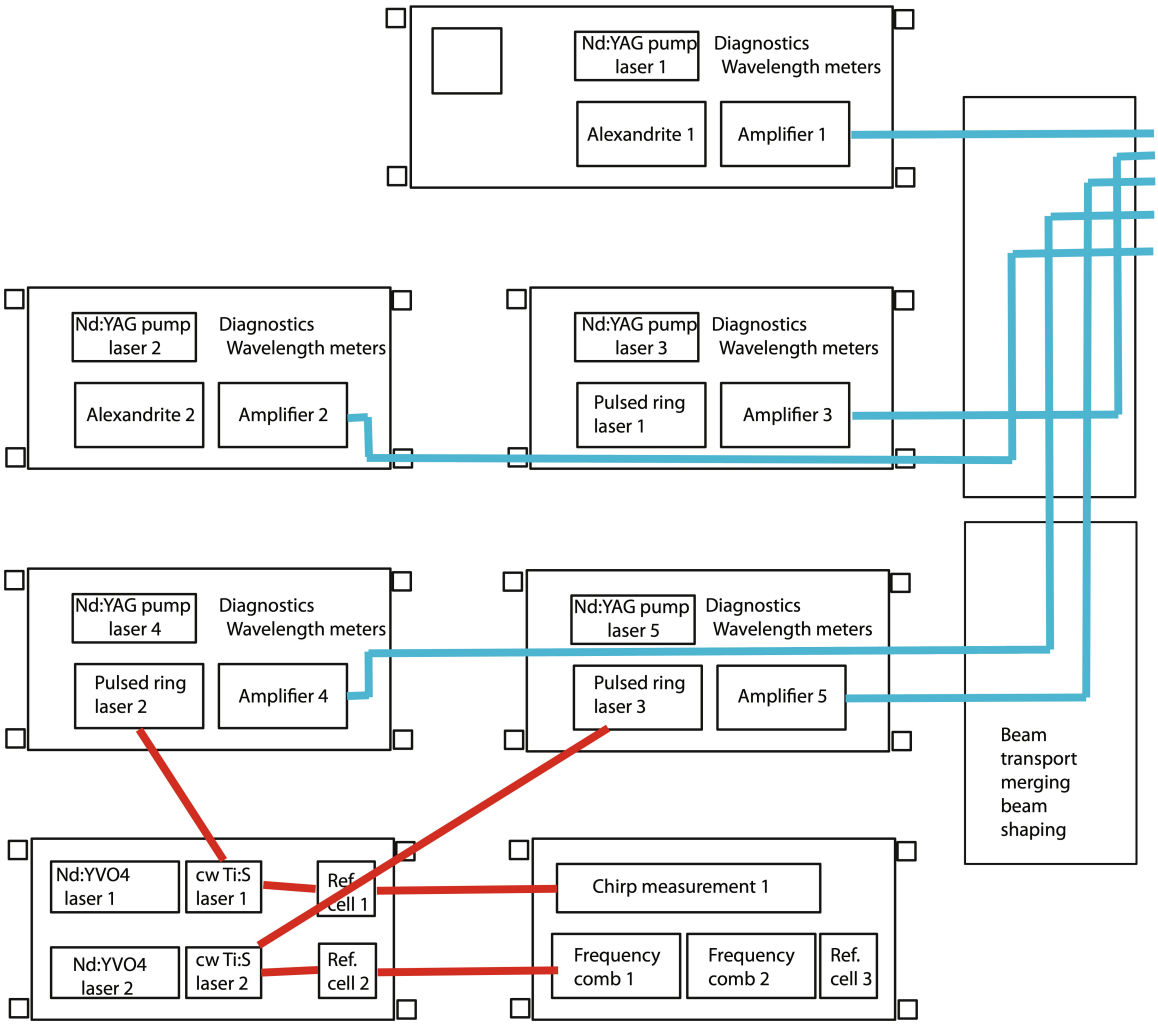

Figure 28 – Layout of the laser system needed for high precision spectroscopy of $\overline{p}\mathrm{He}^+$. The system involves the generation of five laser pulses that would irradiate the atoms in sequence, and spans 9 optical tables of typical size 3×1.5 m. The trajectories of the laser beams will be covered for safety.

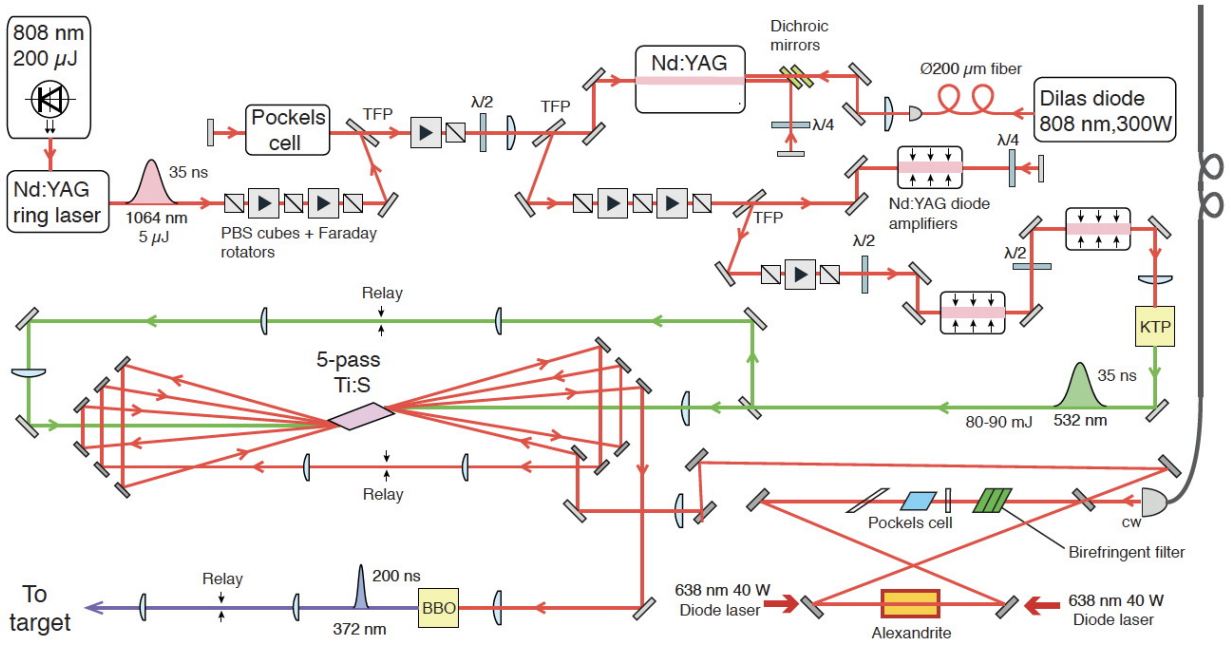

Figure 29 – Schematic diagram of proposed new laser system for two-photon laser spectroscopy of antiprotonic helium. A diode-pumped alexandrite pulsed laser is used to generate a 200-300 ns long laser pulse of energy 1 mJ. The output is amplified in a 5-pass Ti:Sapphire amplifier to 12 mJ, before being frequency doubled in a BBO crystal. A new diode-pumped Nd:YAG pump laser ensures a narrowband and stable output energy for the Ti:Sapphire amplifier.

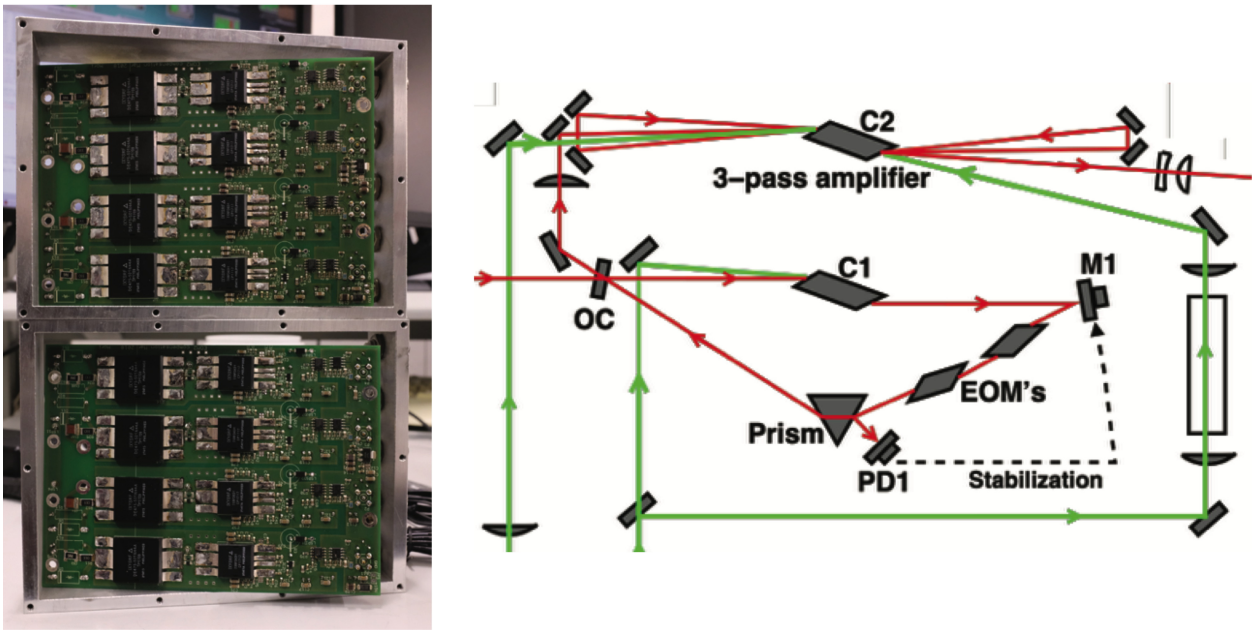

Figure 30 – Photo of the silicon MOS-FET based high-speed, high-voltage system for precisely compensating for the frequency excursions of the laser using an intracavity electro-optic modulator (left). Schematic drawing of one of the laser oscillators used in the experiment (right).

Figure 31 – Photograph of the laser hut in September 2019, after the new extension to the room. The first 2 m of the hut closer to the camera will be cut in spring of 2020 to accommodate a possible new experimental area requested by CERN. The equipment inside the hut must be moved before this.

2.6 Laser system

The experiment needs a large (five) number of laser systems at wavelengths $\lambda = 264$ nm to 470 nm (see Fig. 28). Our current two-photon experiments are based on nanosecond injection-seeded pulsed Ti:Sapphire lasers pumped by a flashlamp Nd:YAG laser of pulse length 3 ns. Their spectral resolutions (> 6 MHz) are limited by the finite (< 100 ns) laser pulse length and by the spurious frequency modulation induced during the amplification [72]. We are investigating various methods to improve the stability and spectral resolution of the lasers. One method involves the use of a single-mode diode-pumped Nd:YAG laser of pulse length 50 ns (see Fig. 29). Five lasers of this type are currently being constructed at Max Planck Institute of Quantum Optics. The Ti:Sapphire lasers have the advantage of a broader tuning range and higher single pass gain, and remains the baseline solution. A new servo system based on a series of eight high-voltage (1 kV) silicon MOSFETs each driven by 30 V MOSFETs which compensated for the small frequency excursions in a single mode, pulse ring Ti:Sapphire laser was developed and used to improve the resolution on the $\overline{p}\mathrm{He}^+$ spectral data in 2018. Numerous small improvements were made to the laser systems.

Alexandrite laser crystals (see Fig. 29) have a longer fluorescence lifetime ($> 200\mu$s) and lower single-pass gain compared to Ti:Sapphire; this supports the generation of longer (> 200–300 ns) laser pulses of correspondingly higher spectral resolution. Previous developmental work based on chirp-compensated flashlamp-pumped alexandrite crystals showed resolutions of < 5 MHz. One possibility is to construct a diode-pumped alexandrite laser to further reduce this resolution, taking advantage of the recent availability of high-power diode lasers that emit in the visible wavelength $\lambda = 638$ nm. Due to the limited power of the laser diodes, the output energy of the alexandrite oscillator is expected to be around 1 mJ. As before, the beam will be further amplified to E=15 mJ in an existing Ti:Sapphire multipass amplifier, before being frequency-doubled or tripled in lithium triborate (LBO) and beta-barium borate (BBO) crystals.

The laser powers needed for the measurement is dependent on the diameter of the sample of $\overline{p}\mathrm{He}^+$ produced in the target. As the induction decelerator and later the extracted beam from an antiproton trap are developed, the necessary laser energy would decrease, enabling higher precision

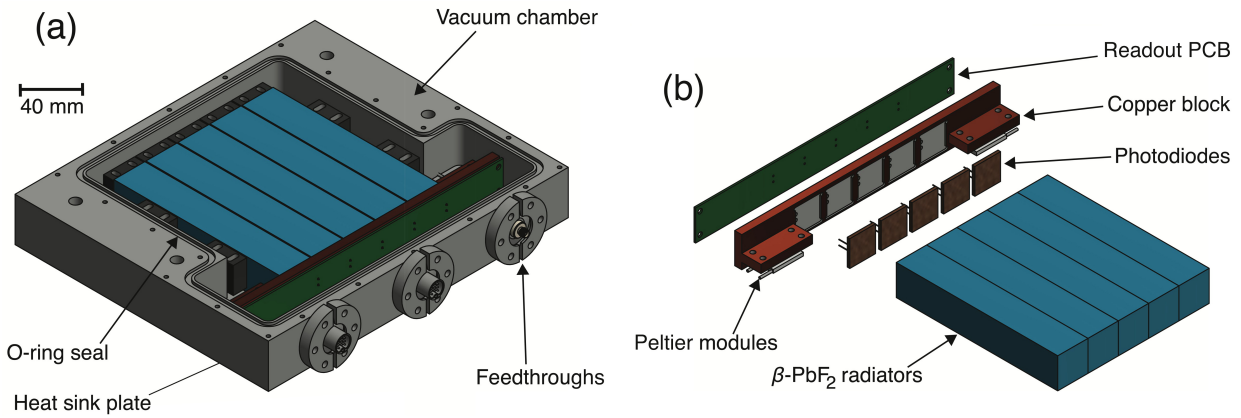

Figure 32 – (a) Layout of the Cherenkov detector hermetically sealed in an aluminum chamber. (b) Details of the β-PbF_2 radiator, photodiodes, copper block, printed circuit board (PCB), and Peltier thermoelectric modules.

spectroscopy. Of vital importance is the need to stabilize the optical frequency of the two lasers corresponding to 3 and 4 in Fig. 13 during the $0.3-1$ μs interval of the two-photon transition. For this we are developing laser systems stabilized on optical cavities of high finesse, and a chain of frequency reference standards based on global positioning satellites, two types of atomic frequency standards, a low-noise quartz oscillator, and an erbium fiber frequency comb. Calculations with metrological experts indicate that a measurement precision of 10^{-11} on the optical frequency is feasible.

The new laser systems involve the use of 9 laser tables of typical size 3×1.5 m which fills the floor space in the existing laser hut of ASACUSA. CERN has requested that we cut a significant portion of the laser room (Fig. 31) so that the space could be used for a future experiment by a different collaboration. This involves temporarily moving the sensitive optics in the hut to a different location, extending the laser hut in a new direction to compensate for the lost space, cutting the laser hut including the air conditioning, electronic power, and cabling, and then building the new laser system. The new extension to the laser hut was recently completed, and we have begun the move so that the old part can be cut in spring 2020. This involves significant manpower and investment over ~ 6 months.

2.7 Detectors

These experiments will be carried out using $\Delta t < 200$ ns long pulsed beams containing $N_{\overline{p}} \sim 8 \times 10^6$ antiprotons. As in the experiments using the RFQD, the arrival of individual antiprotons in the helium target will not be resolved. We will instead determine the relative intensity and temporal structure of the beam by using acrylic Cherenkov detectors to measure the flux of secondary charged particles that emerged from the simultaneous annihilations in the apparatus. Past experiments show (see Ref. [77] and references therein) that on average some 1.5 π^+ mesons, 1.8 π^- mesons, and 2 π^0 mesons emerge from a $\overline{p}$+^{4}He annihilation, and that the momentum of most of the pions are distributed between $p = 0.1$ and 0.9 GeV/c. The π^0 mesons preferentially decay into two γ rays while still inside the target. The annihilations also lead to fission of the target nuclei, and the emission of fast and slow neutrons. We will utilized fine-mesh photomultiplier tubes [77] which have signal responses that were highly linear to read out the Cherenkov radiators.

We have also developed extruded scintillator arrays [78, 79] and a different Cherenkov detector

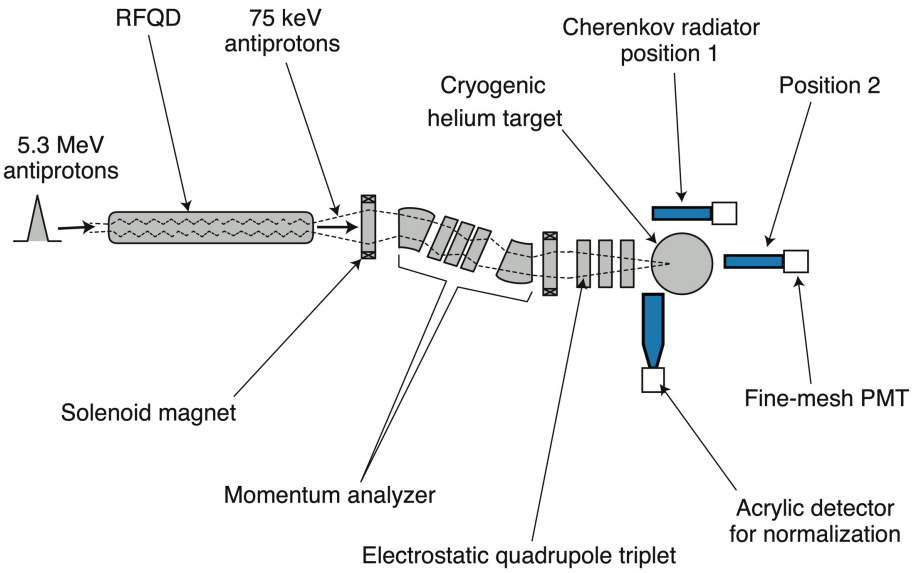

Figure 33 – Experimental layout used to measure the responses of Cherenkov radiators against antiproton annihilations (not to scale). Dashed lines show the trajectory of the antiproton beam. The antiprotons were decelerated to $E = 75$ keV by allowing them to pass through a radiofrequency quadrupole decelerator (RFQD). A momentum analyzer beamline selected the 75 keV antiprotons and transported them to a cryogenic target chamber filled with helium gas. The Cherenkov radiators were placed at two locations indicated by positions 1 and 2. A separate acrylic Cherenkov radiator read out by a fine-mesh photomultiplier tube was used to measure the intensity of the antiproton beam and normalize the data, see text.

[80] that consisted of an array of five lead fluoride crystals in the cubic phase (β-PbF_2) [81–84] of size 30 mm×30 mm×160 mm and tested them. The arrival of antiproton pulses at the experimental target produced an intense flash of Cherenkov light in each crystal; this was measured by a reverse-type avalanche photodiode (APD) of active area 10 mm ×10 mm. These crystals are sensitive to both the charged secondary particles and γ-rays [77] that emerge from antiproton annihilations, and have a higher light yield compared to Cherenkov detectors based on acrylic radiators of the same size. Other advantages of the detector include its compact size and insensitivity to magnetic fields. We compared the light yields of Cherenkov radiators made of β-PbF_2, fused silica, acrylic, lead glass, and a lead-free, high-refractive index glass against antiproton annihilations.

The five β-PbF_2 crystals (Fig. 32) were wrapped in two layers of a polyvinylidene fluoride membrane which constituted a diffusive reflector. The assembly was cooled to a temperature $T \sim 19$ °C using two Peltier thermoelectric modules that were regulated by a proportional–integral–differential controller. The detector was housed in a 290 mm×245 mm×50 mm aluminum chamber, hermetically sealed and purged with nitrogen to prevent condensation on the cooled photodiodes and β-PbF_2 crystals that may arise from the high humidity in the vicinity of the cryogenic target. The chamber also shielded the photodiodes against the electromagnetic interference of frequency range $f = 10$–200 MHz that was emitted from the AD and radiofrequency quadrupole decelerator (RFQD).

The β-PbF_2 crystals were grown using the Bridgman method and all surfaces polished by the Shanghai Institute of Ceramics, Chinese Academy of Sciences (SICCAS). Cherenkov radiators of the same size made of fused silica (CoorsTek T-4040), UV transparent grade acrylic plastic (Nitto Jushi Kogyo Co. Clarex S-0), high transmission grade lead glass (Schott AG SF57HTultra), and

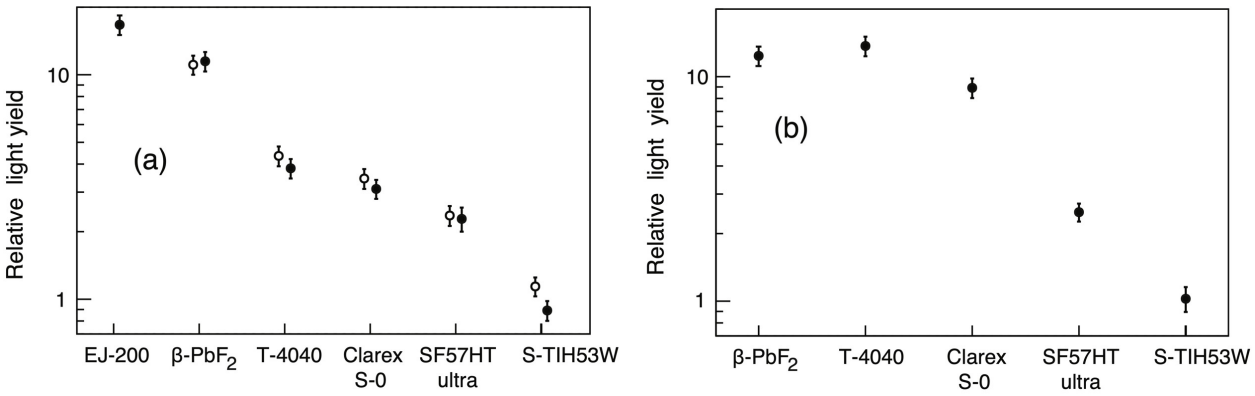

Figure 34 – Relative light yields of various Cherenkov radiators against antiproton annihilations measured by placing the detector at the two positions 1 (a) and 2 (b) indicated in Fig. 33. The radiators include lead fluoride (β-PbF_2), fused silica (T-4040), UV transparent acrylic (Clarex S-0), lead glass (SF57HTultra) and lead-free high refractive index glass (S-TIH53W). For the light yields measured at position 1, no significant differences were seen between detector configurations with (indicated by open circles) and without (filled circles) a silicone light coupler placed between the radiator and a fine-mesh photomultiplier, see text. The light yield of a plastic scintillator (EJ-200) is also shown.

Ohara S-TIH53W glass were also manufactured. The last of these was a lead-free glass with a high refractive index $n_r \sim 1.8$, density $\rho = 3.5$ g/cm^3, and partial dispersion of Abbe number $\nu_d \sim 23.8$. X-ray photoelectron spectroscopy measurements on ground samples of the glass showed that it contained barium, titanium, and niobium oxides. These "eco-friendly" alternatives to conventional flint glass generally have reduced transmission at blue and UV wavelengths.

The silicon APD's were of the so-called reverse type, where the p-n junction of high field in which multiplication takes place was typically located about ~ 5 μm from the illuminated surface of the sensor. Visible photons were absorbed and generated electron-hole pairs within the first few microns of the depletion region. These electrons were collected and underwent multiplication with the highest gain. Although charged particles, X-rays, and neutrons traversing the APD generated primary ion pairs over the entire width of the photodiode, only those pairs that originated in the thin p-type layer preceding the high-field p-n junction underwent high-gain multiplication. This lead to a small ($t_r < 6$ μm) effective thickness of the device with regards to the nuclear counting effect (NCE) against ionizing radiation, which was measured using a ^{90}Sr source.

The schematic layout of the experimental setup used to measure the relative light yields Γ of the Cherenkov radiators against antiproton annihilations are shown in Fig. 33 [9,10]. The 75 keV beam slowed down by the RFQD was transported by a momentum analyzer beamline and transported to a cryogenic helium target. The antiprotons came to rest in the helium or metallic walls of the target chamber and underwent nuclear absorption and annihilation. A single β-PbF_2 crystal was oriented so that either its short (indicated by position 1 in Fig. 33) or long (position 2) axis aligned towards the center of the experimental target at a distance ~ 150 mm. The Cherenkov light produced in the crystal by the antiproton annihilations were measured by a fine-mesh photomultiplier tube [77] with a bialkali photocathode of diameter $d = 17.5$ mm and an entrance window made of borosilicate glass. The photomultiplier had a quantum efficiency of $> 20\%$ at wavelengths $\lambda = 380$–440 nm. The photon yields at position 1 were measured with and without a transparent $t_d = 5$ mm thick disk made of a two-component silicone rubber inserted between the radiator and the entrance window of the photomultiplier to improve the optical coupling. The relative intensity of each antiproton pulse was normalized using the readout of a second Cherenkov detector of size 480 mm$\times$160 mm$\times$20 mm

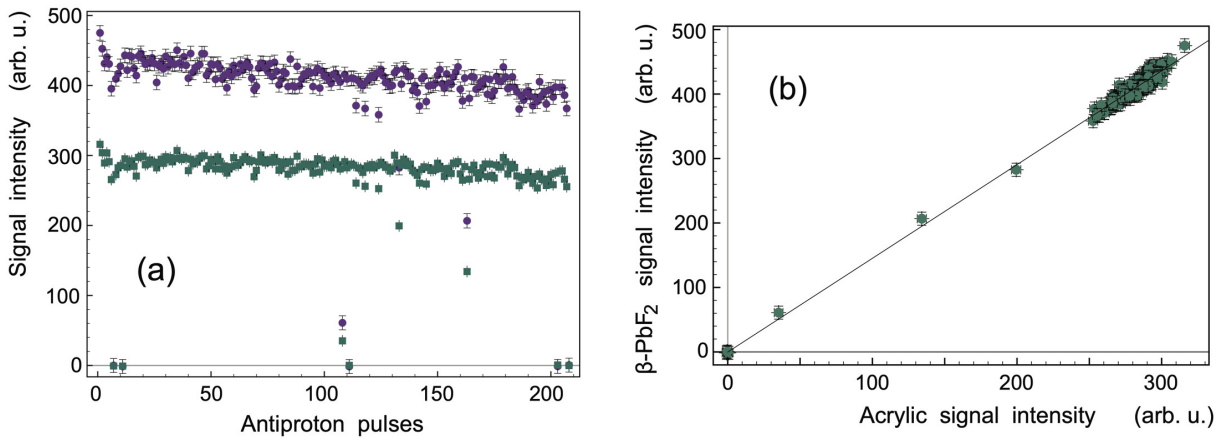

Figure 35 – (a) Relative intensities of 205 antiproton pulses arriving at the cryogenic helium target, measured using an array of β-PbF_2 Cherenkov radiators read out by APD's (filled circles) and an acrylic radiator read out by a fine-mesh photomultiplier tube (squares). (b) Correlation between the signal intensities of the two Cherenkov detectors.

made of UV-transparent acrylic. The detector was positioned 400 mm away from the target, so that the solid angle seen from the target was $\sim 1\%$.

The relative light yields Γ of the five radiators and plastic scintillator measured at position 1 are compared in Fig. 34(a). Each data point represents the average of measurements collected over 30 antiproton pulses, using three samples of each radiator type. The β-PbF2 crystals showed the highest light yield that was a factor three larger than the Γ values of the fused silica and acrylic radiators. This is due to the short radiation length and high refractive index of β-PbF2 that allowed the efficient detection of γ-rays and low-momentum pions. Primarily because of the low transparencies at short wavelengths, the lead glass and S-TIH53W radiators showed light yields that were factors of 5 and 10 smaller compared to β-PbF_2, respectively. No significant differences were seen between the Γ-values measured with (indicated by open circles) and without (filled circles) the silicone light coupler placed between the radiators and photomultiplier.

Fig. 34(b) shows the light yields measured with the five radiator types placed at position 2. The Γ-values of the fused silica and β-PbF_2 radiators are now approximately equal, despite the factor ~ 13 shorter radiation length of the latter material. This is believed to be due to the lower transparency of β-PbF_2 compared to fused silica which results in the absorption of a significant number of those UV Cherenkov photons that were produced in the part of the crystal closest to the experimental target, that prevent them from reaching the photomultiplier.

Fig. 35(a) shows the relative intensities of 205 antiproton pulses that were decelerated by the RFQD over a 8 h period, measured using the β-PbF_2 Cherenkov detector array read out by APD's (indicated by filled circles). We simultaneously measured the response of the acrylic Cherenkov detector read out by a fine-mesh photomultiplier (filled squares), which is known to be highly linear at these beam intensities [77]. The shot-to-shot fluctuations seen here were primarily caused by variations in the number of antiprotons that were created in the production target of the AD. The correlation between the intensity measurements made by the two detectors [Fig. 35(b)] indicates that the linearity of the β-PbF_2 Cherenkov detector array is better than 5%. The residual nonlinearity is assumed to be mostly due to the contribution of the NCE and the response of the APD at high light intensities. Time- and temperature-dependent shifts in the APD gain were estimated to be of order $\sim 2\%$.

We concluded that the linearity and dynamic range of the Cherenkov detector with fine mesh

Phase	1	2a	2b	3
Year	2015-18	2021-	2023-	2026-
Decelerator	RFQD	ELENA	ELENA+induction	Paul trap
Beam energy	85 keV	100 keV	50–85 keV	~ 1 eV
Emittance	100π mm mrad	$< 5\pi$ mm mrad		
Statistics	$1\times$	$5\times$	$7\times$	
S/N ratio	$1\times$	$3\times$	$5\times$	
Natural width (ΔE resolution)	> 15 MHz	0.1 MHz		
Atom temperature	1.5 K	1.5 K	0.4 K	0.1 K
Precision	$\sim 10^{-9}$	$\sim 10^{-10}$	$\sim 10^{-11}$	$\leq 10^{-11}$
Laser beams	2	5		
Milestone		Find narrow resonance	Improve precision	Single collision

Table 2 – The four phases of planning of the $\overline{p}\mathrm{He}^+$ experiment.

photomultiplier or APD readout satisfies the requirements of our experiment in the ELENA era. The detectors are hence fully ready for measurements in 2021.

3 Planning and funding

The experimental programme is divided into four stages, the first of which was completed using the RFQD in 2018 (see Table 2) and several publications are being prepared. Phase 2a starting in 2021 seeks to discover the narrow resonances of $\overline{p}\mathrm{He}^+$ using the 100 keV beam of ELENA. This can be initially started with 3 laser beams, which would be followed by 5 laser beams as the complexity of the experiment is gradually increased. Most of the equipment needed for this initial phase already exists, or must be modified for ELENA. The new extension of the laser hut was carried out through August-September 2019, and we are discussing about the installation of new safety interlocks to the doors. During Phase 2a/b the laser system will be gradually upgraded to reduce the systematic uncertainties in measuring the optical frequency. This involves new Nd:YAG pump lasers and Ti:Sapphire lasers, as well as an upgrade of the erbium frequency comb. These efforts are currently being pursued in Max Planck Institute for Quantum Optics. In the CERN laser hut, old electronics equipment and data acquisition systems are being replaced.

The existing cryogenic target will be modified with a ^{3}He constant Joule-Thompson cryocooler to allow cooling of the atoms to temperature 0.4 K, but initial efforts at searching for the narrow $\overline{p}\mathrm{He}^+$ resonance can start with the easier-to-operate $T = 1.6$ K temperature.

The RFQD and amplifier were removed in February 2019, followed by installation of the ELENA beamline between June and August. The 11 beam profile monitors needed to complete the beamlines are being repaired in Japan and will be ready in the next months. These monitors remain a priority as they are absolutely essential for tuning the antiprotons to the experiments in phase 2a. On the electronic readout side, most of the electronics are in place with the exception of two components, a) the preamplifier boards with the ASICs that will be directly connected to the monitor electrodes, b) the PCB that sends the control signal that moves each monitor in and out of the beam. The preamplifier is in the 3rd iteration of prototying, following requests from the CERN accelerator specialists to add more features and decrease the susceptibility to electromagnetic interference. The layout of the 3rd prototype is finished and we expect 10 sets to arrive in about 1

month. It will then be tested by CERN experts using the H^- beam. Afterwards a mass production of 90 preamplifier boards will be carried out using factory mass production techniques. The wiring of the ASICs to the PCB's will be carried out by the CERN EP division wire bonding lab.

In parallel to this, an induction decelerator is being developed at Max Planck, which we hope to deploy in $\sim$ 2022 for validation tests in Phase2b. We may first choose an intermediate beam energy $E = 85$ keV before further deceleration to $E = 50$ keV to improve the experimental precision.

Phase 3 that follows the LS3 shutdown envisages experiments carried out using eV-scale antiproton beams to improve the precision on the $\overline{p}He^+$ to $\leq 10^{-11}$, though this is subject to the learning experience in phases 2a and 2b using only the induction decelerator. The research programme involves gradual introduction of new equipment and technologies to improve the precision. This step-by-step approach is needed if we are to characterize the systematics of each instrument in sequence.

We are near the end of our present funding cycle and will apply for further grants next year to sustain our operations beyond 2021, provided that SPSC encourages this proposal. We do have a track record over the last 20 years in this respect, and the proponents are committed to continue this experiment for the next 10+ years.

Part III
CUSP experiment for $\overline{\mathrm{H}}$ spectroscopy

4 In-beam hyperfine spectroscopy of antihydrogen

In this section of the proposal, we will begin by describing the aims and methods of the antihydrogen hyperfine structure measurement. The present status of experimental activities will be briefly reviewed and future improvements will be discussed in the context of a road map towards the desired experimental results of a ppm measurement using the Rabi method during run 3 and a ppb measurement using a Ramsey type method during run 4.

4.1 Introduction

Antihydrogen ($\overline{\mathrm{H}}$) is the simplest stable antiatom and the only one which can be produced in the laboratory at low energies. Hence, it is an ideal target for the application of precise spectroscopic methods to determine the transition frequencies between states. The matter counterpart hydrogen is one of the most studied targets in the physical sciences, hence, its structure is extremely well known.

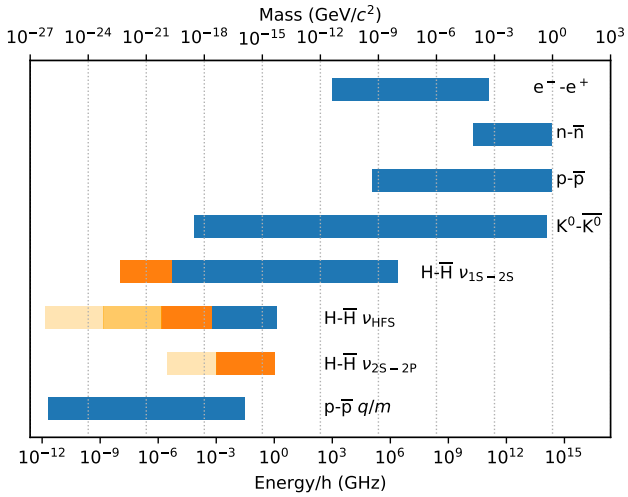

Figure 36 – Comparison of several tests of CPT symmetry on an energy scale. Bar's right hand side: measured quantity, length of bar: relative precision of CPT test, left hand side: sensitivity on an absolute energy scale. Blue: existing test. Orange: predicted sensitivity if existing precision for hydrogen is achieved. In the case of HFS: orange: first goal for in-beam measurement, paler orange: line width for fountain, yellow: hydrogen maser result. In case of Lamb shift: orange: estimated achievable accuracy, paler orange: accuracy for hydrogen. Values are from PDG [85] except for $\overline{\mathrm{H}}$ results for HFS [86], 1S–2S [87], and Lamb shift [88]. $\overline{\mathrm{p}}$ charge-to-mass ratio [24], note that the position is somewhat arbitrary since the cyclotron frequency is proportional to the magnetic field in which the measurement is taken; the length of the bar is very precise however. From [89].

The importance of measuring the hyperfine splitting of antihydrogen is demonstrated in figure 36. Here we compare available tests of CPT symmetry including comparisons of particle and

antiparticle masses, charge-to-mass ratios, and transitions in antihydrogen. A more elaborate comparison including e.g. g-factor measurements as performed by the BASE collaboration to ppb precision [90] is possible within the framework of the Standard Model Extension (SME) [91–93], which is the only model that allows for systematic comparison of different tests of CPT and Lorentz violation. Since the SME bases CPT violation on Lorentz Invariance violation, only transitions between different hyperfine states show first order effects in this model, making the 1S–2S transition less sensitive to testing the SME model [94]. Also the difference of two transitions used by ALPHA to determine the hyperfine splitting show no effect in the SME. The in-beam hyperfine experiments explained in the following thus offer for the first time direct sensitivity to SME coefficients with antihydrogen spectroscopy.

From figure 36, it becomes evident that atomic physics type measurements such spectroscopy of the internal structure of antihydrogen offer the most sensitive tests of CPT symmetry on an absolute scale. This motivates the investigation of the hyperfine splitting of ground-state antihydrogen, as this is the transition which is known to the highest absolute precision, namely to 2 mHz (corresponding to $\sim$8 atto-eV).

The potential of antihydrogen as a system for precision tests of CPT was realised 25 years ago [95], the most difficult challenge being the formation of cold antihydrogen atoms suitable for spectroscopy [96]. At the Antiproton Decelerator (AD) several experiments are now able to routinely produce antihydrogen [97], with the ALPHA collaboration having been able to perform first spectroscopic measurements [86, 87, 98].

Even if the results on antihydrogen are found to agree with those of hydrogen, they can be used to put limits on models and thereby advance our understanding of nature. The ASACUSA-Cusp experiment aims to produce a beam of antihydrogen which will undergo Rabi-type magnetic resonance spectroscopy to perform a precision measurement of the ground-state hyperfine structure [99]. Unlike other approaches [87], extraction of a beam allows for a measurement unperturbed by the high magnetic fields used for confinement, meaning that a higher precision can be achieved.

Rabi-type spectroscopy requires a spin-polarised beam. To form such a beam of antihydrogen, the mixing of positrons and antiprotons occurs within the special magnetic field configuration of the unique 'Cusp trap' [100]. This trap consists of 4 superconducting field coils arranged in a double anti-Helmholtz configuration and a multiringed electrode (MRE) trap housed within a cold bore surrounded by the magnet. Due to the unique magnetic field configuration low field seeking states should be preferentially focused along the beam axis whereas high field seeking states should be defocused - polarising the beam [101,102]. The polarised $\bar{\mathrm{H}}$ beam is then sent through the hyperfine structure spectrometer (as described in section IV).

At present, the collaboration has observed antihydrogen 2.7 m away from the production region [103] and measured the principal quantum number (n) distribution of the beam produced [104]. These measurements yielded a low beam intensity and showed that the principal quantum number distribution skews towards high n. Hence, it is clear that to succeed in the physics goal of the experiment, work must concentrate on increasing the beam intensity and lowering the n distribution.

5 Antihydrogen beam production

To achieve efficient antihydrogen formation, various strategies can be pursued to mix the charged plasmas of antiprotons and positrons as gently as possible. Independently of the underlying details of the mixing process, the formation on the level of individual particles may proceed via two channels, namely radiative recombination:

$$e^+ + \overline{p} \Rightarrow \overline{\mathrm{H}} + h\nu, \tag{15}$$

or three-body recombination:

$$e^+ + e^+ + \overline{p} \Rightarrow \overline{\mathrm{H}} + e^+. \tag{16}$$

At high positron densities and low temperatures the latter process will dominate over the first one by several orders of magnitude, therefore efficient antihydrogen formation relies strongly upon the preparation of the positron plasma.

5.1 Experimental setup for antihydrogen beam production and during LS2

The ASACSUA-Cusp experiment has been described in details elsewhere, we will briefly review the current setup here before discussing present results and ongoing work during the long shutdown (LS2) at CERN which is vital for our future goals. During LS2, a modified version of the existing experimental setup is being used (see figure 37). The modifications have been made to operate with matter instead of antimatter. The technique of using matter to characterise component parts

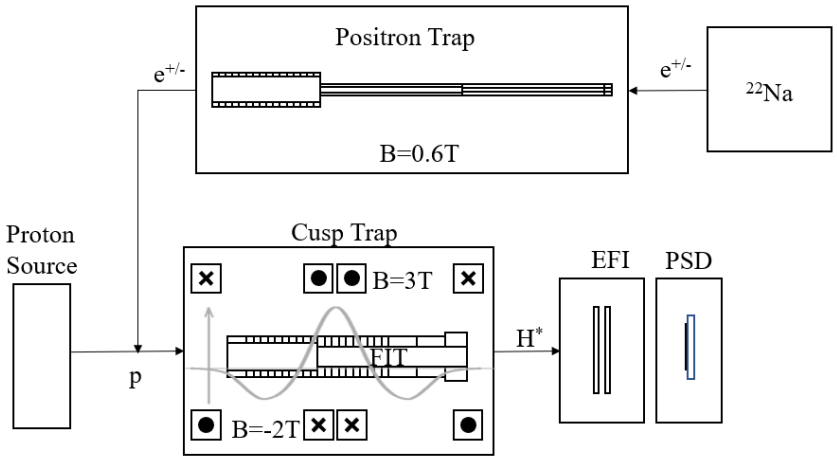

Figure 37 – A schematic diagram of the ASACUSA Cusp experimental setup as described in this proposal modified for matter.

of the ASACUSA-Cusp experiment has previously been very successful. The use of a hydrogen beam (see section IV) has allowed the microwave cavity and superconducting sextupole magnet to be fully characterised yielding the most precise in-beam measurement of the hyperfine structure of hydrogen [105].

A large part of this success is due to the availability of matter for continuous operation at high intensity. The shift to matter experiments during LS2 continues to enable operation of the complex multi-trap setup and only requires little intervention to the existing experimental setup, the required investments for proton production and hydrogen detection have been funded by the FWF in Austria who have also provided funding for a student and postdoc to work on the project. In contrast to antimatter experiments on beam production, the availability of matter will allow us to perform longer experiments achieving higher statistics and to employ methods that would not be possible or even *wasteful* with the precious supply of antimatter.

Previously this kind of matter experiment has not been possible, as the ASACUSA antiproton ($\overline{\mathrm{p}}$) beamline and experimental area are shared meaning the multi-trap setup had to be installed and dismantled on a yearly basis. This situation will change after LS2, with the AD is entering the era of the extremely low energy antiproton ring (ELENA) and the installation of a permanent fixed beamline for the Cusp experiment (see figure 1). Also, due to the shift in operations with ELENA,

we will be upgrading our entire control system to allow more automation and simpler operation. This process has already begun and will continue throughout LS2.

An overview of the multi-trap setup modified for the work with matter is shown in figure 37, however, most apparatus mentioned below can be easily identified. The only significant alteration from the typical antihydrogen experiment is the use of a position sensitive detector (DLD+MCP) to detect excited state hydrogen and protons downstream instead of the Hodoscope and BGO detector.

Positrons are produced by a ^{22}Na source from iThemba labs (SA) providing up to 2 GBq of activity. The decay to ^{22}Ne occurs with 90% probability as β^+-decay producing positrons of up to 546 keV, which are moderated using a solid Ne ice moderator. Approximately 0.25% of these fast positrons are converted into a usable slow beam of energy spread ($\Delta E \sim 1$ eV). The energy of the slow beam can be controlled by biasing the source, the slow beam is then magnetically guided into the positron trap.

The positron trap is housed within the cold bore of a superconducting magnet held at 0.6 T and kept at 100 K. It consists of a long gas cell and a multiringed electrode (MRE) trap which has a large number of narrow (width < diameter) electrodes allowing an extremely flexible potential shape to be produced. Positrons entering the trap must lose energy via inelastic collisions with molecular nitrogen allowing them to become confined within the longitudinal electrostatic potential. Once confined positrons eventually lose energy via collisions and cyclotron cooling, and become captured within a harmonic potential formed by the MRE trap before being ejected and transferred into the Cusp trap.

Multiple stacks of positrons can be stored within the Cusp trap. This combined with the use of a rotating wall electric field technique [106] which compresses the positrons allows for a dense plasma to be produced. To form antihydrogen, the positron plasma is stored in the Cusp trap (see figure 38) ready for mixing with antiprotons.

ASACUSA previously operated a unique radio frequency quadropole decelerator (RFQD) to further reduce the $\overline{\mathrm{p}}$ from 5.3 MeV energy to 115 keV. The RFQD has been removed ready for 100 keV beams from ELENA as it is no longer required. Although both the former RFQD and ELENA provide lower energy antiproton beams than the 5.3 MeV beam from the AD, the antiproton trap will still require a beam deceleration mechanism for an efficient catching. A simple solution is adopted in the form of degrading foils. The optimised tickness depends on the energy of the beam. Previously, the antiproton beam energy was adjusted by using the capability of beam energy tuning of the RFQD. The latest set of foils mounted on the MUSASHI trap are optimized for a 120 keV beam, in this case two 90 μgcm^{-2} biaxially oriented polyethylene terephtalate foils [107].

Since the ELENA beam has fixed kinetic energy of 100 keV, a thin foil with a more precise thickness is required. A commercially available Aluminium foil of 1.1 μm thickness with 10% tolerance is a candidate as the energy degrader. If this is not accurate enough, then it may be possible to float the foil to adjust the incoming beam energy. Our Monte-Carlo simulations indicate an 80% trappable fraction. In the simulation, we assumed the ELENA beam has designed momentum spread $\Delta p/p = 5 \times 10^{-4}$ and bunch length [108], and used experimentally obtained antiproton stopping powers measured by the ASACUSA collaboration [109].

In the case of the RFQD, approximately 10^6 antiprotons are trapped per AD cycle which are then sympathetically cooled and radially compressed using a rotating wall electric field to ambient temperature by electrons, which loose their energy via cyclotron radiation.

During for example, a typical direct injection mixing cycle typically 3×10^5 antiprotons are injected into the positron plasma with an energy just above its potential energy (see figure 38). As antihydrogen atoms are neutral they are not confined by the electric and magnetic, hence once they are produced they are free to move away from the formation region. Immediately downstream

of the mixing region an internal field ionisation trap (FIT) is prepared by applying large potential differences between adjacent ring electrodes. The resulting electric fields strip the positron from Rydberg antihydrogen ($n \gtrsim 27$) and store the antiprotons until they are dumped and detected via the annihilation signals in surrounding detectors. A vertex detector (AMT) is positioned around the vacuum tube inside the magnet bore to reconstruct the annihilation position of antiprotons inside the trap. It consists of two layers of Micromegas with 8 scintillator bars positioned between the layers. In addition, a segmented scintillation detector consisting of rectangular modules is placed externally on both sides of the Cusp trap in order to detect the charged particles that emerge from the antiproton annihilation (mainly pions) and monitor the annihilation rate and position during the different trap operations (extraction, cooling, mixing, and ejection).

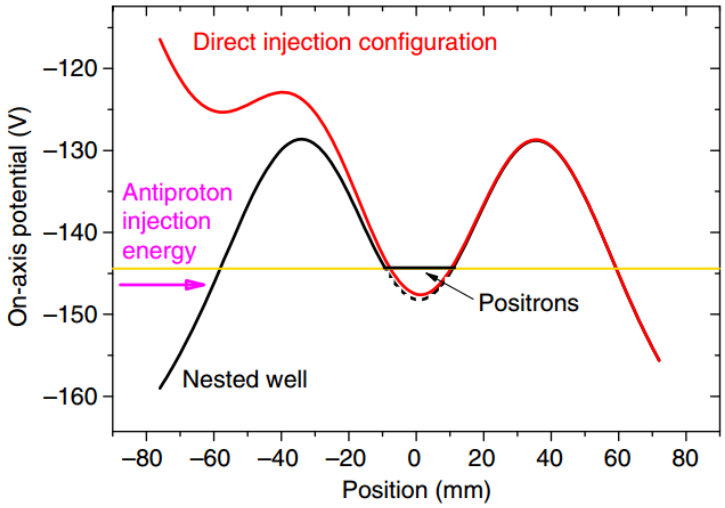

Figure 38 – Schematic diagram showing the direct injection scheme. [110].

Downstream of the Cusp trap a uniform strong electric field can be produced between two highly transparent meshes. This external field ioniser (EFI) is capable of stripping the positron from Rydberg $\overline{\mathrm{H}}$ down to $n = 12$.

At the end of the beamline, antihydrogen is detected by a bismuth germanium oxide (BGO) calorimeter which also acts as an annihilation plate for a charged pion tracker. The latter detector component is constructed as a two-layer hodoscope consisting of 32 scintillator bars for radial resolution and about 100 scintillating fibres for axial resolution per layer [111].

5.2 Current status of antihydrogen beam production

Figure 39a shows results from 2014 published in ref [103]. The distribution of the deposited energy on the BGO crystal located 2.7 m away from the formation region is compared for events detected during a mixing cycle (solid blue line) and those of background runs (shaded blue bars). In this case an electric field of ∼94 Vcm^{-1} was applied at the internal field ioniser trap (FIT) which will strip the positron from Rydberg antihydrogen with $n > 43$.

Taking 40 MeV as the threshold 99 events for $\overline{\mathrm{H}}$ ($n < 43$) were observed in 33 mixing cycles, using a higher field of ∼452 Vcm^{-1}, 29 events for $\overline{\mathrm{H}}$ ($n < 29$) were observed in 14 cycles compared with a background of 6 events in the equivalent time of about 10 cycles.

Figure 39b shows results for measurements of the principal quantum number distribution performed in 2016 from ref [112]. In this case the antihydrogen detector was placed directly after the

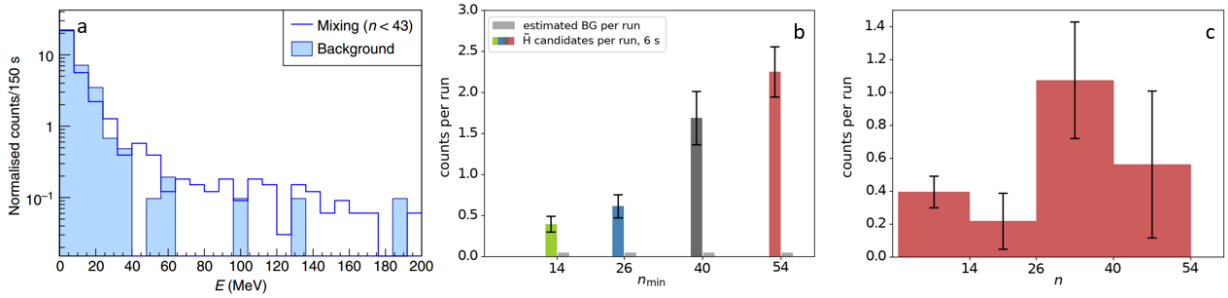

Figure 39 – **a.** figure 3a from ref [103] showing normalised coincidence counts during a mixing cycle compared with background 2.7m from the production region. **b.** Shows the cumulative n distribution of antihydrogen produced during mixing measured at the EFI. **c.** Shows the n distribution i.e. the difference between the cumulative values shown in **b** [112].

EFI to maximise the solid angle coverage. Analysis was performed using a machine learning technique (boosted decision trees), trained using antiproton annihilations on the BGO crystal which have the same event signature as antihydrogen annihilation. Results are shown normalised per mixing cycle. With the highest voltage on the field ionizer only $\overline{\text{H}}$ with $n < 14$ can reach the detector. Within 43 mixing cycles and with this setting, there were 7 $\overline{\text{H}}$ events identified, which assuming a velocity of 1000 ms^{-1} would be in the ground-state before reaching the microwave interaction region.

From these results it is clear that the direct injection method is not suitable for producing a beam of high enough intensity or low enough n state to be probed spectroscopically. Hence, in recent years work has moved towards so called potential merging schemes. Using this method, a positron plasma is at first accumulated in the Cusp trap. Antiprotons are then transferred from MUSASHI to the Cusp trap but not yet mixed with the positrons.

The particles then undergo a number of processes before mixing. Firstly the positrons are leveled (see figure 40**a**), this means the potential well where they are stored is partially opened allowing some to escape. This takes advantage of the space charge of the plasma ensuring that the same number of positrons is used during each experimental trial. Both the positrons and antiprotons undergo rotating wall compression and evaporative cooling (see figure 40**b** and 40**c**, compression takes place in potential i of 40**b**). The former uses a sinusoidally varying electric field applied on segmented electrode which reduces the radius of the plasma [106]. The latter involves slowly opening the potential well containing the plasma, allowing the hottest (those particles with highest kinetic energy) to escape before closing the potential. Finally the two particles are placed in shallow potentials next to one another and allowed to merge producing antihydrogen via three body recombination (see figure 40**d**).

This method was attempted during part of the 2017 and short 2018 beam time. Firstly, approximately 30 million positrons were injected and then 'leveled' off to 15 million. Approximately 300,000 antiprotons were then injected to the Cusp trap. After evaporative cooling of $\overline{\text{p}}$ roughly the same number of antiprotons remained in the trap, however the number of positrons after a similar evaporative cooling process was reduced to between 1 and 5 million (see figure 40 **b** and **c**). Although as many as 19,000 annihilation events were observed by the AMT scintilator [113] during mixing the number in the FIT was very low (almost 0). If these annihilation events are antihydrogen formation, this indicates a conversion efficiency of 6%. However, the fact that annihilation takes place on the walls before travelling towards the FIT indicates that the antihydrogen formed is emitted with a high radial velocity. This may be the case if the positron plasma density is too

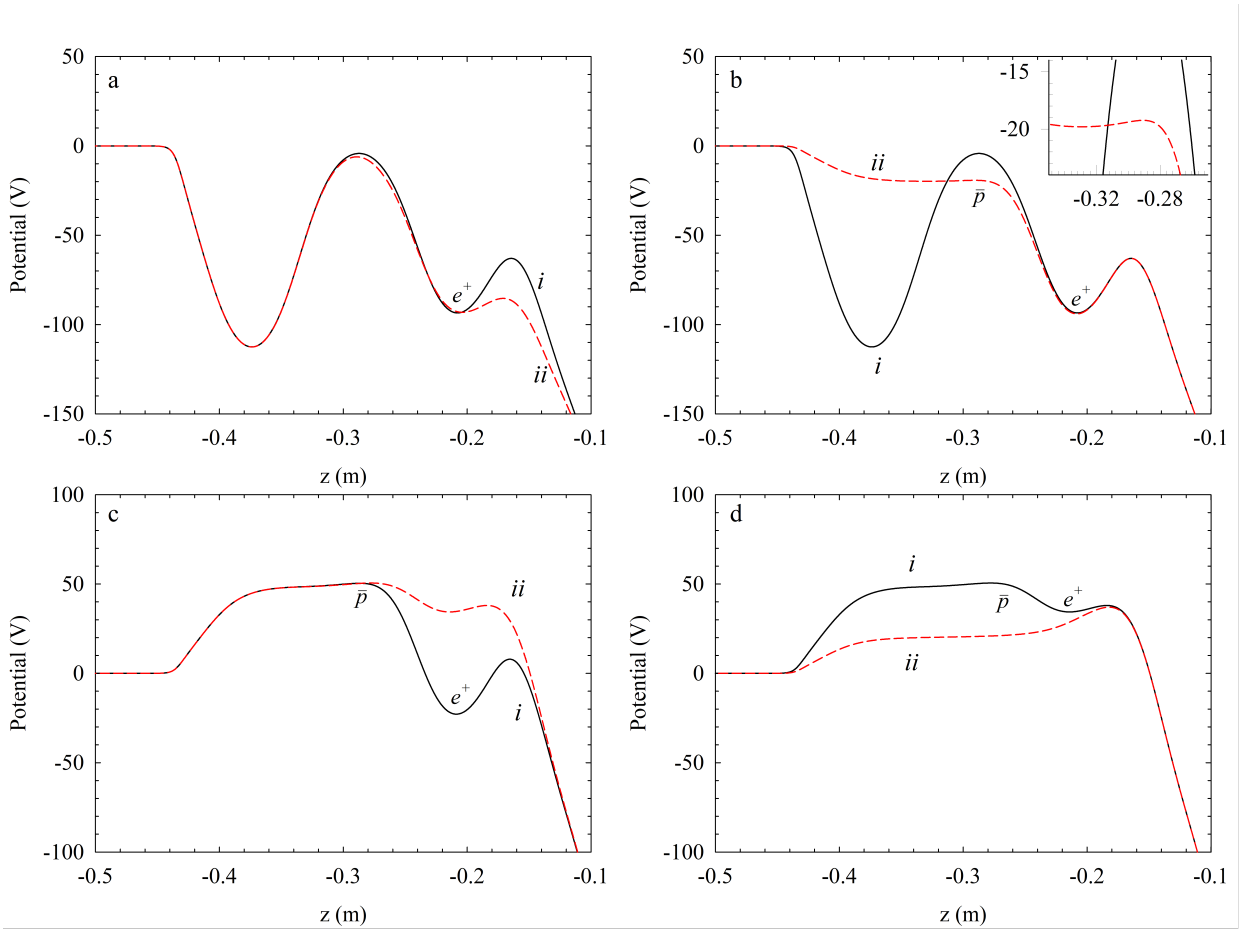

Figure 40 – Figures **a** to **d** show electrical potential shapes produced by the MRE in the Cusp trap. The black line is the starting potential denoted *i* and the red dashed line the finishing potential denoted *ii* in all cases. **a.** Positron leveling manipulation. **b** Antiproton evaporative cooling. **c** Positron evaporative cooling. **d** Antiproton – positron merging

high resulting in a large angular velocity which will in turn be imparted to the antihydrogen [114].

5.3 Planned improvements

From the review given in section 5.2, it's clear that improvements must be made to enhance beam production. In this section we will describe the direction for future experimental work towards this goal. Most of the work described here will take place during LS2 or shortly thereafter using matter or positrons. However, to avoid confusion we will continue to describe production of antihydrogen with positrons and antiprotons.

5.3.1 Cusp MRE trap and cold bore upgrade

As part of the work with matter funded by the FWF, a new MRE trap for the Cusp will be constructed. This new trap will consist of more narrower width electrodes with a smaller diameter in the mixing region (see figure 41 for a sketch of the concept). The use of narrower electrodes will allow for finer control over potential shapes and hence plasma manipulation. The reduced radius will improve the radial potential change over the width of the plasma column which should improve

the uniformity of plasma properties in the trap.

We also intend to improve the thermal properties to allow the electrodes to reach a lower temperature than the presently achievable (15 K). This upgrade is necessary to both update old hardware which can no longer be serviced and because by far the most important variable for efficient antihydrogen formation, is the positron plasma temperature [114, 115]. Without cold positrons any hope of forming an intense beam is lost. Hence, it is crucial that there are both methods to determine the plasma temperature and to reduce it in a reliable and reproducible way.

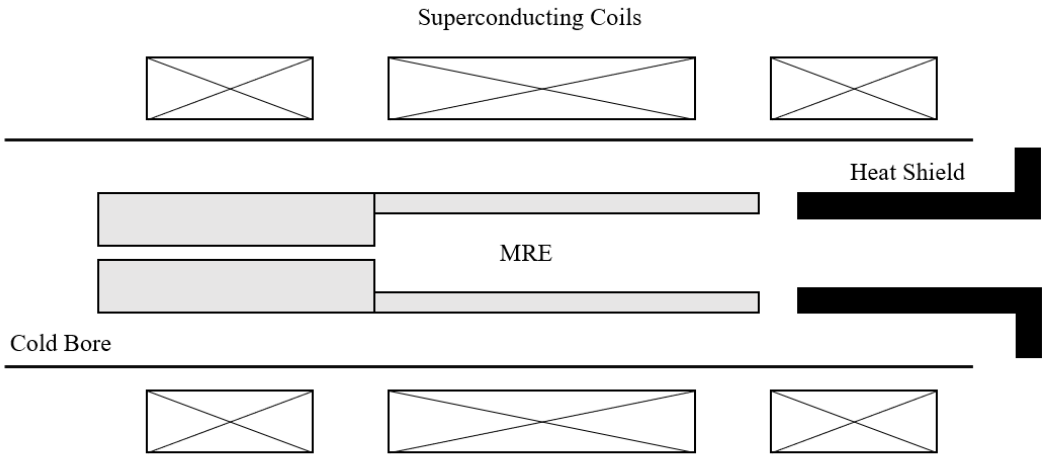

Figure 41 – An illustrative diagram of the new Cusp trap MRE stack concept.

5.3.2 Positron temperature measurement and control

Development of plasma temperature diagnostics has been underway since 2018 and is now maturing during LS2. The principle is simple, hold a plasma in a potential well and slowly lower the wall of the confining potential allowing the plasma to leak out (see figure 42). The current change with blocking voltage will be proportional to the plasma temperature if there are no perturbations to the plasma e.g. diclotron instability.

Positrons are slowly leaked from the potential well onto a detector consisting of a pair of microchannel plates (MCP) and a phosphor screen. This detector can be used to measure the radius of the cloud emerging from the trap by capturing an image of the phosphor screen using a CCD. However, in this case a signal is capacitively decoupled from the MCP back and the phosphor screen. These two signals are then fed into a differential amplifier which has the effect of removing the substantial electronic noise present within the AD hall and enhancing the signal.

Figure 43 shows an example of the positron current vs blocking voltage. By plotting the number of positrons ejected vs the potential drop, the first approximately 1% can be fitted linearly. The gradient (dN/dV) of the fit is then proportional to the temperature such that:

$$T = \left(\frac{dN}{dV} e k_B\right)^{-1} \tag{17}$$

Where, e is the electron charge and k_B is the Boltzmann constant. By applying the fit only to the first 1% of the signal it is expected that any plasma instability caused by depopulating the centre

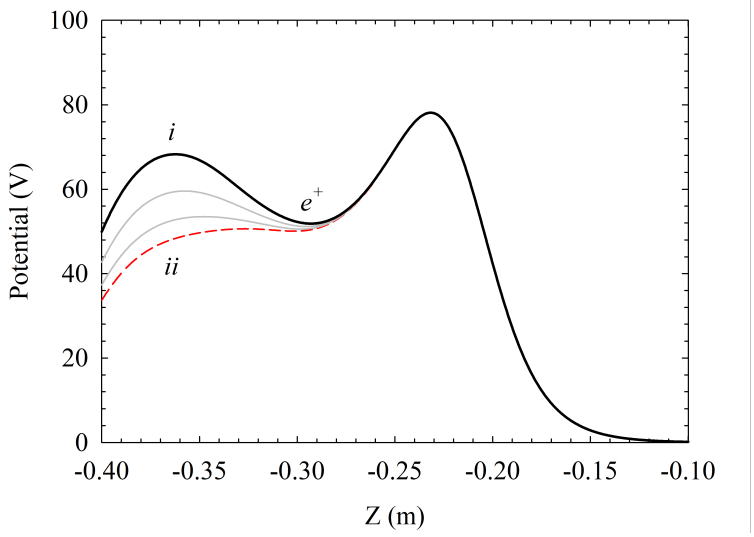

Figure 42 – Figures shows electrical potential shapes produced by the MRE in the Cusp trap. The black line is the starting potential denoted *i* and the red dashed line the open finishing potential denoted *ii*. Grey lines denote intermediate steps. Positrons escape from the well to the left hand side of the figure, the well is finally emptied with a slight potential gradient to count the total number of particles for each sample.

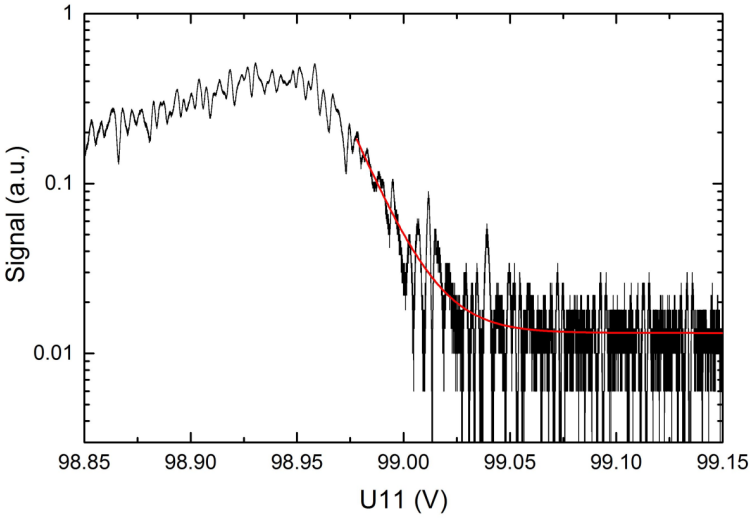

Figure 43 – Example of temperature measurement showing the change in current vs blocking voltage. In this trial experiment, positrons are transferred to the Cusp trap, compressed and then extracted onto the MCP, no cooling takes place.

of the plasma column is avoided. In this case, the plasma temperature was (116 ± 5) K.

The next step is control of temperature, the process of evaporative cooling (illustrated in figure 40**c**). Although this has been attempted previously, no quantitative measurements of temperature as a function of key potential manipulation parameters have been performed. This work is in progress at present. As can be seen in figure 44 a method to lower the positron plasma temperature is the key to increasing the antihydrogen yield.

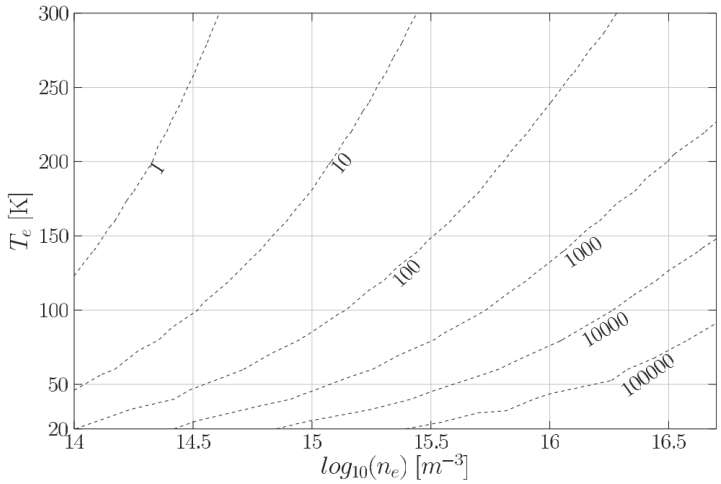

Figure 44 – Contour plot showing the production of ground state antihydrogen as a function of plasma temperature and density from [115].

In this figure the contour lines show the number of ground state antihydrogen atoms produced after a 10 μs pass through a positron plasma of given temperature and density. Given the present temperature measurement corresponds to 1 antihydrogen at 10^{14} m^{-3}. Reducing the temperature by 80 K would result in a 100 times increase in the number of antihydrogen atoms produced. We aim to cool the positron plasma to at least 20 K which would yield more than an order of magnitude increase in production rate according to figure 44.

However, the plot shown in figure 44 studies a regime ($> 10^{15}$m^{-3}) where at present we would need to consider many factors such as positron filling time, the rotation speed of the plasma (which would lead to $\bar{\mathrm{H}}$ being emitted radially, and the radial potential distributions.

To facilitate lower temperatures, the arrangment of the cold bore will be redesigned. This will involve replacing the present cryo-coolers with a larger capacity single cryo-cooler which is rated to 6 K with 3 Watts of cooling power. This allows a redesign of the downstream section of vacuum pipe where the path may be shortened, increasing the solid angle (albeit at the cost of flight time) and allowing options for optical access.

5.3.3 First Point Scientific positron trap and accumulation stage

A new positron trap will be installed in the ASACUSA area during LS2, this trap previously housed at the University of Aarhus was manufactured by First Point Scientific. It has a number of advantages over the existing system, not least it removes any need for regular liquid helium delivery for the ASACUSA Cusp experiment.

The design for the trap is very similar to the existing one (see figure 45), a ^{22}Na source provides fast positrons which are moderated by solid Ne in a 120 Gauss magnetic field. The moderation efficiency of the system is approximately 0.5% [116] which is a factor of 2 higher than the present moderator. This beam is magnetically guided into the trap which is a 2 stage design again similar to the existing system with a trapping efficiency of 35%. With a 1 GBq ^{22}Na source, a million positrons can be accumulated per second.

However, due to higher gas pressure in the storage stage, the lifetime in the Aarhus trap is much shorter than the present design (1.5 s as opposed to 38 s). Hence, a new accumulation stage will be constructed using the existing positron transfer line magnet which can provide a field of

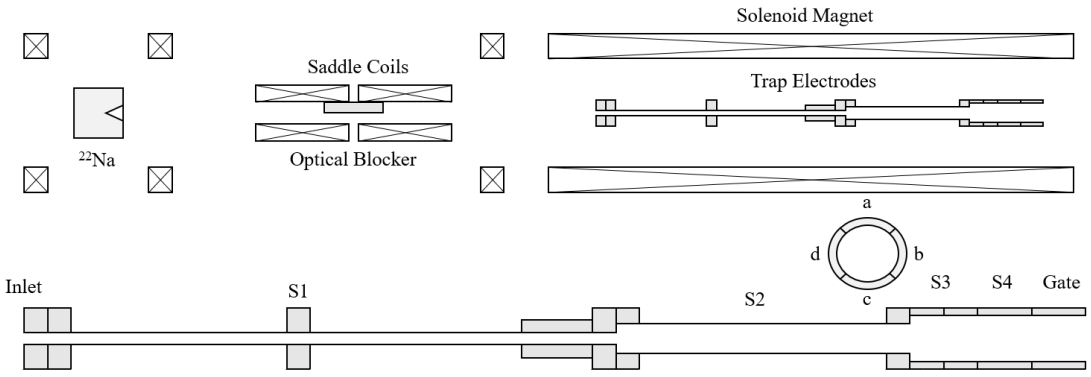

Figure 45 – Schematic diagram of the new positron trap showing **top:** magnetic field coil configuration and position of source and electrodes. **bottom:** detailed view of the trap electrodes including inset of electrode S3 which is split into 4 petals.

500 Gauss when water cooled. The trap will be a small MRE which can produce a harmonic potential for compressing and bunching the stored positrons before transferring to the Cusp trap. A small amount ($p \sim 1 \times 10^{-8}$) of sulphur hexafloride cooling gas will be admitted to cool the positrons during compression.

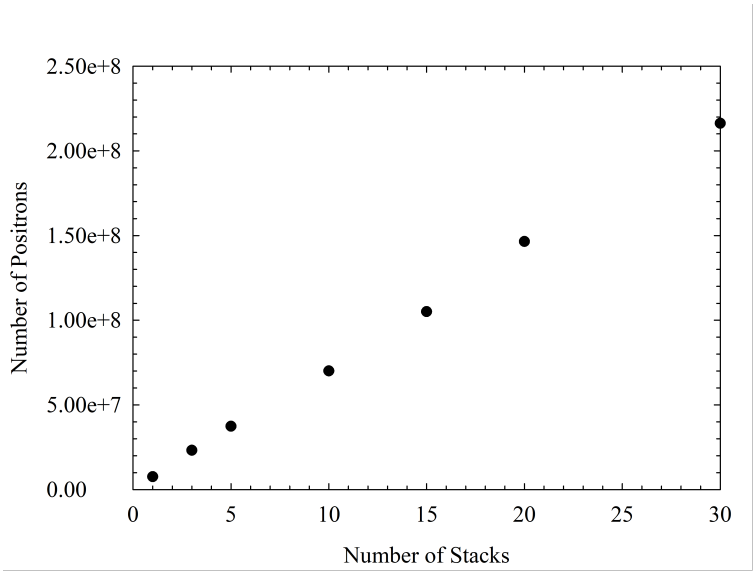

Figure 46 – Plot shows number of positrons stored in the cusp trap as a function of number of stacks.

One major advantage of this new system is the ability to collect a positron plasma in the accumulation stage allowing transfer to the Cusp trap in one shot. At present repeated stacking of shots (see figure 46) from the positron trap occurs allowing nitrogen gas to contaminate the Cusp trap electrodes each time a stack is transferred degrading the vacuum and hence the antiproton lifetime. Another huge advantage is that continuous positron accumulation can take place allowing for rapid refilling of the Cusp trap which will be essential to produce regular pulses of antihydrogen for spectroscopy.

5.3.4 Construction of an antiproton reservoir trap

As noted above, in the case of the new positron accumulator, to produce a regular pulsed beam of antihydrogen for spectroscopy it is essential to have both positrons and antiprotons available for mixing. Previously, in the case of antiprotons, before transferring to the Cusp trap the antiproton trap MUSASHI would catch 3 stack from the AD and condition them by electron cooling taking 6 minutes. Before this process could be initiated, positrons were stacked in the cusp taking between 3 and 10 minutes depending on source strength and number required. This is a slow process which takes time away from mixing experiments, hence it is planned to produce a new reservoir trap [117] for antiprotons between MUSASHI which will be used to catch pulses from ELENA and the Cusp trap where beam production will be performed. It is planned to finance this project by a standalone project application to the FWF in Austria. An illustrative drawing of a possible design for the new reservoir trap is shown in figure 47, a new MRE will be constructed following a similar design principle to the existing MUSASHI trap with smaller electrode radius for a better radial distribution. A harmonic potential can be created in the centre to manipulate the $\overline{\mathrm{p}}$. The previous single Cusp trap magnet will be operated in solenoid mode to provide a magnetic field of approximately 2.7 T. The entire apparatus will be kept at cryogenic temperatures less than 10 K in a heat shielded region. To cool the $\overline{\mathrm{p}}$ the conventional method of using collisions with electrons will be used.

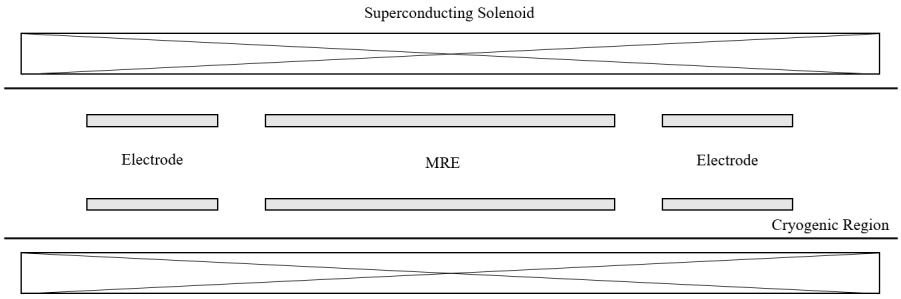

Figure 47 – Schematic diagram showing an approximate layout for the antiproton reservoir trap. Long cylindrical electrodes are indluded to make a well defined earth plane or a flat barrier for particles to pass over during slow extraction.

The trap arrangement is intended to be used in two ways, either a pulsed transfer as is used at present to move $\overline{\mathrm{p}}$ between MUSASHI and the Cusp or slow extraction of an antiproton beam (see e.g. [107]). The trap is designed to be symmetrical allowing extraction either upstream or downstream which opens up new possibilities for a parasitic slow extraction beam line mentioned elsewhere in this proposal (see section 9).

In terms of antihydrogen beam formation, the inclusion of this new trap opens a new possibility for a slow extraction mixing from the reservoir trap. The idea in theory is simple, to guide a $\overline{\mathrm{p}}$ beam into the Cusp trap with a well defined energy. To transport antiprotons adiabatically into the Cusp trap with energies of the order 5 meV above the positron plasma potential is extremely difficult. This will require custom optics to be produced to ensure that the antiprotons remain on centre and with an energy that is well defined compared to the potentials defined by the Cusp trap MRE. However, the prospect is very attractive given the very recent work of ref [114] which has suggested that for effective beam formation the $\overline{\mathrm{p}}$ must have some forward momentum when entering the positron plasma. In some way this aligns with the methods used for creating other neutral beams such as positronium via charge exchange with gases [118]. However, in this case the

gas is a cold positron plasma stored in the Cusp trap. In this beam neutralisation scheme, the antiprotons do not undergo multiple passes of the positron plasma. It may be possible to store them in the Cusp trap downstream of the mixing region and return them to the reservoir trap for reconditioning.

Another consideration for this method is that aside from the technically challenging work to transfer antiprotons from the reservoir with a very well defined beam energy is that the Cusp must contain and maintain the cold (20 K or less) positron plasma. One concern is RF noise heating the plasma e.g. picked up from the environment or during catching pulses in MUSASHI. The Cusp can be completely isolated electronically from the remainder of the multi-trap system, reducing electronic noise and hence possible heating effects on the positron plasma from RF. The successful observation of an antihydrogen beam 2.7 m from the production region was made using the direct injection process [103]. This involved colliding a pulse of antiprotons with an energy spread in the electronvolt range into the positron plasma (see section 5.2). It is expected that one of the main limiting factors of this method is the heating of positrons by the antiprotons which will occur very quickly via Coulomb collisions. In this direct injection model, a lower intensity beam of $\overline{\mathrm{p}}$ can be provided over a few 10s of seconds. By carefully tuning parameters such as beam energy relative to the positron plasma potential, number of antiprotons per cycle, and antiproton energy spread, an optimal slow extraction mixing cycle may be found.

5.4 Antihydrogen beam deexcitation schemes

Whilst the above discussion has focused on producing a higher beam intensity, another problem remains, that of the n-distribution from three body recombination. As shown in ref [115] this distribution skews towards high n as would be expected from basic conservation of energy arguments regarding the process. For successful hyperfine spectroscopy, a spin polarised beam of $n = 1$ antihydrogen is required. Atoms produced in $n > 1$ states which survive in the beam may contribute to the background observed by the antihydrogen detector.

During the flight between the production region and the microwave cavity, atoms will undergo spontaneous emission decaying towards the ground state. The length of time the atom has to cascade depends upon the velocity of the antihydrogen, which is primarily determined by the $\overline{\mathrm{p}}$ velocity when three body recombination occurs. Some states such as the metastable 2S or circular states ($|m| = n - 1$) can be very long lived and will not decay to the ground state even at very low kinetic temperature, these states will contribute to a background and not be useful for our measurement. There are two solutions to this problem, either remove the background if the ground-state beam is intense enough or increase the deexcitation rate.

5.4.1 Collisional deexcitation with a plasma

It may be possible to achieve both an increase in $n = 1$ and a filtering of high-n states using a plasma placed between the formation region of the Cusp trap and the cavity. Two possibilities exist for collisional deexcitation plasmas, either a long positron plasma in the formation region or an electron plasma placed downstream of the second cusp point of the magnetic field.

For a positron plasma, the collisions of interest are:

$$\text{3 Body Recombination: } \bar{p} + e^+ + e^+ \rightarrow \bar{H}^{**} + e^+ \tag{18}$$

$$\text{Collisional Deexcitation: } \bar{H}^{**} + e^+ \rightarrow \bar{H}^{*} + e^+ \tag{19}$$

$$\text{Collisional Excitation: } \bar{H}^{**} + e^+ \rightarrow \bar{H}^{***} + e^+ \tag{20}$$

$$\text{Ionization: } \bar{H}^{**} + e^+ \rightarrow \bar{p} + e^+ + e^+ \tag{21}$$

The first channel is collisional deexcitation, in this case a collision will enhance the number of ground state antihydrogen atoms which reach the cavity. This process appears in general to be important after the initial formation of antihydrogen whilst it is still in the positron plasma, a few collisions are required to 'stabilise' the atom before it can escape [114, 115]. The opposite process collisional excitation can also occur which would increase the number of atoms in excited states and thus increase the background. Ionization is a loss processes but occurs with a higher probability for very high n states. Three body recombination, is the inverse of ionisation and the process which initially creates the n-distribution and is shown for completeness.

The length of the positron plasma i.e. the effect of multiple collisions, has been investigated in ref [119]. It was found that for a 20 K plasma increasing the length from 0.7 cm to 35 cm produced an increase in the ground state fraction of 4 orders of magnitude, whereas a 300 K plasma over the same length range only showed 2 orders of magnitude increase. Although a dense 35 cm plasma would be impossible to produce in the present arrangement due to the cusped field configuration required to polarise the beam, a few cm positron plasma could be produced, especially for the mixing scheme described above where a slow antiproton beam originating from an upstream trap is neutralised.

In the case of an electron plasma downstream of the magnetic cusp points, we have to now consider electron collisions with antihydrogen, here we return to a situation analogous to positron collisions with atoms. In this discussion the channels of interest are:

$$\text{Collisional Deexcitation: } \bar{H}^{**} + e^- \rightarrow \bar{H}^{*} + e^- \tag{22}$$

$$\text{Collisional Excitation: } \bar{H}^{**} + e^- \rightarrow \bar{H}^{***} + e^- \tag{23}$$

$$\text{Positronium Formation: } \bar{H}^{**} + e^- \rightarrow \bar{p} + Ps^{**} \tag{24}$$

$$\text{Ionization: } \bar{H}^{**} + e^- \rightarrow \bar{p} + e^+ + e^- \tag{25}$$

The latter two processes positronium formation and ionization are loss processes but again, should occur with a higher probability for high n states filtering the distribution and reducing the background. Our simulations show that the rates for these ionization processes are typically lower than the deexcitation rate.

Figure 48 shows a distribution of n states calculated using the methods described in ref [115] as black circles. In this case, the simulation included states up to n=50 however more highly excited states will be produced but may not escape the plasma. In this simulation antiprotons interact with a 25 K, $\rho = 1 \times 10^{14}$ m^{-3} positron plasma inside a 2.0 T magnetic field. This distribution was then allowed to interact with an identical electron plasma for a further 10 μs, the resultant n-distribution is shown as red circles. In this case, new scattering rates for electrons on antihydrogen were calculated using CTMC simulation, the Ps formation rate was added to the ionization rate so we consider the 'total ionization rate' rather than individual 'direct ionization' and positronium formation, finally the three body recombination rate is set to 0. The white circles show the time evolution after 10 μs with no particle interaction. As can be seen from the figure, the interaction with the plasma begins to remove some of the high n states and enhances the cascade towards ground state.

Within the Cusp trap arrangement, an electron plasma can be placed downstream of the magnetic cusp, allowing storage of a stable plasma. The same techniques used to produce a cold positron plasma described above can be used to prepare a similar electron plasma which can be injected with a simple electron gun. This makes this dexcitation and filtering scheme simple in comparison to other more complex schemes involving stimulated emission described below. An additional benefit of this electron collision scheme in terms of the formation of a spin polarised

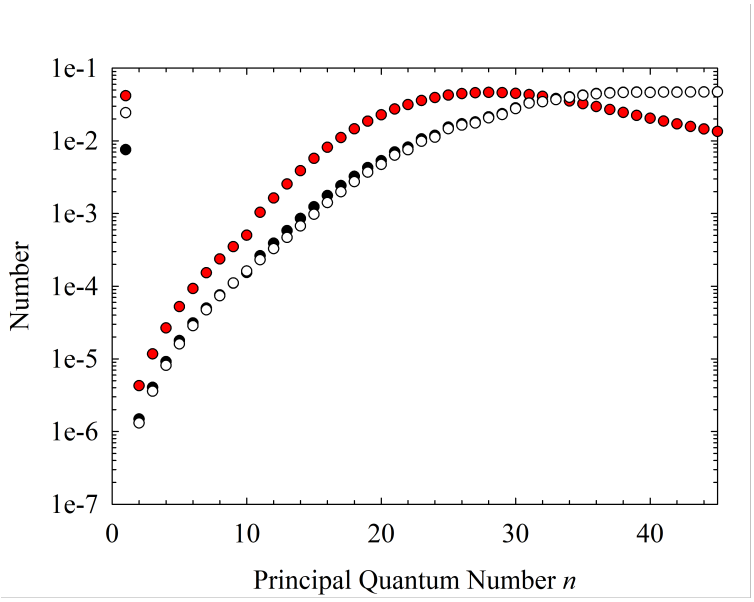

Figure 48 – Figure shows distributions of n states formed during a 10 μs pass through a positron plasma $\rho = 1 \times 10^{14}$ m^{-3}, T=25 K in B=2.0 T - black circles, this is the initial n distribution after mixing. The initial distribution after a 10 μs pass through a electron plasma with the same temperature and density as the positron plasma - red circles. The initial distribution after a 10 μs flight interacting with no particles - open circles.

beam is that an electron is unable to flip the spin of the atoms it interacts with due to the lack of the exchange interaction.

This scheme will be tested during LS2 and if effective will be applied during run 3 and run 4. In parallel, another deexcitation scheme is envisioned relying on light interaction allowing the atoms formed in high Rydberg states to reach near ground states in a few μs timescale after their formation which would provide a much improved flux of useful antihydrogen atoms to the cavity.

5.4.2 Stimulated deexcitation

As mentioned before, one of the main point to be addressed during LS2 is the production of ground-state atoms. Since three-body recombination produces high Rydberg states with a spontaneous lifetime of several milliseconds (translating to several meters of travel before reaching ground-state assuming an antihydrogen beam with a distribution of velocities corresponding to a temperature of 50 K), a stimulated deexcitation is needed to obtain ground-state atoms for measurements. An alternative to the collisional deexcitation described above is that of dedicated light stimulated deexcitation. This presents two advantages : that of bringing high n states (that collision would have potentially ionized) down to deeply-bound states and address the highest number of antihydrogen formed since, in principle, appropriate light can be brought at the point of formation. We have seen that it is important to bring atoms as soon as possible to ground-state after their formation because the yield and polarisation of the beam after the cusp is much improved and the background from excited state at the cavity is suppressed [120]. We should thus rather deexcite to ground-state rather than merely shift the initial broad distribution of states to lower states and solely rely on spontaneous decay between the production point and the cavity. Antihydrogen formation via three-body recombination is a long process (formation has been observed to last milliseconds) we therefore need a "continuous" deexcitation mechanism which is nevertheless

efficient in bringing atoms to ground-state within a few μs so that antihydrogen atoms do not travel more than a few cm before they reach ground-state.
For this purpose, different light-stimulated deexcitation mechanisms can be envisioned :

1. that of lowering the principal quantum number n by driving $\Delta n = -1$ transitions down to low n states that have faster spontaneous lifetimes. Those transitions are in the low to sub-THz region (for example $n = 30$ to $n' = 29$ is around 200 GHz while $n = 10$ to $n' = 9$ would be around 8 THz) and require a narrow-band source of multiple THz frequencies in order to efficiently bring the atoms to low n states.

2. that of bringing the most populated high angular momentum states with long lifetimes toward low angular momentum states which have fast spontaneous decay. For $n \sim 30$, the transitions are around 15 GHz and therefore require a broadband microwave source which can cover the spread of the manifold due to the diamagnetic term (a few GHz for high n).

A combination of those two mechanisms or coupling to a laser can also be envisioned. We have studied the different options [121] in a simulation. We diagonalized the full Hamiltonian for hydrogen in a 1 T magnetic field and obtained energy levels and transition dipoles between all possible states up to $n = 30$ (note that the final n state is only limited by the computational time and can be extended to higher Rydberg states).
Figure 49 shows the proportion of ground-state atoms as a function of time from an initial distribution in the $n = 30$ manifold (equipopulation in all substates) when illuminated with THz light at frequencies to drive all transitions from $n = 30$ to $n' = 5$. It shows that a total power of $\sim 100\,\mu\mathrm{W/mm^2}$ (in this case evenly distributed between the 25 needed transition frequencies) is sufficient to bring 80 % of the atoms in ground-state within 30 μs.
This amount of power injected into the cryogenic apparatus should not be harmful. A dedicated test will nevertheless be done in-situ during LS2 to determine any potential issue.
It should be noted that, in this process, all manifold with $n < 30$ will also be brought down, which will even increase the proportion of the initial broad distribution brought to ground-state.
This result can be slightly improved when adding microwave radiation which favours a good mixing in m. Even better results can be obtained by going to lower n' (the shorter the spontaneous lifetime of the n' state which provides the dissipative process to ground-state the better the result). However it is experimentally difficult to drive several $\Delta n = -1$ transitions at low n manifold (which corresponds to high THz frequencies).
We have evaluated several off-the-shelves options that will be tested experimentally during LS2 (see sec. 8.3).
Reaching low n' is however possible with a laser bringing population down to the $n' = 3$ or $n' = 2$ manifolds where the spontaneous lifetimes are only a few tens of ns. We have estimated the gain in coupling THz and RF mixing at high n with a continuous laser deexcitation from $n' = 20$ to $n'' = 3$ ($\lambda \sim 839$ nm). The results are illustrated in Fig. 50 for different laser powers. The evaluation of feasible laser powers and most optimal THz/RF/laser configurations will be provided in [121] and will be tested experimentally on a Rydberg hydrogen beam (see sec. 8.3). The result of these evaluation will be reported in the next report to the SPSC (January 2020).
The implementation of such light-induced deexcitation will require modifying the trap in order to allow for light access, something that is envisioned in the Cusp electrodes and cold bore redesign. One of the challenge will be bringing THz light as close as possible from the formation region for which solutions are being investigated.
Such light access will also enable possible experimental tests of a novel antihydrogen formation mechanism. Indeed, it was realized that coupling a laser stimulated recombination process as pro-

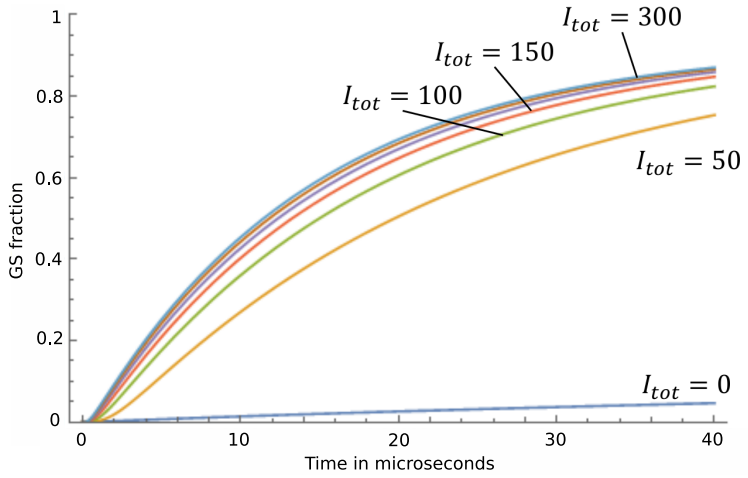

Figure 49 – Ground state fraction as a function of time. The population is initiated in the $n = 30$ manifold. We stimulate all $\Delta n = -1$ transitions down to $n' = 5$. Every $\Delta n = -1$ transition is driven with an intensity of $I_{tot}/25$. Units are in W/m^2.

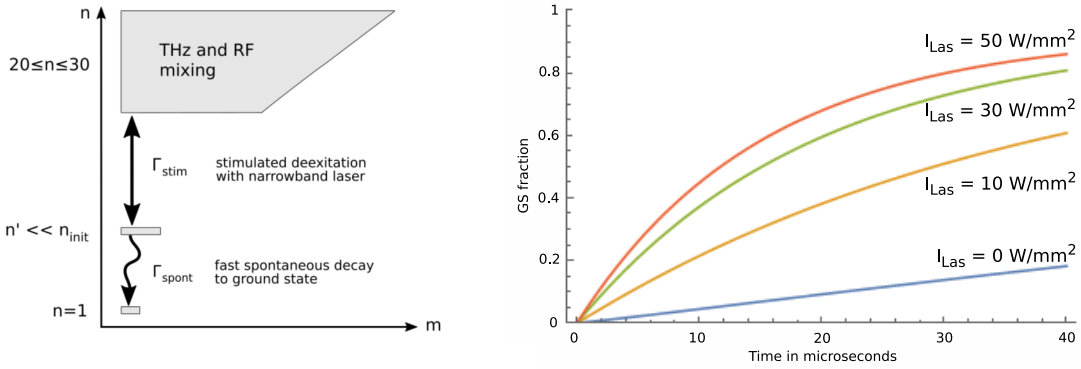

Figure 50 – right: sketch of a possible scheme to combine THz/MW and laser light to bring high Rydberg states to ground-state. left: Ground state fraction as a function of time. The population is initiated in the $n = 30$ manifold. THz light is used to mix the $n = 30$ down to $n' = 20$ manifolds (i. e. all manifolds in between are mixed). A laser couples transitions from $n' = 20$ to $n'' = 3$.

posed several years ago [122] (and experimentally tried with hydrogen and antihydrogen [123,124]) with a rapid deexcitation mechanism could significantly enhance the formation rate and bring it in competition to that of three-body recombination. The advantage of this formation mechanism is that it produces low n and low m states which are both advantageous for the rapid formation of ground-state antihydrogen. A comprehensive estimation of the prospects of this scheme is under study and will be reported in an upcoming publication [121] and further detailed in the next report to the SPSC (January 2020).

5.5 Detector Upgrades

5.5.1 Antihydrogen detector

The purpose of the antihydrogen detector at the end of the beamline is to count the arriving antihydrogen atoms. Since the detector only sees a small solid angle, the antihydrogen atoms

reaching the detector are few. Consequently, antihydrogen annihilations are very rare and the detector needs to be able to identify them efficiently in a background dominated environment. The background primarily consists of cosmic rays which have, depending on the trigger condition, rates of ∼0.5 Hz to 1.5 Hz. Another background contribution could come from annihilations of antiatoms in high-field seeking states that are defocused by the sextupole magnet and hit the wall of the beam pipe close to the detector. Those events would have a signature in the detector very similar to low-field seeking antihydrogen atoms reaching the detector. Therefore, a high detection efficiency and very good background suppression are essential.

The existing tracking detector is composed of two individual sub-detectors, (1) two layers of hodoscope made up of scintillating plastic bars parallel to the beam direction giving the tracking detector x and y-resolution, and (2) two additional layers (one for each bar layer) of scintillating fibers perpendicular to the beam providing position resolution in the z-direction. Technical drawings of the $z-y$ and $x-y$ plane of the detector system can be seen in figure 51.

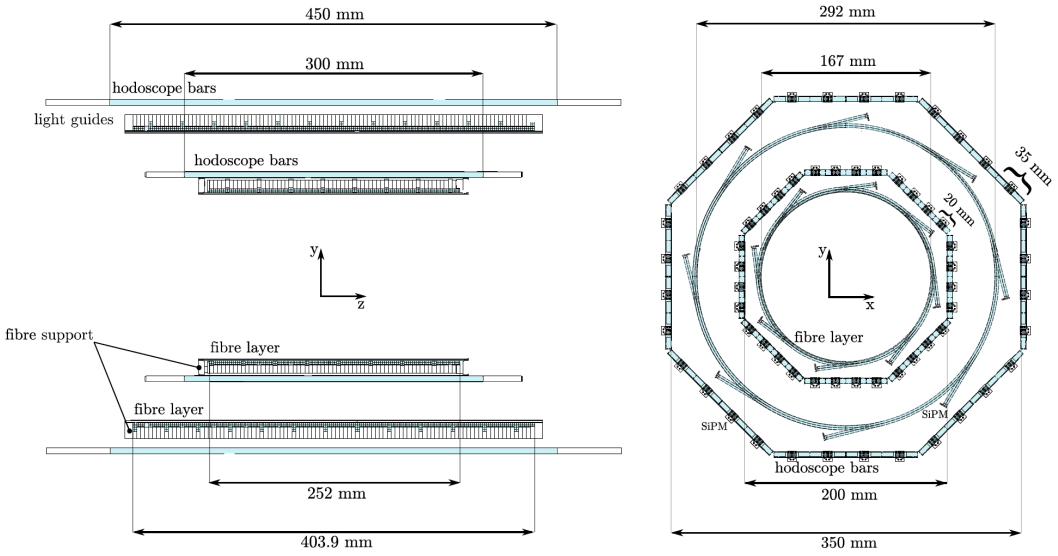

Figure 51 – $z-y$ (left) and $x-y$ (right) cross sections of the tracking detector

The performance of the detector, mainly the improvement of the z-resolution of bars and its impact on the vertex was studied carefully during the last two beam times in 2017 and 2018 (cf. fig. 53). It was shown that an unambiguous determination of the z-resolution will help to clearly discriminate between annihilation events coming from antiprotons stopping in the wall of the vacuum chamber and antihydrogen events annihilating in the central detector. A further improvement on the z-resolution could be achieved by increasing the time resolution (and therefore also of the z-resolution) of the hodoscope bars by removing the light guides of the bars and gluing the SiPMs directly on the scintillating bars, which is currently tested in the lab. An additional improvement will be to insert a layer of scintillating tiles around the inner hodoscope ring. Monte Carlo simulations are under way to determine the optimum design of this additional detector part. A sketch of the planned setup is shown in figure 52.

5.5.2 Scintillating bar detector

The scintillating bar detector placed along side the Cusp. Its purpose is to reveal the position and time of a $\overline{\mathrm{p}}$ annihilation occurring inside the Cusp trap. This is achieved by detecting the charged

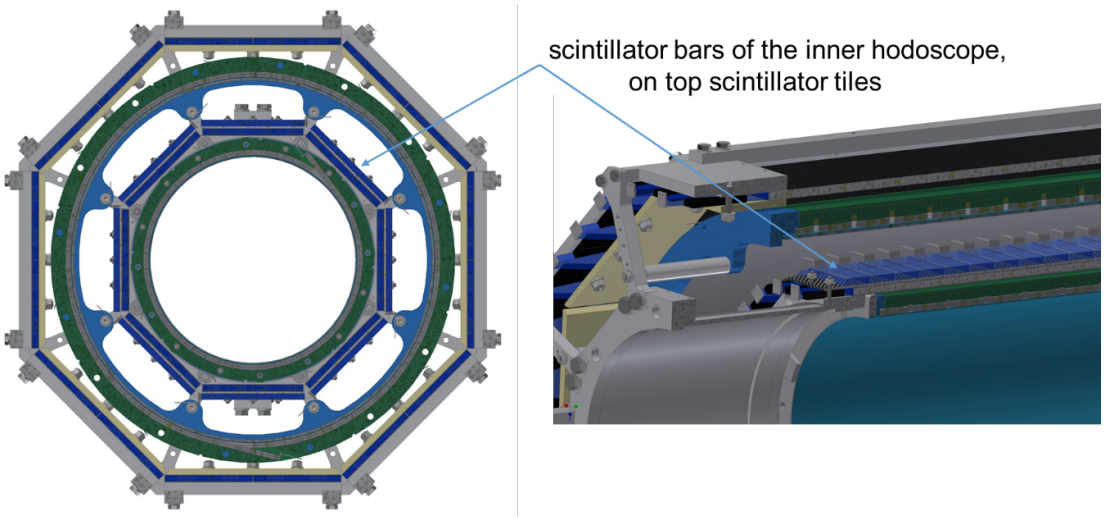

Figure 52 – $x-y$ cross section of the hodoscope with an additional layer of Si-tiles above the inner hodoscope bars (left); a detailed view of the Si-tile hodoscope bar structure (right).

pions originating in the annihilation process and reconstructing the vertex position and time.

The detector consists of scintillating planes with a sensitive area of 1 m^2 (larger version) or 0.5 m^2 (smaller version). The planes are composed of scintillating bars with length and section of 96 cm and 1.5×1.9 cm^2 respectively. A hole is drilled along their length to host a Y-11 type WLS fiber by Kuraray glued with E30 epoxy. The light from the WLS fibers of a single plane (maximum 62 channels) is collected by 2 Hamamatsu 64 channel H7546-B multianode PMTs. The electronics readout is performed by dedicated front-end boards (FEB) equipped with a MAROC3 ASIC. The FEBs host 2 FPGAs, a 12 bit ADC and present a dedicated socket to connect one single PMT. The MAROC3 chip processes the 64 analog signals from the PMT through a pre-amplifier with a variable gain and the signals are then delivered to a slow shaper and a sample and hold circuit. This analog output is then multiplexed with a clock speed of 5 MHz and digitized by the ADC locally on the board. The FEBs signals are handled by a VME buffer based set of electronics boards run by data acquisition program (DAQ), which is designed to operate the electronics both in auto-trigger mode (using a desired combination of the on-board discriminated signals) and with an external trigger.

The planes are placed close to the Cusp trap covering a total solid angle fraction from the center of the trap of ∼11% (8.5% one side and 2.5% on the other side). Since its geometrical acceptance covers a large area of the Cusp trap, the detector is complementary to the AMT detector which is more accurate but covers a narrower spatial region of the Cusp trap. The maximum DAQ acquisition rate is ∼1 kHz and the expected resolution for the z coordinate is around 2–4 cm.

Two possible improvement of the detector are foreseen replacing PMTs with Silicon PhotoMultipliers (SiPM) and upgrading the existing FEB (Front End Boards) to a full digital readout.

SiPMs are widely used in detectors for many physics fields. They do not require high voltages, they are small, magnetic field tolerant and can detect small amounts of light. The upgrade would consist of replacing the current light readout system (many fibers glued facing a multianode PMT) with a 1-to-1 fiber to SiPM scheme. With such an upgrade, each WLS fiber carrying the light out of the scintillators will be cut, re-polished and re-coupled to its SiPM improving the light collection efficiency and uniformity which are among the major causes of performance loss of the detector after several years of data taking and movement. The compactness of the system would also positively

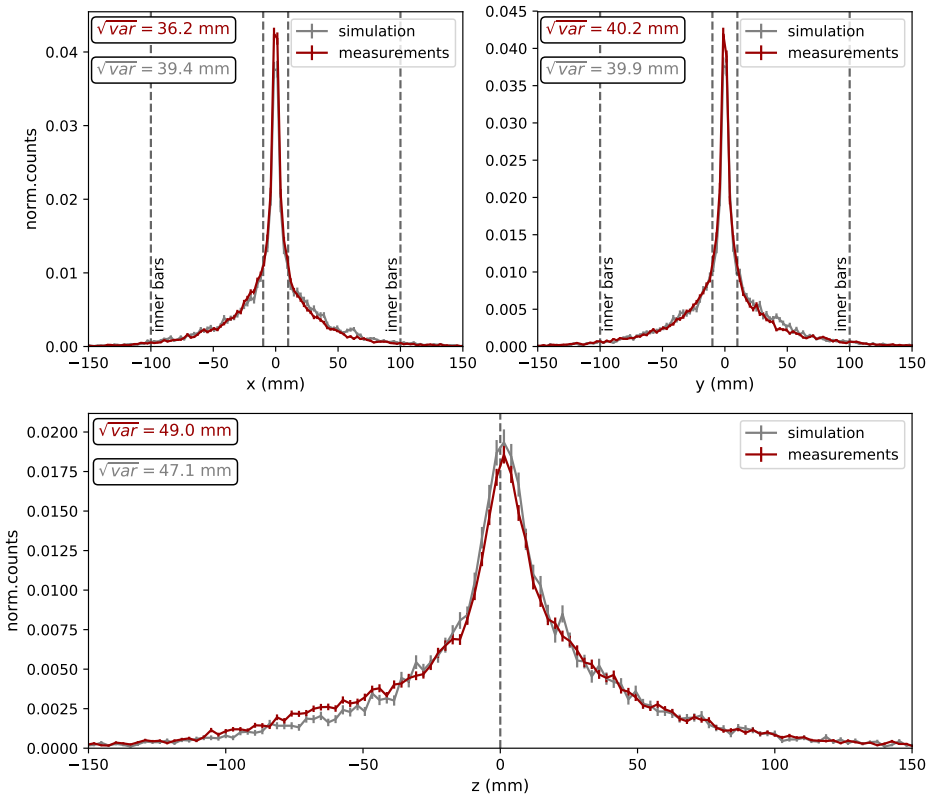

Figure 53 – Normalised distributions of the x (top left), y (top right) and z (bottom) vertex coordinates for measured data (red) and simulations (grey). The dashed lines mark the limits of the carbon foil and the Hodoscope inner scintillation layer [112].

affect the overall mechanical structure of the planes (less room for the fiber curvature and grouping would be necessary, which would mean smaller global dimension of the plane structure). The SiPMs signals would be handled by the present FEBs. A possible drawback comes from SiPMs intrinsic high dark count rate and their gain temperature dependence. Tests will be performed before the end of the year to validate the upgrade convenience.

The current DAQ scheme in the FEBs presents some limitations, e.g. a maximum DAQ rate of around 1 kHz is achievable. In certain conditions, sudden annihilation rates have been recorded thus saturating the scintillating detector DAQ for brief moments. Higher DAQ rates would be accessible by exploiting a full digital readout of the analog signals, a feature which is in principle already present in the MAROC3 ASIC hosted on the FEBs. The analog signals can be discriminated at a ∼MHz frequency with a time-over-threshold technique to measure the signal amplitude thus allowing a theoretical maximum DAQ rate a couple of orders of magnitude larger than the present one. The upgrade would also be cost effective because it just requires a new adapter card to be designed and added to the current DAQ chain.

6 Goals for run 3 and run 4

The physics goal of the ASACUSA-Cusp experiment is to perform spectroscopy of the hyperfine structure of antihydrogen. The existing Rabi type spectroscopy apparatus has been tested with a spin polarised hydrogen beam and produced the highest precision beam spectroscopy result for that target [105]. Hence, the work described above is designed to give a detailed road map towards producing a beam of spin polarised ground state antihydrogen which is intense enough to perform spectroscopy measurements in runs 3 and 4.

Most of the hardware upgrades and experimental testing will be performed during LS2 using matter and positrons. The availability of matter for testing enables continuous upgrading and experiments when antiprotons are not available in LS2 and beyond. After successful $\bar{H}$ spectroscopy, an intriguing possibility is using the same techniques with matter during LS3 within the same apparatus. The difficulty in this case is of course, observing a very low intensity beam of ground state H. However, this will be the most direct comparison of matter and antimatter spectroscopy possible.

Beyond LS3 and into run 4 we will upgrade our spectroscopy apparatus from a Rabi method to a Ramsey method. This will be described in detail elsewhere, as this apparatus is at present under development as part of the ASACUSA hydrogen beam program (see section IV). Using this method we expect to increase precision of the measurement from 1 part per million to 10 part per billion.

LS 2	**Matter Experiments**	Test mixing schemes with protons and electrons
	Hardware Upgrades	New positron trap and accumulator, new Cusp MRE, reservior trap development
Run 3	**Beam on/off observation**	First observation of interaction of beam with microwaves, resovior trap install
	Rabi Spectroscopy	Perform spectroscopy to 1 ppm or better
LS 3	**Matter Experiments**	Testing apparatus and if detection is possible spectroscopy to investigate systematic effects
	Install Ramsey Apparatus	
Run 4	**Ramsey Spectroscopy**	Perform spectroscopy to 10 ppb

The largest external changes to the experimental apparatus will be the removal of the Oxford super conducing magnet used for the present positron trap which at present requires 1000 litres of liquid He a week, and it's replacement with the smaller First Point Scientific style positron trap. The existing MUSASHI trap will become an antiproton catching trap and a new reservoir trap will be installed in the previous single Cusp magnet operated in solenoid mode allowing pulsed and slow extraction up or down stream. It is expected that during LS2 the control room will be moved from inside the AD hall to building 93, to facilitate this there will be a major upgrade of the trap control system.

Part IV
Experiments with a polarized hydrogen beam

In this part we describe ASACUSA's hydrogen beam experiments. The setup is operated at CERN in support of our $\overline{\mathrm{H}}$ program since the end of 2013. ASACUSA benefits in multiple ways from the parallel matter experiments. The main purpose of the hydrogen beam is in-depth characterisation of the $\overline{\mathrm{H}}$ hyperfine spectroscopy equipment and methods. Due to much lower availability of antimatter it would be impractical and wasteful to apply the $\overline{\mathrm{H}}$ beam for such tasks. In addition, hydrogen experiments with equipment built for $\overline{\mathrm{H}}$ are the most direct way to exclude or find systematic shifts, which might mimic a CPT violation. Finally, matter experiments carried out at high precision and/or over longer acquisition periods can put constraints on certain subsets of coefficients of the Standard Model Extension (SME) and thus explore CPT and Lorentz violation partly without a comparison to antimatter.

7 Status of ASACUSA's hydrogen beam experiments

In this section we briefly describe the hydrogen beam setup and summarise the status and achievements of the experiments. As we have obtained hyperfine spectroscopy results with hydrogen we use this section also to revisit the properties of the hydrogen (and $\overline{\mathrm{H}}$) hyperfine structure and the principles of Rabi spectroscopy first.

7.1 The hyperfine structure and Rabi spectroscopy

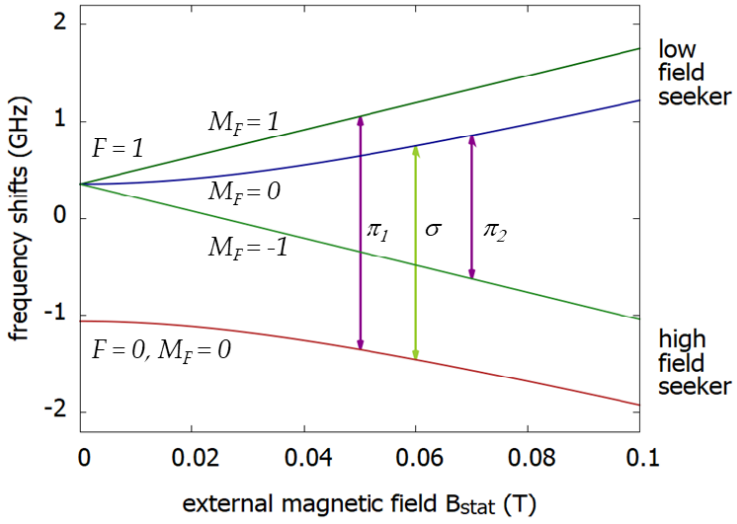

Figure 54 – Breit-Rabi diagram for hydrogen.

The properties of the hydrogen/$\overline{\mathrm{H}}$ hyperfine structure are comprehensively summarized in the Breit-Rabi diagram (see fig. 54 for the case of hydrogen; for $\overline{\mathrm{H}}$ the labelling of the states with $M_F = +1, -1$ would be interchanged). It shows the hyperfine energy levels of ground-state hydrogen as a function of an external magnetic field B_{stat} and their separation into a lower lying singlet state ($F = 0$) and an excited triplet state ($F = 1$). The Zeeman shift of two states of the triplet

($M_F = 0, 1$) increases the energy level at higher magnetic fields, making them to low field seekers, i.e. they feel a force towards lower magnetic field when exposed to a field gradient. The remaining triplet state ($M_F = -1$) and the singlet state are high field seekers. The two states with magnetic quantum number equal to zero ($M_F = 0$) have a hyperbolic, i.e. only a second order, dependence on B_{stat}. The other two states have a linear dependence. The transition between the two states with $M_F = 0$ is called σ transition and features the weakest magnetic field sensitivity. The π transitions include one of the states with linear Zeeman shifts and are much more sensitive to magnetic fields.

Conventional Rabi spectroscopy requires the following ingredients: (i) a polarised beam produced by traversing a region with a strong magnetic field gradient - (ii) an interaction region, where oscillating magnetic fields B_{osc} induce transitions between the states - (iii) a second region of strong magnetic field gradients to analyze the changed state populations - (iv) a detector (the sections are identified in fig. 55). The application of this method to a beam of $\overline{\text{H}}$ is straight forward. Higher detection efficiencies are possible for $\overline{\text{H}}$ due to the distinct annihilation signals. However, this can not compensate for the tremendously lower yield when working with antimatter as opposed to matter experiments. Therefore the $\overline{\text{H}}$ hyperfine spectroscopy beamline requires a much larger acceptance (i.e. open diameter). Consequently the oscillating magnetic field is provided by a cavity and the analyzing magnetic field gradient by a superconducting sextupole magnet having an open diameter of 100 mm each.

7.2 The hydrogen beam setup

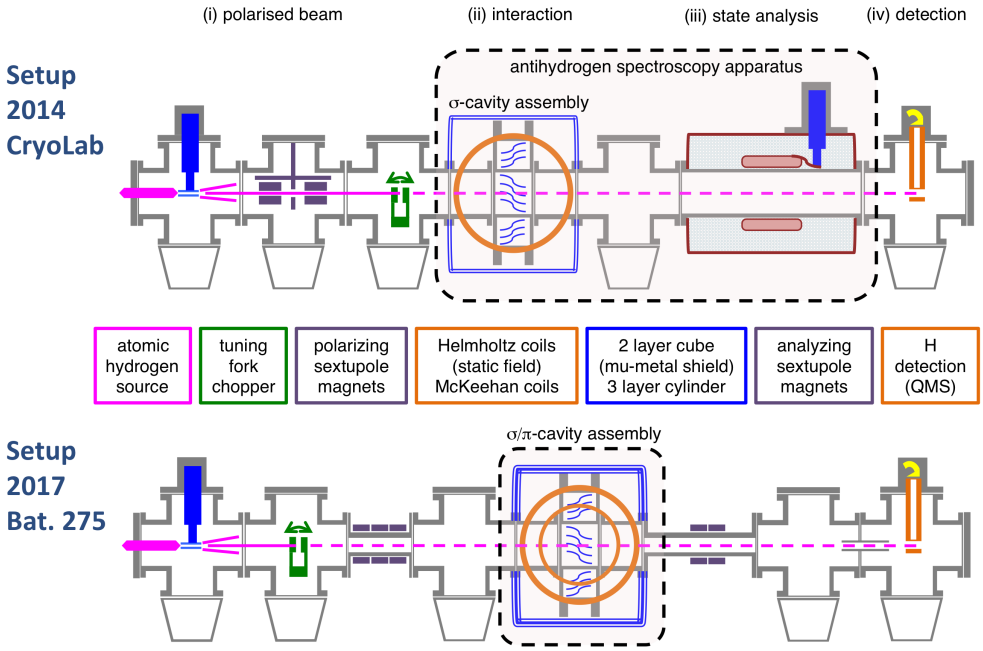

Figure 55 – Sketch comparing the hydrogen beam setups as installed at the CryoLab and bat. 275.

A source of cold, modulated, and polarized atomic hydrogen and a detector system have been brought from Vienna. At CERN a spin-flip cavity and an analysis sextupole magnet have been inserted between the source and detector, completing the Rabi experiment. Figure 55 shows a sketch of the main components of the hydrogen beam setup and compares two arrangements, which have been used so far.

The cavity of strip-line geometry [125] for providing microwaves at 1.42 GHz to induce hyperfine transitions and the superconducting sextupole magnet for spin-state analysis are the main components of ASACUSA's purpose-built hyperfine spectrometer beamline for $\overline{\mathrm{H}}$ experiment. Detailed technical descriptions are available in Ref. [126].

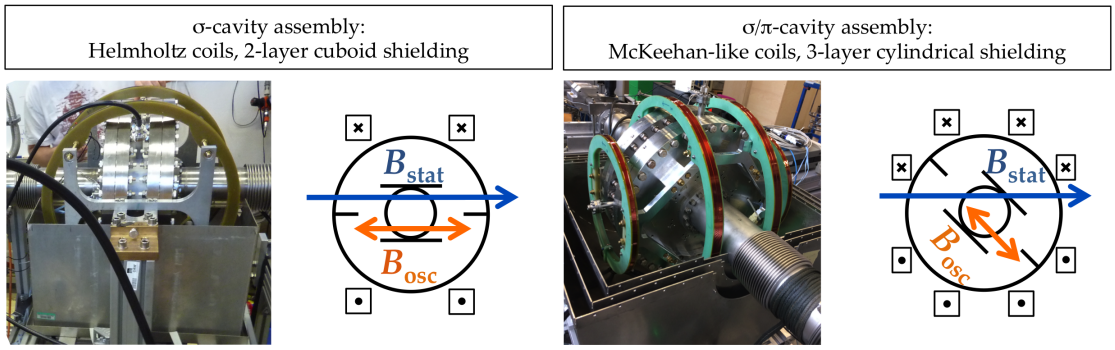

Figure 56 – Left: photograph and sketch of the σ-cavity assembly using Helmholtz coils and a two-layer cuboid magnetic shielding to provide B_{stat} in parallel alignment to B_{osc}. Right: photograph and sketch of the σ/π-cavity assembly using McKeehan-like coils and a three-layer cylindrical magnetic shielding to provide B_{stat} at an angle of 45° with respect to B_{osc}.

Two cavity assemblies are available (compare fig. 56) referenced as σ-cavity and σ/π-cavity assembly. The first one uses Helmholtz coils, which provide the static magnetic field B_{stat} in parallel alignment to the magnetic component of the microwave field B_{osc} and at a homogeneity of better than 1% (defined as standard deviation over mean value). This device is suited to investigate the σ transition ($F, M_F : 1, 0 \rightarrow 0, 0$). The in-depth characterisation of this cavity assembly and the superconducting sextupole magnet lead to the results published in Ref. [105], where the most precise in-beam measurement of the hydrogen hyperfine structure has been reported (relative precision of 2.7 ppb). Later a second cavity has been equipped with McKeehan-like coils to provide a more homogeneous static field (0.05%) at an angle of 45° w.r.t. to B_{osc}. This apparatus gives access to both the σ and π_1 ($F, M_F : 1, 1 \rightarrow 0, 0$) transitions. A journal publication on the results is in preparation, but they can already be found in two master theses [127, 128]. The characterisation of the σ/π-cavity assembly is basically complete and it can be employed for measurements on $\overline{\mathrm{H}}$ as soon as a beam of sufficient intensity becomes available. During LS2, however, it is sensible to continue with further systematic studies and long-term measurements.

7.3 Brief summary on achievements to date

The initial setup incorporating the σ-cavity assembly is described in Ref. [126] and the most important results are published in Ref. [105], which are:

- Determination of the hydrogen hyperfine structure with a relative precision of 2.7 ppb presenting the best result for this quantity achieved by using in-beam spectroscopy.
- Observed lineshape (apparatus profile) is well understood including effects caused by measurement properties like beam velocity distribution and microwave power $P_{\mathrm{MW}} \propto B_{\mathrm{osc}}^2$ (compare fig. 57 and fig. 58).
- On the present level of precision no systematic shifts where found, which might mimic a CPT violation. Therefore first result on $\overline{\mathrm{H}}$ will not suffer from systematic effects (NB: first stage precision goal is better than 1 ppm).

- The σ-cavity assembly and the superconducting sextupole magnet for spin-state analysis are characterized in depth and on stand-by in the AD-hall to be used in experiments with an $\overline{\text{H}}$-beam as soon as sufficient intensity is reached.

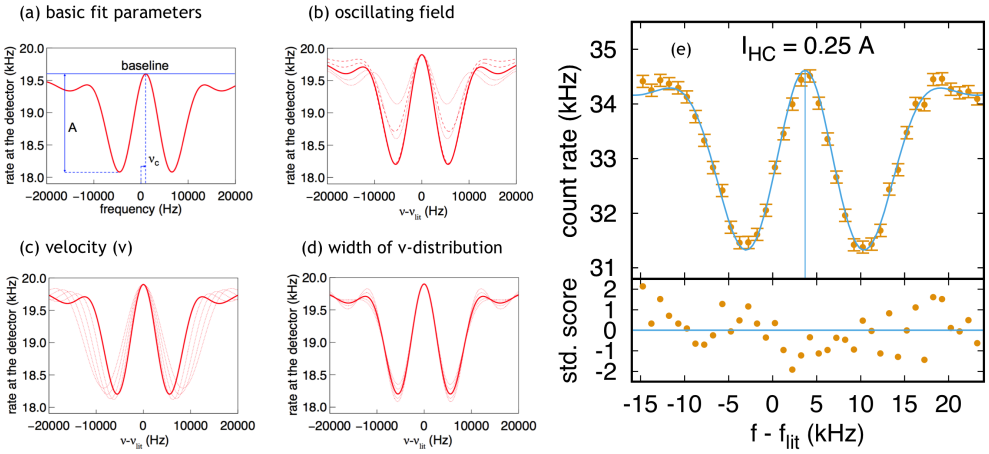

Figure 57 – Lineshape with double-dip structure as observed in Rabi-experiments with the oscillating magnetic field geometry of a strip-line cavity: Illustration of the influence of individual parameters and an example of data with a fit. (a) basic parameters are the central frequency, baseline and depth of the dips, (b) strength of B_{osc}, (c) mean velocity of the beam, (d) width of the velocity-distribution, (e) a single measurement at a certain value of B_{stat} and the fit with residuals shown below as standard scores.

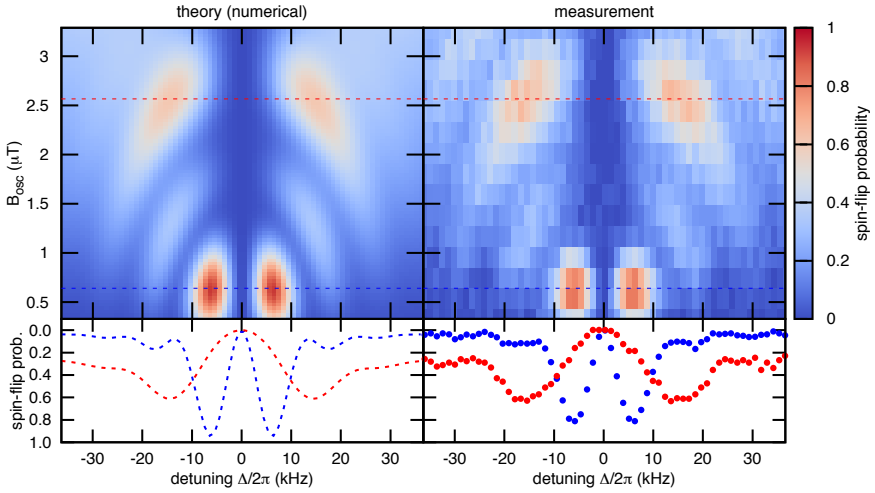

Figure 58 – Intensity plots showing the state-conversion probability as a function of the detune and B_{osc} as applied by the cavity. Left: theoretical calculation including the effect of a beam with a finite velocity spread. Right: measurement.

The measurements using the σ-cavity assembly have been conducted at the CryoLab of CERN as a helium recuperation line was needed for the operation of the superconducting sextupole magnet. A photograph of the setup is shown in fig. 59.

The superconducting sextupole was replaced by an analysing sextupole of much smaller acceptance (i.e. open diameter) based on permanent magnets, which is possible for experiments with a

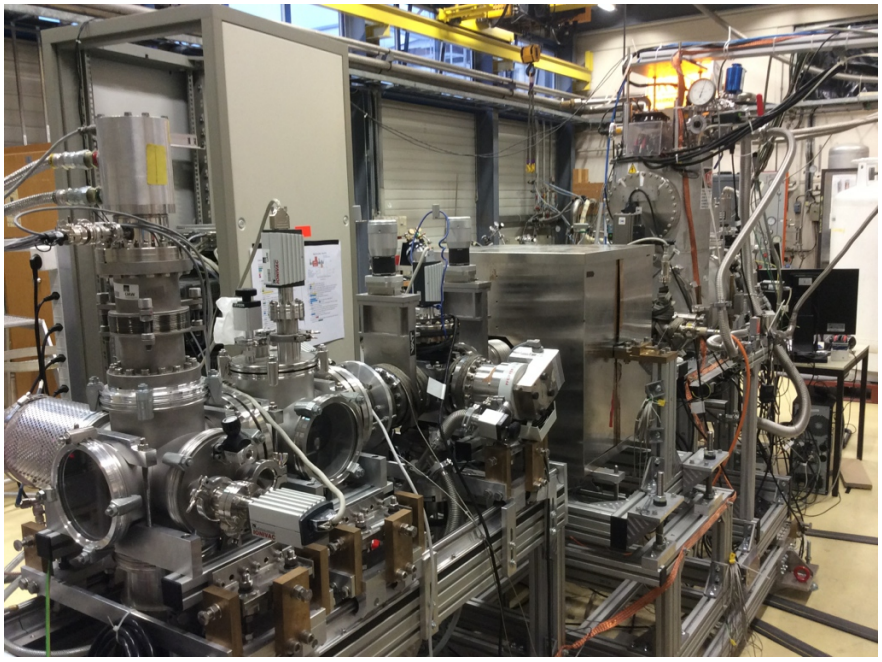

Figure 59 – Hydrogen beam experiment for measurements on the σ transition at the CryoLab.

hydrogen beam of small diameter. The setup has been moved to bat. 275 (compare fig. 60), where tests with the σ/π-cavity assembly have been performed:

- Those tests are complete, apart from investigations of beam-trajectory variations in the cavity.
- Similar level of statistical uncertainty has been reached as for the σ-cavity assembly.
- Systematic effects due to resonance interference at extremely low B_{stat} were observed.
- Correction methods for the systematic shifts have been investigated and further refinements are currently debated.

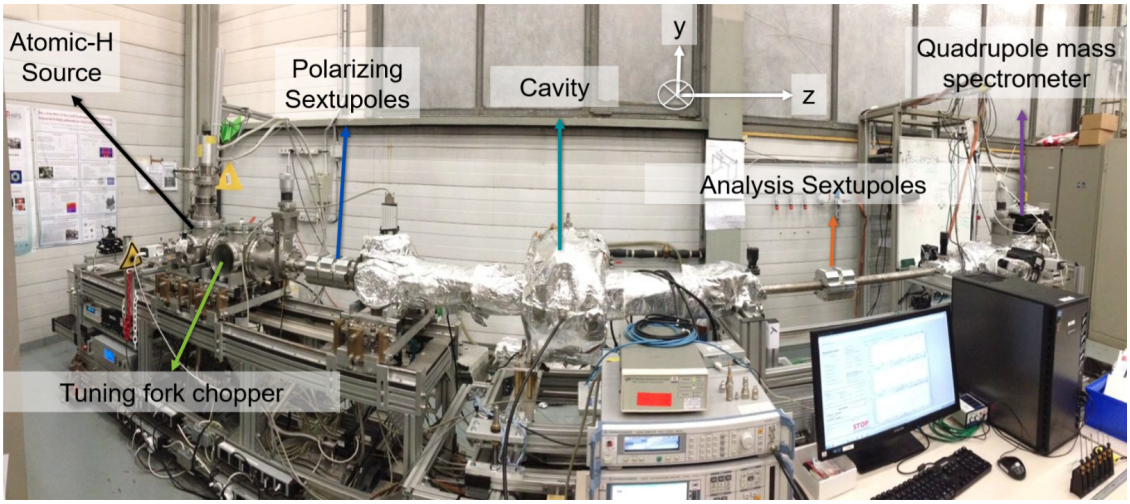

Figure 60 – Hydrogen beam experiment for measurements on the σ and π_1 transitions at bat. 275.

8 Proposed program for the hydrogen beam experiment

In this section we outline the future plans and propose the physics program, which includes both supportive measurements for $\overline{\mathrm{H}}$ as well as matter experiments with their own (i.e. antimatter-independent) merits.

The physics goals we strive to achieve in the parallel matter experiments up to the end of LS3 are listed below and described in more detail subsequently (referring to this numbering scheme):

1. Investigations of potential systematic effects from beam-trajectory variations in the σ/π-cavity assembly.

2. Further investigations on the resonance interaction at low fields observed with a 45° alignment between B_{osc} and B_{stat}.

3. When $\overline{\mathrm{H}}$ hyperfine spectroscopy is attempted during run 3, the hydrogen beam shall operate in parallel to provide a matter reference frequency, which is temporally and spatially well correlated.

4. Long-term measurements at few ppb precision with varying alignment of B_{stat} on the σ and π_1 transitions to put limits on so far unconstrained coefficients of the SME.

5. Pioneering the Ramsey method on measurements with hydrogen and deuterium at a precision level better than ppb, which promises extreme sensitivity to certain coefficients of the SME.

6. The experiences with the Ramsey apparatus for hydrogen and deuterium will guide the design of a Ramsey apparatus for $\overline{\mathrm{H}}$, which will be commissioned with hydrogen during LS3.

7. Testing the detection schemes for Rydberg hydrogen, which shall be used for the matter experiments with the ASACUSA-Cusp setup during LS2 (this requires the development of Rydberg excitation schemes for the hydrogen beam setup).

8. The availability of a beam of excited or Rydberg hydrogen atoms will also allow for the study of deexcitation schemes, which shall be applied to the $\overline{\mathrm{H}}$ beam in order to increase the number of ground-state atoms.

The tentative timetable correlating the individual points of the program to the AD run and shut down periods is given here:

	LS 2	Run 3	LS 3	Run 4
1) Trajectory independence				
2) Interference effect				
3) Reference for antihydrogen spectroscopy				
4) Swapping B_{stat}				
5) Ramsey H & D				
6) Ramsey antihydrogen				
7) Rydberg H detector tests				
8) Deexcitation studies				

8.1 Rabi experiment using the σ and π_1 transitions of hydrogen

ad 1) When proposing the idea of a Rabi-type hyperfine experiment on $\overline{\mathrm{H}}$ some assumptions on the anticipated beam parameters had to be made. The most important beam properties apart from intensity are the velocity distribution (or temperature), the beam profile, and the polarisation. Achieving a beam temperature of 50 to 100 K seems realistic and the hydrogen beam is tuned to operate at this velocity regime. Differences in polarisation should merely affect the observed signal-to-noise ratio, meaning that the same precision can be obtained with a smaller integral yield, if the polarisation is higher. However, differences in the beam profile might systematically influence the line-shape and the $\overline{\mathrm{H}}$ beam is expected to be significantly larger than the hydrogen beam. Therefore the σ/π-cavity assembly is mounted on a stage allowing for transverse (vertical and horizontal) movement of the cavity assembly with respect to the beam (compare left side of fig. 61). The beam position and profile can be investigated with a beam blocker using the rotating wire principle (compare right side of fig. 61). The combination of the movable cavity assembly and the helical beam blocker will allow for a detailed investigation of a potential trajectory dependence and remove this remaining unknown when transferring the conclusions from hydrogen tests onto $\overline{\mathrm{H}}$.

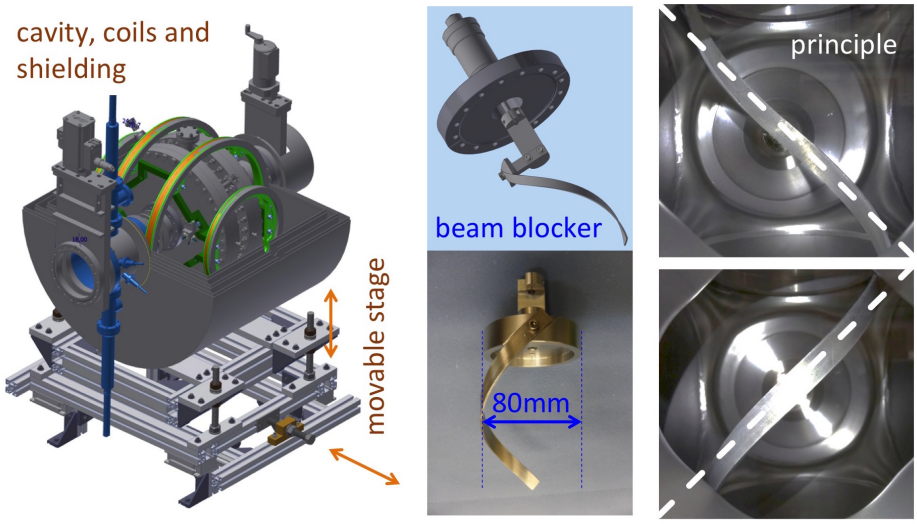

Figure 61 – Left: The σ/π-cavity assembly rests on stage that allow for transverse movement of the cavity assembly w.r.t. the hydrogen beam. Right: 3D-Drawing and photographs of the helical beam blocker also illustrating the operation principle for two-dimensional beam profile detection.

ad 2) As the interaction time is typically 100 μs (beam velocity $\sim$ 1 km/s, cavity length $\sim$ 100 mm) observed line widths are on the order of 10 kHz. At small B_{stat} the separation of the σ and π_1 transitions becomes comparable to the line width. For example, at 4.6 μT the separation decreases to 65 kHz. In the configuration with a 45° angle between the field (compare right of fig. 56), which allows for investigations of both transitions, this leads to interference effects and to asymmetric line shapes. If one continues to apply the symmetric fit function for a two-level system in this regime systematic shifts of the extracted central frequencies will arise. Figure 62 shows a numerical calculation of the state-conversion map based on the four-level system as expected for a B_{stat} of 4.6 μT illustrating the induced asymmetries in the observable lineshapes. This can be compared to the simpler, symmetric case in a two-level system as depicted in fig. 58.

Currently we apply corrections to compensate for the systematic shifts. The development of a fit procedure based on the complete four-level system of the ground-state hyperfine states is under consideration. However this is followed with lower priority as the interference effect can be avoided in two ways. At higher static fields the systematic shifts drop below the ppb level and are negligible for the first-stage goal of $\overline{\mathrm{H}}$ Rabi-spectroscopy, which is a ppm measurement. Alternatively, a purely parallel or orthogonal alignment between the fields allows for addressing the two transitions separately. This approach is followed in the design of the Ramsey apparatus (cf. sec. 8.2). Nevertheless, it remains intriguing to investigate the interference further. For instance the effect could be exploited for precise determinations of B_{stat}. Without the interference effect B_{stat} only shifts the resonance, while in the low-field regime the lineshape itself is altered, which should lead to increased fit-sensitivity. The hyperfine splitting determinations could benefit from a more precise calibration of the field. So far the constant, which translates the current on the coils into a magnetic field value have been obtained as fit parameters in present evaluations.

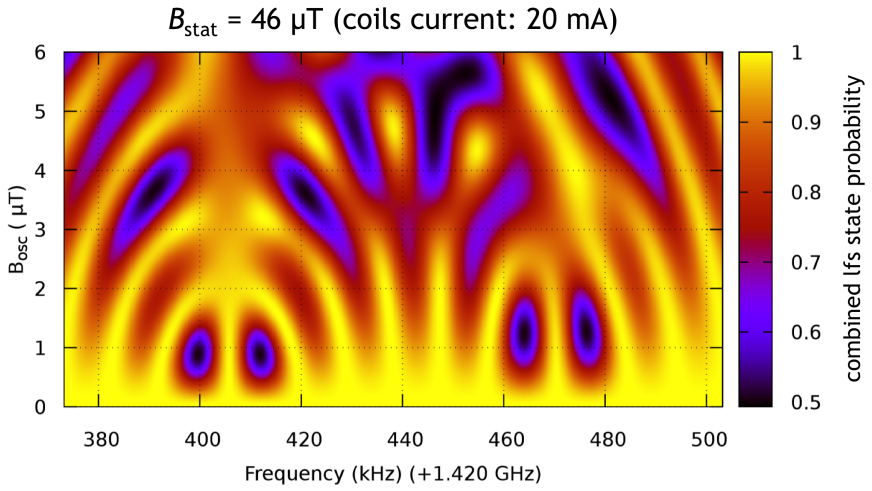

Figure 62 – Intensity plot showing the combined probability for the two low-field seeking states (i.e. the initial states of the σ and π_1 transition) as a function of the detune and B_{osc} as applied by the cavity and for a static magnetic field value of 46 μT. While the similar plot of fig. 58 is produced using numerical solutions of the two-level system here the complete four-level system of the ground-state hydrogen hyperfine structure has been solved; albeit for a mono-velocity beam. Especially for the π_1 transition (right structure) and at values of B_{osc} >3 μT the asymmetry due to the interference caused by the 45° alignment of the fields is clearly visible.

ad 3) We outlined the strategy towards the first Rabi-spectroscopy on $\overline{\mathrm{H}}$ in part II. Based on the main pillars of colder positrons and the support of proton mixing with high availability the clear goal is to realize this within the period of run 3. Once the intensity of the $\overline{\mathrm{H}}$ beam with useful properties has sufficiently increased the priority of the hydrogen beam experiments will shift to parallel operation in order to provide the best possible matter reference. At the first-stage precision goal of 1 ppm the choice of reference is not extremely crucial, however, if the ideal reference is available it should be used. For a CPT test this means taking measurements on hydrogen (the matter counterpart) at the same time and place as the $\overline{\mathrm{H}}$ measurement. In bat. 275 the hydrogen beam is only about 200 m separated from the AD hall. However, there is a slight deviation in alignment. With reasonable efforts it is also possible to move the hydrogen beam experiment to the AD hall or to set up a second experiment. A hydrogen beam setup at the AD hall would

be beneficial for excitation and deexcitation studies on hydrogen, which have the potential to significantly increase the production of ground state $\overline{\mathrm{H}}$ (compare section 8.3). A second source of atomic hydrogen is already available so that such goals do not interfere with other ongoing tasks.

ad 4) Antimatter investigations and comparison to matter are a direct and model-independent test of CPT symmetry. However, most coefficients of the Standard Model Extension can be tested with matter experiments. If a value different from zero was found, this would imply CPT or Lorentz violation. Such experiments are performed at high precision and over longer run periods to exploit the fact that the Earth is a rotating and moving system in the Sun-centered frame. If observations were to change with position, orientation or direction of the velocity one could discover it as sidereal or annual variations. Hydrogen maser measurements have been performed for this purpose [129]. Recently, the SME was extended to the non-minimal sector, including operators of arbitrary mass dimension. For (anti)hydrogen hyperfine spectroscopy, many new coefficients are added that also depend on the orientation of the applied static field [130]. The accessible coefficients by hydrogen hyperfine experiments are conveniently summarised in the notation $\mathcal{K}_{Wk1m}$ (for details compare section III B of Ref. [130] or the discussion for our experiments Ref. [131]). In total 24 SME coefficients in the laboratory system (i.e. Earth) then translate into 72 coefficients in the Sun-centered frame according to:

$$\mathcal{K}^{\mathrm{NR,lab}}_{\mathcal{W}k10} = \mathcal{K}^{\mathrm{NR,Sun}}_{\mathcal{W}k10}\cdot\cos\vartheta - \sqrt{2}\,\Re\Big(\mathcal{K}^{\mathrm{NR,Sun}}_{\mathcal{W}k11}\Big)\cdot\sin\vartheta\cdot\cos\omega_\oplus T_\oplus + \sqrt{2}\,\Im\Big(\mathcal{K}^{\mathrm{NR,Sun}}_{\mathcal{W}k11}\Big)\cdot\sin\vartheta\cdot\sin\omega_\oplus T_\oplus, \quad (26)$$

where ϑ is the angle between the Earth's rotational axis and B_{stat} and $\omega_\oplus$ is the Earth's rotation frequency of $2\pi/23\mathrm{h}56\mathrm{min}$. The maser measurements constrained 48 out of the 72 coefficients in the Sun-centered frame. The remaining 24 coefficients can be tested in our hydrogen beam experiment by long-term measurements, where the direction of B_{stat} gets swapped on a regular basis. A precision matching the one achieved in the maser measurements will be out of reach for now, however, the lack of constraints on these particular coefficients justifies this experiment also on the level of precision of Rabi spectroscopy. A later improvement is planned as soon as Ramsey spectroscopy on hydrogen has been tested.

8.2 Planned Ramsey experiment with hydrogen, deuterium, and $\overline{\mathrm{H}}$

ad 5) In-beam measurements on the hyperfine structure can attain higher precision by applying Ramsey's method of two separated oscillatory fields, which is an improved version of Rabi-spectroscopy. Therefore we have started the design of a Ramsey apparatus. It shall be capable of studying all σ and π transitions in both hydrogen and deuterium. The latter has in the non-minimal SME a high sensitivity to coefficients depending on the proton momentum in the deuterium nucleus [130]. In order to achieve this goal different frequencies and matching respective orientations of B_{osc} and B_{stat} have to be provided. Resonance interferences as discussed in 8.1 shall be avoided by either having parallel or orthogonal alignment. Similar as for the existing cavity assemblies the apparatus will consist of devices providing the microwaves, coil configurations to provide the static field and a surrounding magnetic shielding to block external stray fields and Earth's magnetic field. An overview the required frequencies and field alignments for the various transition is given in tab. 3 together with the currently envisioned solution to provide the microwaves. Strip-line travelling wave structures are being designed with the help of CERN RF expert Dr. Fritz Caspers, which enable a large frequency range to accommodate both hydrogen and deuterium frequencies. Since travelling waves have a transverse magnetic field, additional RF structures are needed to provide longitudinal B_{osc}. Here a TE_{011} cavity for H and a split-ring resonator for D are being studied.

Finding a coil configuration for providing B_{stat} with sufficient homogeneity over the entire length appears to be the simpler task according to simulations. A grant application to fund production of this device and the required microwave and current supplies has been submitted in May this year.

Atom	Transition (ν_c)	Trans. freq. ($B_{\text{stat}} = 0$)	Field alignment	Microwave device
H	σ	1.42 GHz	$B_{\text{osc}} \parallel B_{\text{ext}}$	cavities
	π_1	1.42 GHz	$B_{\text{osc}} \perp B_{\text{ext}}$	travelling wave structure
	π_2	0 GHz	$B_{\text{osc}} \perp B_{\text{ext}}$	travelling wave structure
D	σ_1, σ_2	327 MHz	$B_{\text{osc}} \parallel B_{\text{ext}}$	split ring resonator
	π_1, π_2	327 MHz	$B_{\text{osc}} \perp B_{\text{ext}}$	travelling wave structure
	π_3	0 MHz	$B_{\text{osc}} \perp B_{\text{ext}}$	travelling wave structure

Table 3 – Requirements for accessing different transitions in hydrogen and deuterium.

A sketch of the current design status is shown in fig. 63 (a) together with the Breit-Rabi diagram for deuterium and hydrogen (b). The axial orientation of B_{stat} could allow for a field calibration using slow electrons, which are guided through the entire apparatus. Therefore the electron cyclotron frequency with it's direct scaling with B_{stat} is also included in the Breit-Rabi diagram of fig. 63 (b).

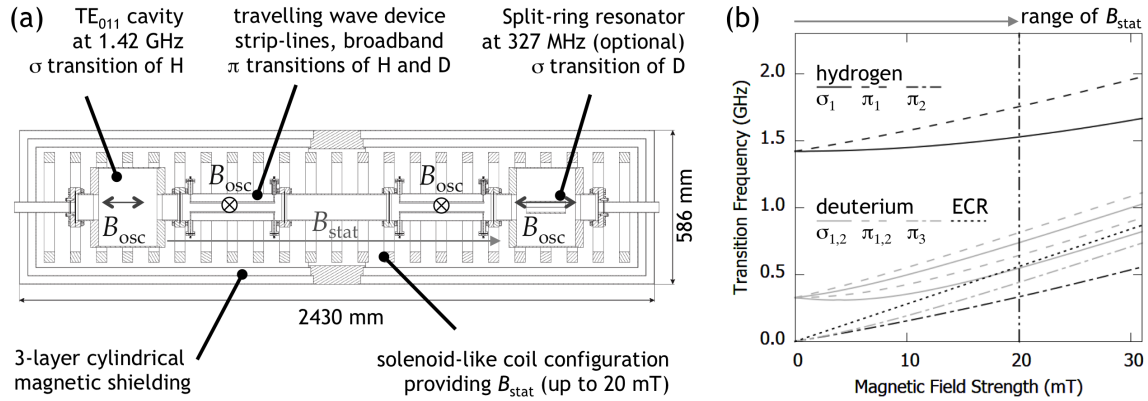

Figure 63 – (a) Schematic of the Ramsey spectrometer design showing the cavities, strip-line structures, the non-interacting zone in the center, the solenoidal coils and the shielding. (b) Transition frequencies in the GS-HFS in hydrogen and deuterium and the electron cyclotron resonance frequency, versus the static magnetic field strength B_{stat}.

The design phase will be concluded soon and we expect construction to begin early 2020 and hopefully first results soon thereafter. This device is dedicated to matter experiments and has a smaller open diameter than the $\overline{\text{H}}$ Rabi-spectrometer (40 mm compared to 100 mm). We have chosen to take this intermediate step on the way towards Ramsey-spectroscopy on $\overline{\text{H}}$ for two reasons. It does not seem realistic to complete Rabi-spectrocopy within the run 3 period, therefore the availability of Ramsey apparatus for $\overline{\text{H}}$ is not crucial within the next five years. Devising the apparatus with the flexibility to investigate deuterium as well vastly increases the sensitivity of ASACUSA's matter experiments to certain coefficients of the SME. The prospective searches for the signals of Lorentz and CPT violations would be in sidereal variations of transition frequencies at the first and second harmonic of the sidereal frequency (compare Eqs. (48) and (123) of Ref. [130]

for the hyperfine structure). The quantities contributing to the energy shifts depend on coefficients for Lorentz and CPT violation, namely, a_{wkjm}, c_{wkjm}, g_{wkjm} and H_{wkjm} (as described in Eq. (6) of Ref. [130]). In deuterium, the energy shifts depend on the expectation values $\langle \boldsymbol{p}_{pd} \rangle$, $\langle \boldsymbol{p}_{pd}^2 \rangle$ and $\langle \boldsymbol{p}_{pd}^4 \rangle$, where $\boldsymbol{p}_{pd}$ is the momentum of the proton relative of the centre of mass of deuteron. This being significantly different from that of hydrogen, leads to the enhancement of the sensitivity of coefficients for Lorentz and CPT violation [130] by a factor of 10^9 for coefficients with $k = 2$ and 10^{18} for coefficients with $k = 4$.

ad 6) The experiences collected in Ramsey experiments with hydrogen and deuterium will guide the design of an equivalent apparatus for $\overline{\mathrm{H}}$, which will enable hyperfine spectroscopy on $\overline{\mathrm{H}}$ on the 10 ppb level after LS3. Assuming we succeed with both, Rabi-spectroscopy on $\overline{\mathrm{H}}$ and Ramsey-spectroscopy on hydrogen within the next five years we expect a fast design, construction, and matter-testing of an $\overline{\mathrm{H}}$ Ramsey-spectrometer during LS3. This can lead directly to Ramsey-spectroscopy on $\overline{\mathrm{H}}$ during the run 4 period.

8.3 Experiments with a beam of excited hydrogen

A new source of hydrogen was built at SMI and characterized at CERN. It will be used to produce a beam of excited hydrogen for different tests during LS2.

ad 7) The first step towards creating a beam of Rydberg state hydrogen is to excite to the 2S metastable state. This will produce a beam of H(2S) which can be further excited to H(n,l) states using a laser as described below. To create H(2S), electron impact excitation will be used as shown in in equation 27:

$$\mathrm{e}^- + \mathrm{H} \rightarrow \mathrm{H}^* + \mathrm{e}^- \tag{27}$$

To achieve this, an experimental setup as shown in figure 64 will be produced following the work of ref [132]. An electron emitter fires an intense ($\sim$mA cm^{-2}) electron beam with an energy of

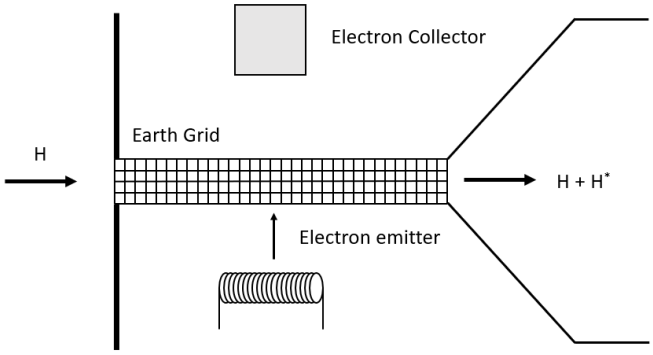

Figure 64 – Sketch of the experimental arrangement needed to produce H(2S).

the order 10 eV through the earth grid where the hydrogen beam is shielded from external electric fields (this is necessary to prevent stark mixing of the 2S and 2P states reducing the lifetime of the 2S state). The electron collector will be biased to collect the beam and so the intensity can be monitored.

Given a beam intensity of approximately 1×10^{17} Hz, and an electron current areal density of 2 mA cm^{-2} following the estimates in [132] we find the following for a 6 mm production length and a 50 K beam the transit time is approximately 6 μS the conversion rate is 1.3×10^{-6}, quenching from electron impact was estimated at 20% and from res gases at 30% solid angle of course depends on as yet undecided geometry. However in the production region this yields 7×10^{10} Hz. Using the measured beam in [132] which was 2 orders lower than their estimate and a solid angle of 1×10^{-4} which could be for a 1mm aperture 6mm from the production region, then we may observe a beam intensity around 5×10^{4} Hz.

This beam will be detected downstream on a position sensitive delay line detector (DLD80) to test the efficiency of detecting metastable H, a method routinely used for other metastable atomic beams [133]. This method will be used in the antihydrogen apparatus as described in section 5.1 to text mixing strategies with matter.

ad 8) Fig. 65 shows a simplified sketch of a beamline to test the light-stimulated deexcitation of Rydberg hydrogen which was introduced in sec. 5.4.2. The hydrogen source will be followed by an electron discharge to excite hydrogen to the 2s-state by overcoming the very strong binding energy in the XUV range. In a second stage a laser (828-839 nm depending on the Rydberg state targeted) will be added in the presence of electric and magnetic fields to populate a wide range of sub-levels. Deexcitation by light will be performed in the following chamber. The state distribution of the atoms will finally be detected by a field-ionizer coupled to an MCP for charge detection.

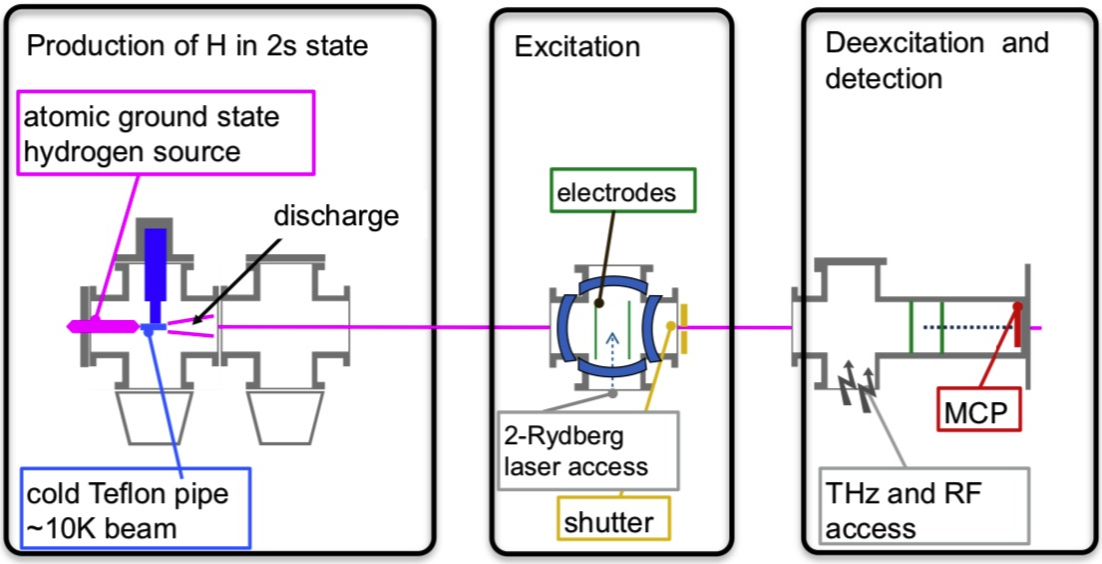

Figure 65 – Sketch of the experimental setup for testing hydrogen stimulated deexcitation with light.

In the first stage, while lasers are being implemented, different sources of THz and RF light will be tested with the smaller and less controllable flux of Rydberg hydrogen provided by the electron discharge (amount of which still needs to be investigated). Those first tests can be done at the current location of the the hydrogen beam setup (building 275) and will give a first insight in the efficiency of the deexcitation mechanism envisioned for antihydrogen. The setup coupled to lasers will be moved to the ASACUSA area at the AD.

Part V
Other longer-term options

9 Slow-extracted low-energy antiproton beam facility

9.1 Introduction

Low energy antiproton-proton annihilation was extensively studied at LEAR by the ASTERIX, CRYSTAL BARREL and OBELIX collaborations [134]. Apart from the pion multiplicity distributions, which are in fair agreement with statistical models, details on the annihilation process are not understood. Evidence for quarks dynamics was obtained, but the exact mechanism involving quarks is still unclear, in particular, the origin of the strong violation of the OZI rule in ϕ production (possibly due to sea (anti)quarks in the (anti)nucleon). The mechanism underlying the rare annihilations, involving more than one nucleon, is also not understood.

Antiproton-nucleus annihilation was studied by a few experiments in LEAR (e.g. PS186 and PS203 [135, 136]) which provided significant insight in the processes that occur when antiprotons are stopped in different nuclei. These experiments used antiprotons with energies between 20 and 200 MeV and produced a number of results on measured cross-sections and yielded spectra of light particles emitted by stopped antiprotons in nuclei using telescopes. The deduced transferred and excitation energies showed good agreement with the intranuclear cascade model [136]. Another important question that was investigated were the residual nuclei, i.e. what is left of a nucleus after annihilation. Starting a few minutes after the irradiation with antiprotons, the radioactivity of the activated material was measured using Ge detectors for the gamma spectra [137–139].

9.1.1 Fragmentation and final state interaction

The antinucleon-nucleus inelastic interaction includes phenomena similar to those occurring on free nucleons, i.e. annihilation on a single nucleon and inelastic scattering with or without break-up of the nucleus, depending on the interaction between the final products of the previous reactions and the residual nuclear fragments (final-state interaction (FSI) or re-scattering). Moreover, exotic phenomena, where the antiprotons annihilate on two or more nucleons (B $>$ 0 systems) are also possible.

Despite the previous efforts (e.g. in LEAR), full experimental and theoretical treatment of the final state interactions are still missing. This implies the need for a deeper understanding of the possible scenarios that the nucleus can undergo, as well as on the different mechanisms (e.g. absorption, charge exchange) through which some of the primarily produced pions can re-interact with the residual nucleus. Measuring the total multiplicity e.g. of charged annihilation prongs and their identification would provide experimental data to reveal the details of these processes.

Measurements on the multiplicity of Minimum Ionizing Particles (MIP) and Heavily Ionizing Particles (HIP) from low-energy antiproton annihilation in three different materials were carried out in the AEgIS experiment, using emulsion films [140]. Comparison against models used by simulation packages such as GEANT4 and FLUKA were performed, and it was found that the latter is in good agreement with the measured data. However, the statistics in this study were limited, with $<$ 1000 annihilation events per material. In ASACUSA, as elaborated in the next section, we have started a systematic study, measuring the products of antiproton annihilation at

rest with different nuclei, combining two different detectors. For measuring the total multiplicity (i.e. $\sim 4\pi$), a continuation of this study with a new set-up is required.

9.2 Slow extraction of antiprotons in ASACUSA

9.2.1 Measurement of multiplicitites

During the beam time in 2017 and 2018, we have carried out measurements of antiproton-nucleus annihilation at rest on three different nuclei: carbon, gold and molybdenum [141, 142]. The measurements were performed within several shifts at the end of each beam campaign. The concept was advantageous over previous experiments in a few aspects: the slow extraction of antiprotons (∼150 eV) allowed the use of thin targets (1-2 μm), which, in turn, allowed the emergence and detection of heavier nuclei produced in the annihilation.

The combination of two detectors provided simultaneous detection of pions (> 80 % of the 4π solid angle), protons, alphas and other heavier fragments (∼ 25 % of the 4π solid angle). Ultimately, the slow extraction method combined with the focusing using Einzel lenses and the biased foil produced a well defined beam and, in turn, a very clean signal from individual annihilations, e.g. with zero background (see figure 66 left). The goal of this study was validation of the GEANT4 physics models for antiproton annihilation at rest, which are extensively used for detector design and optimization of the detection efficiency in the AD community. The analysis and the simulations are being finalized and the results are expected to be published in the next months (e.g. figure 66 right shows the number of reconstructed 3D pion tracks per antiproton annihilation for different nuclei, recorded with the Hodoscope).

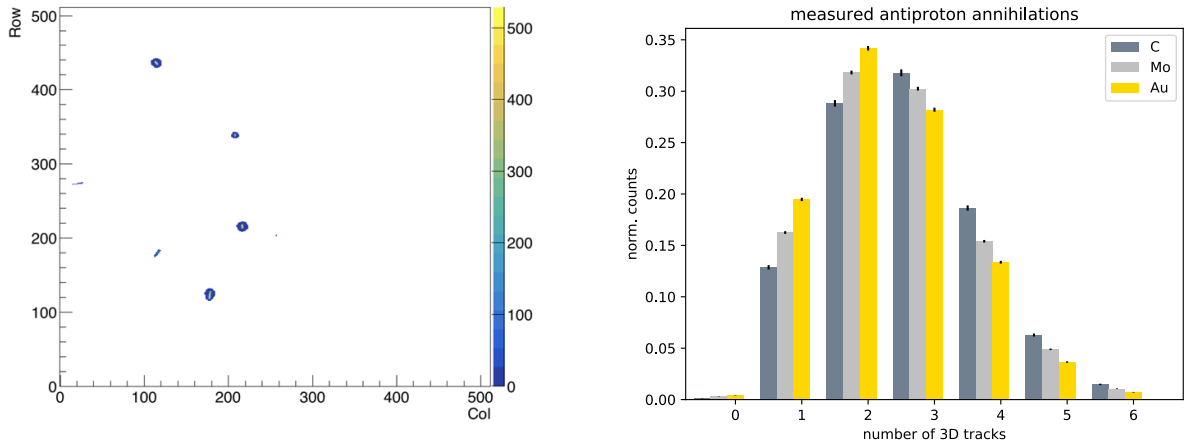

Figure 66 – Left: Fragments from individual annihilation, as recorded with the Timepix3, Right: Number of 3D reconstructed pion tracks per annihilation (recorded with the Hodoscope).

As discussed in section 5.3.4, the antiproton reservoir trap, which is one of the foreseen upgrades on the ASACUASA apparatus towards increasing the rate of produced antihydrogen, opens the possibility for a parasitic beam line for physics measurements with slow extracted low-energy antiprotons. As shown in figure 47 in section 5.3, antiprotons from the reservoir trap will be electrostatically guided upstream, where they will meet a cylindrical deflector lens element. In normal operation this element is grounded, allowing antiprotons from MUSASHI to pass through and be stored in the reservoir. The deflector will turn the slow extracted beam through 90° into focusing elements which will deliver antiprotons to the target. Preliminary ion optics simulations that we

have carried out show that, for a 200 eV beam with a 0.8 mm diameter, $> 95\%$ of the antiprotons are transmitted.

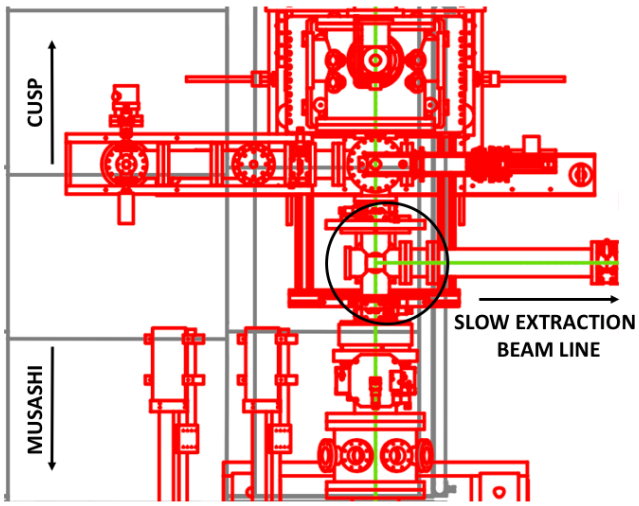

Figure 67 – A zoom-in layout of the experimental zone with the 90° deviation for the slow extraction beam line (in black circle)

A new detection system, based on silicon pixel detectors is foreseen to be installed downstream the beam line. Given the successful use of Timepix3 in our previous experiment, we intend to build a detector using multiple Timepix3 (and/or the upcoming Timepix4) ASICs developed by the Medipix3/Medipix4 Collaboration at CERN [143], which would be able to measure the charged annihilation prongs in $\sim 4\pi$ solid angle. The first physics measurements will be an extension on our previous fragmentation studies, including a larger number of stable nuclei (e.g. > 10), thus providing a data base on the total multiplicity of charged particles for antiproton-nucleus annihilation at rest.

A potential synergy for these measurements is being discussed with a recently proposed experiment, PUMA [144], which main goal is to study the ratio of neutron-antiproton and proton-antiproton annihilations in unstable nuclei. Their method is based on the detection of the charged pions in the annihilaiton, so precise determination of the FSI is crucial to their success. At the moment, because of the lack of a simulation code for antiproton-nucleus annihilation at rest, they have implemented antiproton-induced reactions with heavy ions inside the Intra-Nuclear Cascade of Liège (for incident energies ranging from a few tens of MeV to a few GeV) [145], which, on the other hand, defines the pion-nucleon interactions from experimental data. Measurements of the different channels for antiproton-nucleus annihilations with a good efficiency and constraints on final state interactions are complementary to the validation process of the parametrization of the FSI with a model, foreseen in PUMA. In fact, such data are necessary for any future development on a fully microscopic and consistent treatment of the antiproton-nucleus many-body problem.

A rough estimation of the necessary beam time can be deduced from our previous measurements: given the repetition rate of the antiproton bunches at the AD ($\sim$100 s) and the time needed for the required manipulations for the slow extraction (e.g. electron cooling), the data for three different elements were obtained within seven 8-hours shifts. About 150 antiproton shots/element were used, which, considering the foreseen continuous operation of ELENA, means that the data for a single element could be taken in less than half a day. The data taking is intended to be parasitic to the main experiment and adjusted in a non-pertubative way. The measurements with slow

extracted antiprotons will be carried out e.g. during times needed for offline analysis or hardware developments on the main apparatus. A parallel operation (e.g. during potential longer manipulations in the CUSP) could also be investigated. The successful implementation and operation of the slow extraction beam line will open the possibility for carrying out a variety of other experiments. Depending on the interest from different AD groups and the potential to build up a larger community, the slow extraction beam line could become a new experimental installation with a much broader physics program.

9.2.2 Further possible measurements with slow extracted antiprotons

Pontecorvo reactions The annihilations involving more than one nucleon were proposed in 1956 by Bruno Pontecorvo. Two-body final states in annihilations on two nucleons, such as $\bar{p}d \to \pi^- p, \Lambda K^0, \Sigma^0 K^0$, have been measured at LEAR. The rates are very small, lying between 10^{-6} and 10^{-5}. Attempts to describe these reactions, by rescattering of the pions or kaons from annihilation on the first nucleon, on the second nucleon, lead to much larger branching ratios, or are prone to orders of magnitude short range uncertainties or form factors.

A much more promising approach is that of the fireball model [146,147] in which a highly excited $3\overline{q}6q$ bag decays into the observed final state through quark annihilation and rearrangement (fig.68, left) . The annihilation rate of protons on two nucleons is given by the probability to form a fireball (on the first nucleon then propagating to the second one), times the normalized final state phase space factor. From the measured $\overline{\mathrm{p}}\mathrm{d} \to \pi^-\mathrm{p}$ branching ratio the fireball formation probability is about 3%. This leads to the branching ratios 3×10^{-6} for $\bar{p}d \to \Lambda K^0$ and $\Sigma^0 K^0$, in excellent agreement with data [148].

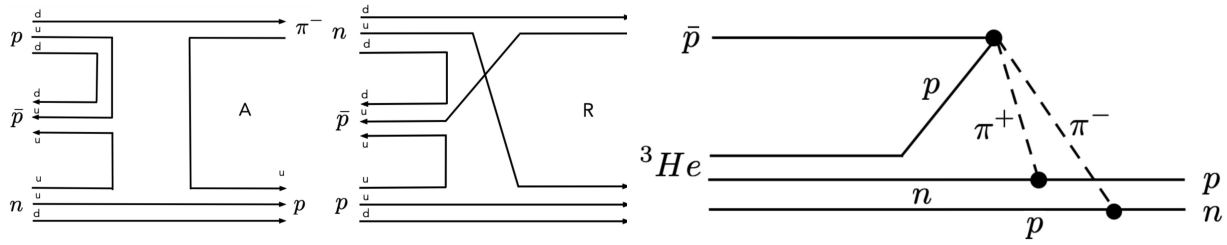

Figure 68 – Left: annihilation and rearrangement graphs in the fireball model. Right: rescattering diagram for $\overline{\mathrm{p}}^3\mathrm{He} \to np$.

The fireball model can now be checked by studying annihilation on three nucleons (fireball propagating to the third nucleon) such as $\overline{\mathrm{p}}^3\mathrm{He} \to np$ or $\overline{\mathrm{p}}^3\mathrm{H} \to nn$, for which no data exist yet. The rates are expected to be of the order of 10^{-6} [147] much in contrast to the 10^{-8} to 10^{-7} predicted for the rescattering graph in fig.68 (right) [149]. This can be done by measuring the 1 GeV back-to-back nucleons with calorimeters.

After the initial series of measurements, the slow extraction facility can be upgraded for measuring rare annihilation at rest, such as $\overline{\mathrm{p}}3\mathrm{N} \to \overline{\mathrm{p}}^3\mathrm{He}$ or $\overline{\mathrm{p}}^3\mathrm{H}$. A successful outcome would provide the first observation of annihilation on three nucleons. The ASACUSA collaboration traps currently some 10^6 antiprotons/AD cycle (100s), which could be slowly released between two cycles with an intensity of $\simeq 10^4$ s^{-1}, comparable to that in CRYSTAL BARREL at LEAR. This experiment would require cryogenic targets such as solid hydrogen, or ion traps, as well as detector upgrade. A quantitative evaluation on the production rates and the solid angle detection efficiency is in progress. Depending on the available resources, this measurement might still be feasible before LS3.

Antiprotonic atoms Other measurements, e.g. beyond LS3, could include the formation and study of decay processes of antiprotonic atoms, which are of special interest for probing the nuclear periphery. In the first years of operation of the AD, after ASACUSA demonstrated the successful production of a slow extracted antiproton beam [150,151], external groups with previous experience from different LEAR experiments expressed interest for potential collaboration, for measurements on antiprotonic atoms. As a result, such ideas were included as part of the ASACUSA proposal in 2002 [152], but were never carried out, to a great extent because of the scarce beam time. If the slow extraction beam facility is upgraded for this kind of studies, QED tests in antiprotonic atoms with heavy nuclei (e.g. Kr, Ar, Xe) via X-ray spectroscopy would also become feasible. However, these measurements would require a much larger installation, and hence another 90° bend to the currently foreseen one, e.g. for a needed acceleration stage for the antiprotons to 100 keV, to enter a gas target, or a gas jet. Such a major effort would be possible only with joint forces with other groups. Our preliminary discussions inside the AD community revealed potential interest for such measurements from other collaborations, which might easily result in a cross-collaboration. More long term prospects could include even more exotic ideas, such as quantification of the production of hyper nuclei in antiproton-nucleus collisions.

9.2.3 Funding and resources

For the realization of the slow extraction facility in ASACUSA, including the antiproton reservoir trap, we intend to seek funding from FWF (Austrian Research Funding Agency) within the next months, and if successful, to set-up a small group of one post-doc, one PhD student and master students working on its development and realization. A recent ECT* Trento workshop [153] on antiproton-nucleus interactions and related phenomena reaffirmed the fact that low energy antiprotons are a powerful tool for probing the nuclear structure that remains unexploited, despite their great potential to close many open questions in this field. Our idea is to make use of the utility and the capacity of ELENA to fill these gaps.

References

[1] V. I. Korobov, L. Hilico, and J.-P.. Karr, *Phys. Rev. Lett.*, vol. 112, p. 103003, 2014.

[2] V. I. Korobov, L. Hilico, and J.-P.. Karr", *Phys. Rev. A*, vol. 89, p. 032511, 2014.

[3] V. I. Korobov, *Phys. Rev. A*, vol. 89, p. 014501, 2014.

[4] V. I. Korobov, L. Hilico, and J.-P.. Karr, *Hyperfine Int.*, vol. 233, p. 75, 2015.

[5] M.-H.. Hu *et al.*, *Chem. Phys. Lett.*, vol. 654, p. 114, 2016.

[6] D. Baye, J. Dohet-Eraly, and P. Schoofs, *Phys. Rev. A*, vol. 99, p. 022508, 2019.

[7] M. Ahmadi, B. X. R. Alves, C. J. Baker, W. Bertsche, E. Butler, A. Capra, C. Carruth, C. L. Cesar, M. Charlton, S. Cohen, R. Collister, S. Eriksson, A. Evans, N. Evetts, J. Fajans, T. Friesen, M. C. Fujiwara, D. R. Gill, A. Gutierrez, J. S. Hangst, W. N. Hardy, M. E. Hayden, C. A. Isaac, A. Ishida, M. A. Johnson, S. A. Jones, S. Jonsell, L. Kurchaninov, N. Madsen, M. Mathers, D. Maxwell, J. T. K. McKenna, S. Menary, J. M. Michan, T. Momose, J. J. Munich, P. Nolan, K. Olchanski, A. Olin, P. Pusa, C. O. Rasmussen, F. Robicheaux, R. L. Sacramento, M. Sameed, E. Sarid, D. M. Silveira, S. Stracka, G. Stutter, C. So, T. D. Tharp, J. E. Thompson, R. I. Thompson, D. P. van der Werf, and J. S. Wurtele, "Observation of the 1s-2s transition in trapped antihydrogen," *Nature*, vol. 541, p. 506, Dec. 2016. [Online]. Available: http://dx.doi.org/10.1038/nature21040

[8] M. Ahmadi, B. X. R. Alves, C. J. Baker, W. Bertsche, A. Capra, C. Carruth, C. L. Cesar, M. Charlton, S. Cohen, R. Collister, S. Eriksson, A. Evans, N. Evetts, J. Fajans, T. Friesen, M. C. Fujiwara, D. R. Gill, J. S. Hangst, W. N. Hardy, M. E. Hayden, C. A. Isaac, M. A. Johnson, J. M. Jones, S. A. Jones, S. Jonsell, A. Khramov, P. Knapp, L. Kurchaninov, N. Madsen, D. Maxwell, J. T. K. McKenna, S. Menary, T. Momose, J. J. Munich, K. Olchanski, A. Olin, P. Pusa, C. O. Rasmussen, F. Robicheaux, R. L. Sacramento, M. Sameed, E. Sarid, D. M. Silveira, G. Stutter, C. So, T. D. Tharp, R. I. Thompson, D. P. van der Werf, and J. S. Wurtele, "Characterization of the 1s-2s transition in antihydrogen," *Nature*, vol. 557, no. 7703, pp. 71–75, May 2018.

[9] M. Hori *et al.*, *Science*, vol. 354, p. 610, 2016.

[10] M. Hori and others", *Nature*, vol. 475, p. 484, 2011.

[11] M. Hori and V. I. Korobov, *Phys. Rev. A*, vol. 81, p. 062508, 2010.

[12] J. Biesheuvel *et al.*, *Nature Communications*, vol. 7, p. 10385, 2016.

[13] J. Koelemeij, B. Roth, A. Wicht, I. Ernsting, and S. Schiller, *Phys. Rev. Lett.*, vol. 98, p. 173002, 2007.

[14] S. Alighanbari, M. G. Hansen, V. I. Korobov, and S. Schiller, *Nature Physics*, vol. 14, p. 555, 2018.

[15] R. Pohl *et al.*, *Nature*, vol. 466, p. 213, 2010.

[16] A. Beyer *et al.*, *Science*, vol. 358, p. 79, 2017.

[17] H. Fleurbaey *et al.*, *Phys. Rev. Lett.*, vol. 120, p. 183001, 2018.

[18] P. J. Mohr, D. B. Newell, and B. N. Taylor, *Rev. Mod. Phys.*, vol. 88, p. 035009, 2016.

[19] P. J. Mohr, B. N. Taylor, and D. B. Newell, *Rev. Mod. Phys.*, vol. 84, p. 1527, 2012.

[20] F. Heiße *et al.*, *Phys. Rev. Lett.*, vol. 119, p. 033001, 2017.

[21] S. Sturm *et al.*, *Nature*, vol. 506, p. 467, 2014.

[22] G. Gabrielse *et al.*, *Phys. Rev. Lett.*, vol. 82, p. 3198, 1999.

[23] J. K. Thompson, S. Rainville, and D. E. Pritchard, *Nature*, vol. 430, p. 58, 2004.

[24] S. Ulmer, C. Smorra, A. Mooser, K. Franke, H. Nagahama, G. Schneider, T. Higuchi, S. Van Gorp, K. Blaum, Y. Matsuda *et al.*, "High-precision comparison of the antiproton-to-proton charge-to-mass ratio," *Nature*, vol. 524, no. 7564, pp. 196–199, 2015.

[25] R. J. Hughes and B. I. Deutch, *Phys. Rev. Lett.*, vol. 69, p. 578, 1992.

[26] E. J. Salumbides, W. Ubachs, and V. I. Korobov, *J. Mol. Spect.*, vol. 300, p. 65, 2014.

[27] J. Murata and S. Tanaka, *Class Quantum Grav.*, vol. 32, p. 033001, 2015.

[28] M. S. Safronova *et al.*, *Rev. Mod. Phys.*, vol. 90, p. 025008, 2018.

[29] F. Ficek *et al.*, *Phys. Rev. Lett.*, vol. 120, p. 183002, 2018.

[30] Y. J. Kim, P.-H. Chu, and I. Savukov, *Phys. Rev. Lett.*, vol. 121, p. 091802, 2018.

[31] M. Hori, A. Sótér, and V. I. Korobov, *Phys. Rev. A*, vol. 89, p. 042515, 2014.

[32] V. I. Korobov, A. K. Bakbaev, D. T. Aznabayev, and S. A. Zhaugasheva, *J. Phys. B: At. Mol. Opt. Phys*, vol. 48, p. 0245006, 2015.

[33] B. Obreshkov and D. Bakalov, *Phys. Rev. A*, vol. 93, p. 062505, 2016.

[34] M. Hori *et al.*, *Phys. Rev. Lett.*, vol. 89, p. 093401, 2002.

[35] H. Yamaguchi *et al.*, *Phys. Rev. A*, vol. 66, p. 022504, 2002.

[36] H. Yamaguchi and others", *Phys. Rev. A*, vol. 70, p. 012501, 2004.

[37] M. Hori and others", *Phys. Rev. A*, vol. 70, p. 012504, 2004.

[38] T. Kobayashi *et al.*, *J. Phys. B: At. Mol. Opt. Phys.*, vol. 46, p. 245004, 2013.

[39] O. I. Kartavtsev, D. E. Monakhov, and S. I. Fedotov, *Phys. Rev. A*, vol. 61, p. 062507, 2000.

[40] V. I. Korobov, Z.-X. Zhong, and Q.-L. Tian, *Phys. Rev. A*, vol. 92, p. 052517, 2015.

[41] M. Hori *et al.*, *Phys. Rev. Lett.*, vol. 94, p. 063401, 2005.

[42] G. Ya. Korenman and S. N. Yudin, *J. Phys.: Conf. Ser.*, vol. 88, p. 012060, 2007.

[43] J. Zatorski and K. Pachucki, *Phys. Rev. A*, vol. 82, p. 052520, 2010.

[44] V. I. Korobov, *Phys. Rev. A*, vol. 73, p. 022509, 2006.

[45] T. Pask *et al.*, *Phys. Lett. B*, vol. 678, p. 55, 2009.

[46] S. Friedreich *et al.*, *Phys. Lett. B*, vol. 700, p. 1, 2011.

[47] S. Friedreich and others", *J. Phys. B: At. Mol. Opt. Phys.*, vol. 46, p. 125003, 2013.

[48] V. I. Korobov, *Phys. Rev. A*, vol. 61, p. 064503, 2000.

[49] S. P. Goldman, *Phys. Rev. A*, vol. 57, p. R677, 1998.

[50] G. W. F. Drake, *Phys. Scr.*, vol. T83, p. 83, 1999.

[51] D. L. Farnham, R. S. Van Dyck Jr., and P. B. Schwinberg, *Phys. Rev. Lett.*, vol. 75, p. 3598, 1995.

[52] E. G. Adelberger, B. R. Heckel, and A. E. Nelson, *Ann. Rev. Nucl. Part. Sci.*, vol. 53, p. 77, 2003.

[53] T. W. Murphy, *Rep. Prog. Phys.*, vol. 76, p. 7, 2013.

[54] J. M. Pendlebury *et al.*, *Phys. Rev. D*, vol. 92, p. 092003, 2015.

[55] S. Weinberg, *Phys. Rev. Lett.*, vol. 40, p. 223, 1978.

[56] F. Wilczek, *Phys. Rev. Lett.*, vol. 40, p. 279, 1978.

[57] J. E. Moody and F. Wilczek, *Phys. Rev. D*, vol. 30, p. 130, 1984.

[58] B. A. Dobrescu and I. Mocioiu, *J. High Energy Phys.*, vol. 11, p. 005, 2006.

[59] D. J. Marsh, *Phys. Rep.*, vol. 643, p. 1, 2016.

[60] V. Anastassopoulos *et al.*, *Nature Physics*, vol. 13, p. 584, 2017.

[61] R. Ballou *et al.*, *Phys. Rev. D*, vol. 92, p. 092002, 2015.

[62] P. Sikivie, *Phys. Rev. Lett.*, vol. 113, p. 201301, 2014.

[63] K. V. Tilburg, N. Leefer, L. Bougas, and D. Budker, *Phys. Rev. Lett.*, vol. 115, p. 011802, 2015.

[64] G. T. Condo, *Phys. Lett.*, vol. 9, p. 65, 1964.

[65] J. E. Russell, *Phys. Rev. Lett.*, vol. 23, p. 63, 1969.

[66] K. Assamagan *et al.*, *Phys. Rev. D*, vol. 53, p. 6065, 1996.

[67] S. Lenz *et al.*, *Phys. Lett. B*, vol. 416, p. 50, 1998.

[68] M. Trassinelli *et al.*, *Phys. Lett. B*, vol. 759, p. 583, 2016.

[69] M. Daum, R. Frosch, and P.-R. Kettle, *Phys. Lett. B*, vol. 796, p. 11, 2019.

[70] M. Hori *et al.*, *Phys. Rev. Lett.*, vol. 87, p. 093401, 2001.

[71] B. D. Obreshkov *et al.*, *Phys. Rev. A*, vol. 69, p. 042701, 2004.

[72] M. Hori and A. Dax, *Opt. Lett.*, vol. 34, p. 1273, 2009.

[73] T. Iwashita *et al.*, *Phys. Rev. Special Topics*, vol. 14, p. 071301, 2011.

[74] K. Takayama *et al.*, *Nucl. Instrum. Meth. A*, vol. 733, p. 182, 2014.

[75] J. Holma and M. J. Barnes, *IEEE Trans. Plasma Science*, vol. 42, p. 2899, 2014.

[76] K. Nordlund, D. Sundholm, P. Pyykkö, D. M. Zambrano, and F. Djurabekova, *Phys. Rev. A*, vol. 96, p. 042717, 2017.

[77] M. Hori, K. Yamashita, R. S. Hayano, and T. Yamazaki, *Nucl. Instrum. Meth. A*, vol. 496, p. 102, 2003.

[78] A. Sótér, K. Todoroki, T. Kobayashi, D. Barna, D. Horváth, and M. Hori, *Rev. Sci. Instrum.*, vol. 85, p. 023302, 2014.

[79] K. Todoroki *et al.*, *Nucl. Instrum. Meth. A*, vol. 835, p. 110, 2016.

[80] Y. Murakami, H. Aghai-Khozani, and M. Hori, *Nucl. Instrum. Meth. A*, vol. 933, p. 75, 2019.

[81] D. F. Anderson *et al.*, *Nucl. Instrum. Meth. A*, vol. 290, p. 385, 1990.

[82] C. L. Woody *et al.*, *IEEE Trans. Nucl. Science*, vol. 40, p. 546, 1993.

[83] R. D. Appuhn *et al.*, *Nucl. Instrum. Meth. A*, vol. 350, p. 208, 1994.

[84] P. Achenbach *et al.*, *Nucl. Instrum. Meth. A*, vol. 465, p. 318, 2001.

[85] M. Tanabashi, et al., and (Particle Data Group), *Phys. Rev. D*, vol. 98, p. 010001, 2018.

[86] M. Ahmadi, B. X. R. Alves, C. J. Baker, W. Bertsche, E. Butler, A. Capra, C. Carruth, C. L. Cesar, M. Charlton, S. Cohen, R. Collister, S. Eriksson, A. Evans, N. Evetts, J. Fajans, T. Friesen, M. C. Fujiwara, D. R. Gill, A. Gutierrez, J. S. Hangst, W. N. Hardy, M. E. Hayden, C. A. Isaac, A. Ishida, M. A. Johnson, S. A. Jones, S. Jonsell, L. Kurchaninov, N. Madsen, M. Mathers, D. Maxwell, J. T. K. McKenna, S. Menary, J. M. Michan, T. Momose, J. J. Munich, P. Nolan, K. Olchanski, A. Olin, P. Pusa, C. O. Rasmussen, F. Robicheaux, R. L. Sacramento, M. Sameed, E. Sarid, D. M. Silveira, S. Stracka, G. Stutter, C. So, T. D. Tharp, J. E. Thompson, R. I. Thompson, D. P. van der Werf, and J. S. Wurtele, "Observation of the hyperfine spectrum of antihydrogen," *Nature*, vol. 548, p. 66, aug 2017. [Online]. Available: http://dx.doi.org/10.1038/nature23446

[87] M. Ahmadi, B. X. R. Alves, C. J. Baker, W. Bertsche, E. Butler, A. Capra, C. Carruth, C. L. Cesar, M. Charlton, S. Cohen, R. Collister, S. Eriksson, A. Evans, N. Evetts, J. Fajans, T. Friesen, M. C. Fujiwara, D. R. Gill, A. Gutierrez, J. S. Hangst, W. N. Hardy, M. E. Hayden, C. A. Isaac, A. Ishida, M. A. Johnson, S. A. Jones, S. Jonsell, L. Kurchaninov, N. Madsen, M. Mathers, D. Maxwell, J. T. K. McKenna, S. Menary, J. M. Michan, T. Momose, J. J. Munich, P. Nolan, K. Olchanski, A. Olin, P. Pusa, C. Ø. Rasmussen, F. Robicheaux, R. L. Sacramento, M. Sameed, E. Sarid, D. M. Silveira, S. Stracka, G. Stutter, C. So, T. D. Tharp, J. E. Thompson, R. I. Thompson, D. P. van der Werf, and J. S. Wurtele, *Nature*, vol. 548, no. 7665, pp. 66–69, Aug. 2017.

[88] P. Crivelli, D. Cooke, and M. W. Heiss, "Antiproton charge radius," *Phys. Rev. D*, vol. 94, p. 052008, Sep 2016. [Online]. Available: https://link.aps.org/doi/10.1103/PhysRevD.94.052008

[89] E. Widmann *et al.*, "Hyperfine spectroscopy of hydrogen and antihydrogen in ASACUSA," Proceedings of the 7th International Symposium on Symmetries in Subatomic Physics, Aachen, Germany, 10-15 Jun 2018, 2018, arxiv: 1809.00875.

[90] C. Smorra, S. Sellner, M. J. Borchert, J. A. Harrington, T. Higuchi, H. Nagahama, T. Tanaka, A. Mooser, G. Schneider, M. Bohman, K. Blaum, Y. Matsuda, C. Ospelkaus, W. Quint, J. Walz, Y. Yamazaki, and S. Ulmer, "A parts-per-billion measurement of the antiproton magnetic moment," *Nature*, vol. 550, p. 371, Oct. 2017. [Online]. Available: http://dx.doi.org/10.1038/nature24048

[91] D. Colladay and V. A. Kostelecký, "CPT violation and the standard model," *Physical Review D*, vol. 55, pp. 6760–6774, 1997.

[92] V. Kostelecký and N. Russell, "Data tables for Lorentz and CPT violation," *Review of Modern Physics*, vol. 83, no. 1, pp. 11–32, Mar. 2011.

[93] A. Kostelecky and N. Russell, "Data Tables for Lorentz and CPT Violation," arXiv:0801.0287, 2018 edition.

[94] R. Bluhm, V. Kostelecký, and N. Russell, "CPT and Lorentz tests in hydrogen and antihydrogen," *Physical Review Letters*, vol. 82, no. 11, pp. 2254–2257, 1999.

[95] M. Charlton, J. Eades, D. Horvath, R. Hughes, and C. Zimmermann, "Antihydrogen physics," *Physics Reports*, vol. 241, no. 2, pp. 65–117, 1994.

[96] G. Gabrielse, "Atoms made entirely of antimatter: two methods produce slow antihydrogen," *Adv. At. Mol. Opt. Phys*, vol. 50, p. 155, 2005.

[97] M. Hori and J. Walz, "Physics at cerns antiproton decelerator," *Progress in Particle and Nuclear Physics*, vol. 72, pp. 206 – 253, 2013. [Online]. Available: http://www.sciencedirect.com/science/article/pii/S0146641013000069

[98] M. Ahmadi, B. X. R. Alves, C. J. Baker, W. Bertsche, A. Capra, C. Carruth, C. L. Cesar, M. Charlton, S. Cohen, R. Collister, S. Eriksson, A. Evans, N. Evetts, J. Fajans, T. Friesen, M. C. Fujiwara, D. R. Gill, J. S. Hangst, W. N. Hardy, M. E. Hayden, E. D. Hunter, C. A. Isaac, M. A. Johnson, J. M. Jones, S. A. Jones, S. Jonsell, A. Khramov, P. Knapp, L. Kurchaninov, N. Madsen, D. Maxwell, J. T. K. McKenna, S. Menary, J. M. Michan, T. Momose, J. J. Munich, K. Olchanski, A. Olin, P. Pusa, C. . Rasmussen, F. Robicheaux, R. L. Sacramento, M. Sameed, E. Sarid, D. M. Silveira, D. M. Starko, G. Stutter, C. So, T. D. Tharp, R. I. Thompson, D. P. van der Werf, and J. S. Wurtele, "Observation of the 1s-2p lyman- transition in antihydrogen," *Nature*, pp. –, 2018. [Online]. Available: https://doi.org/10.1038/s41586-018-0435-1

[99] E. Widmann, J. Eades, R. S. Hayano, M. Hori, D. Horvath, T. Ishikawa, B. Juhazs, J. Sakaguchi, H. A. Torii, H. Yamaguchi, and T. Yamazaki, in *The Hydrogen Atom.* Springer, Berlin, Heidelberg, 2001, pp. 528–542.

[100] A. Mohri and Y. Yamazaki, "A possible new scheme to synthesize antihydrogen and to prepare a polarised antihydrogen beam," *Europhysics Letters*, vol. 63, p. 207, 2003.

[101] Y. Nagata and Y. Yamazaki, "A novel property of anti-Helmholz coils for in-coil syntheses of antihydrogen atoms: formation of a focused spin-polarized beam," *New Journal of Physics*, pp. 1–11, Aug. 2014.

[102] Y. Nagata, Y. Kanai, N. Kuroda, H. Higaki, Y. Matsuda, and Y. Yamazaki, *J. Phys.: Conf. Ser.*, vol. 635, no. 2, p. 022062, 2015.

[103] N. Kuroda, S. Ulmer, D. J. Murtagh, S. Van Gorp, Y. Nagata, M. Diermaier, S. Federmann, M. Leali, C. Malbrunot, V. Mascagna, O. Massiczek, K. Michishio, T. Mizutani, A. Mohri, H. Nagahama, M. Ohtsuka, B. Radics, S. Sakurai, C. Sauerzopf, K. Suzuki, M. Tajima, H. A. Torii, L. Venturelli, B. Wünschek, J. Zmeskal, N. Zurlo, H. Higaki, Y. Kanai, E. Lodi Rizzini, Y. Nagashima, Y. Matsuda, E. Widmann, and Y. Yamazaki, *Nat Commun*, vol. 5, Jan. 2014.

[104] C. Malbrunot, C. Amsler, S. A. Cuendis, H. Breuker, P. Dupre, M. Fleck, H. Higaki, Y. Kanai, B. Kolbinger, N. Kuroda, M. Leali, V. Mäckel, V. Mascagna, O. Massiczek, Y. Matsuda, Y. Nagata, M. C. Simon, H. Spitzer, M. Tajima, S. Ulmer, L. Venturelli, E. Widmann, M. Wiesinger, Y. Yamazaki, and J. Zmeskal, *Phil. Trans. R. Soc. A*, vol. 376, no. 2116, p. 20170273, Mar. 2018.

[105] M. Diermaier, C. B. Jepsen, B. Kolbinger, C. Malbrunot, O. Massiczek, C. Sauerzopf, M. C. Simon, J. Zmeskal, and E. Widmann, "In-beam measurement of the hydrogen hyperfine splitting and prospects for antihydrogen spectroscopy," *Nat Commun*, vol. 8, Jun. 2017.

[106] R. G. Greaves and C. M. Surko, "Inward transport and compression of a positron plasma by a rotating electric field," *Physical Review Letters*, vol. 85, no. 9, pp. 1883–1886, 2000. [Online]. Available: http://link.aps.org/doi/10.1103/PhysRevLett.85.1883

[107] N. Kuroda, H. A. Torii, Y. Nagata, M. Shibata, Y. Enomoto, H. Imao, Y. Kanai, M. Hori, H. Saitoh, H. Higaki, A. Mohri, K. Fujii, C. H. Kim, Y. Matsuda, K. Michishio, Y. Nagashima, M. Ohtsuka, K. Tanaka, and Y. Yamazaki, "Development of a monoenergetic ultraslow antiproton beam source for high-precision investigation," *Phys. Rev. ST Accel. Beams*, vol. 15, p. 024702, Feb 2012. [Online]. Available: https://link.aps.org/doi/10.1103/PhysRevSTAB.15.024702

[108] V. Chohan, C. Alanzeau, M. E. Angoletta, J. Baillie, D. Barna, W. Bartmann, P. Belochitskii, J. Borburgh, H. Breuker, F. Butin, M. Buzio, O. Capatina, C. Carli, E. Carlier, M. Cattin, T. Dobers, P. Chiggiato, L. Ducimetiere, T. Eriksson, S. Fedemann, T. Fowler, R. Froeschl, R. Gebel, N. Gilbert, S. Hancock, J. Harasimowicz, M. Hori, L. V. Jorgensen, R. Kersevan, D. Kuchler, J. M. Lacroix, G. LeGodec, P. Lelong, L. Lopez-Hernandez, S. Maury, J. Molendijk, B. Morand, A. Newborough, D. Nisbet, A. Nosych, W. Oelert, M. Paoluzzi, S. Pasinelli, F. Pedersen, D. Perini, B. Puccio, J. Sanchez-Quesada, D. Schoerling, L. Sermeus, L. Soby, M. Timmins, D. Tommasini, G. Tranquille, G. Vanbavinckhove, A. Vorozhtsov, C. Welsch, and T. Zickler, Eds., *Extra Low ENergy Antiproton (ELENA) ring and its Transfer Lines: Design Report*, ser. CERN Yellow Reports: Monographs. Geneva: CERN, 2014.

[109] S. P. Mller, A. Csete, T. Ichioka, H. Knudsen, U. I. Uggerhj, and H. H. Andersen, "Antiproton Stopping at Low Energies: Confirmation of Velocity-Proportional Stopping Power," *Physical Review Letters*, vol. 88, no. 19, p. 193201, Apr. 2002. [Online]. Available: https://link.aps.org/doi/10.1103/PhysRevLett.88.193201

[110] N. Kuroda, S. Ulmer, D. J. Murtagh, S. Van Gorp, Y. Nagata, M. Diermaier, S. Federmann, M. Leali, C. Malbrunot, V. Mascagna, O. Massiczek, K. Michishio, T. Mizutani, A. Mohri, H. Nagahama, M. Ohtsuka, B. Radics, S. Sakurai, C. Sauerzopf, K. Suzuki, M. Tajima, H. A. Torii, L. Venturelli, B. Wünschek, J. Zmeskal, N. Zurlo, H. Higaki, Y. Kanai, E. Lodi Rizzini, Y. Nagashima, Y. Matsuda, E. Widmann, and Y. Yamazaki, "A source of

antihydrogen for in-flight hyperfine spectroscopy," *Nat Commun*, vol. 5, p. 3089, 01 2014. [Online]. Available: http://dx.doi.org/10.1038/ncomms4089

[111] B. Kolbinger, C. Amsler, H. Breuker, M. Diermaier, P. Dupr, M. Fleck, A. Gligorova, H. Higaki, Y. Kanai, T. Kobayashi, M. Leali, V. Mckel, C. Malbrunot, V. Mascagna, O. Massiczek, Y. Matsuda, D. Murtagh, Y. Nagata, C. Sauerzopf, M. C. Simon, M. Tajima, S. Ulmer, N. Kuroda, L. Venturelli, E. Widmann, Y. Yamazaki, and J. Zmeskal, "Recent developments from asacusa on antihydrogen detection," *EPJ Web of Conferences*, vol. 181, 2018. [Online]. Available: https://doi.org/10.1051/epjconf/201818101003

[112] B. Kolbinger, "Machine Learning for Antihydrogen Detection in ASACUSA," Ph.D. dissertation. [Online]. Available: http://cds.cern.ch/record/2670395

[113] B. Radics, Y. Nagata, Y. Yamazaki, S. Ishikawa, N. Kuroda, Y. Matsuda, M. Anfreville, S. Aune, M. Boyer, F. Chateau, M. Combet, R. Granelli, P. Legou, I. Mandjavidze, S. Procureur, M. Riallot, B. Vallage, and M. Vandenbroucke, "The ASACUSA Micromegas Tracker: A cylindrical, bulk Micromegas detector for antimatter research," *Review of Scientific Instruments*, vol. 86, no. 8, p. 083304, Aug. 2015. [Online]. Available: http://aip.scitation.org/doi/full/10.1063/1.4927685

[114] S. Jonsell and M. Charlton, "Formation of antihydrogen beams from positron antiproton interactions," *New Journal of Physics*, vol. 21, no. 7, p. 073020, Jul. 2019.

[115] B. Radics, D. J. Murtagh, Y. Yamazaki, and F. Robicheaux, "Scaling behavior of the ground-state antihydrogen yield as a function of positron density and temperature from classical-trajectory Monte Carlo simulations," *Physical Review A*, vol. 90, no. 3, p. 032704, Sep. 2014. [Online]. Available: http://link.aps.org/doi/10.1103/PhysRevA.90.032704

[116] A. Soren Lindholt, "Positronium Formation and Cooling in Meso-Structured Silica Films," Ph.D. dissertation, Aarhus Univerity, 2015.

[117] C. Smorra, A. Mooser, K. Franke, H. Nagahama, G. Schneider, T. Higuchi, S. V. Gorp, K. Blaum, Y. Matsuda, W. Quint, J. Walz, Y. Yamazaki, and S. Ulmer, *International Journal of Mass Spectrometry*, vol. 389, pp. 10–13, Oct. 2015.

[118] "The production of collimated beams of o-Ps atoms using charge exchange in positron-gas collisions," vol. 20.

[119] B. Radics and Y. Yamazaki, *J. Phys. B: At. Mol. Opt. Phys.*, vol. 49, no. 6, p. 064007, 2016.

[120] R. Lundmark, C. Malbrunot, Y. Nagata, B. Radics, C. Sauerzopf, and E. Widmann, *J. Phys. B: At. Mol. Opt. Phys.*, vol. 48, no. 18, p. 184001, 2015.

[121] T. Wolz, C. Malbrunot, and et al., "Stimulated decay and formation of antihydrogen atoms," *in preparation*, 2019.

[122] R. Neumann, H. Poth, A. Winnacker, and A. Wolf, "Laser-enhanced electron-ion capture and antihydrogen formation," *Zeitschrift für Physik A Atoms and Nuclei*, vol. 313, no. 4, pp. 253–262, 1983.

[123] F. Yousif, P. Van der Donk, Z. Kucherovsky, J. Reis, E. Brannen, J. Mitchell, and T. Morgan, "Experimental observation of laser-stimulated radiative recombination," *Physical review letters*, vol. 67, no. 1, p. 26, 1991.

[124] M. Amoretti, C. Amsler, G. Bonomi, P. D. Bowe, C. Canali, C. Carraro, C. Cesar, M. Charlton, A. Ejsing, A. Fontana *et al.*, "Search for laser-induced formation of antihydrogen atoms," *Physical review letters*, vol. 97, no. 21, p. 213401, 2006.

[125] S. Federmann, "A spin-flip cavity for microwave spectroscopy of antihydrogen," mathesis, Universität Wien. Fakultät für Physik, 2012. [Online]. Available: http://othes.univie.ac.at/22584/

[126] C. Malbrunot, M. Diermaier, M. Simon, C. Amsler, S. A. Cuendis, H. Breuker, C. Evans, M. Fleck, B. Kolbinger, A. Lanz, M. Leali, V. Maeckel, V. Mascagna, O. Massiczek, Y. Matsuda, Y. Nagata, C. Sauerzopf, L. Venturelli, E. Widmann, M. Wiesinger, Y. Yamazaki, and J. Zmeskal, "A hydrogen beam to characterize the asacusa antihydrogen hyperfine spectrometer," *Nuclear Instruments and Methods in Physics Research Section A: Accelerators, Spectrometers, Detectors and Associated Equipment*, vol. 935, pp. 110 – 120, 2019. [Online]. Available: http://www.sciencedirect.com/science/article/pii/S0168900219305315

[127] S. Arguedas Cuendis, "Measuring the hydrogen ground-state hyperfine splitting through the π_1 and σ_1 transitions," M. thesis, Universität Wien. Fakultät für Physik, 2017. [Online]. Available: http://othes.univie.ac.at/22584/

[128] A. Lanz, "Hydrogen hyperfine structure measurements using the sigma- and pi1-transitions: Evaluation and correction," *Master Thesis*, 2019. [Online]. Available: http://cds.cern.ch/record/2686432

[129] M. A. Humphrey, D. F. Phillips, E. M. Mattison, R. F. C. Vessot, R. E. Stoner, and R. L. Walsworth, "Testing CPT and Lorentz symmetry with hydrogen masers," *Physical Review A - Atomic, Molecular, and Optical Physics*, vol. 68, no. 6, pp. 063 807/1–063 807/14, 2003.

[130] V. A. Kostelecký and A. J. Vargas, *Phys. Rev. D*, vol. 92, no. 5, p. 056002, Sep. 2015.

[131] C. Malbrunot, C. Amsler, S. Arguedas Cuendis, H. Breuker, P. Dupre, M. Fleck, H. Higaki, Y. Kanai, B. Kolbinger, N. Kuroda, M. Leali, V. Mäckel, V. Mascagna, O. Massiczek, Y. Matsuda, Y. Nagata, M. C. Simon, H. Spitzer, M. Tajima, S. Ulmer, L. Venturelli, E. Widmann, M. Wiesinger, Y. Yamazaki, and J. Zmeskal, "The asacusa antihydrogen and hydrogen program: results and prospects," *Philosophical Transactions of the Royal Society of London A: Mathematical, Physical and Engineering Sciences*, vol. 376, no. 2116, p. 20170273, 2018. [Online]. Available: http://rsta.royalsocietypublishing.org/content/376/2116/20170273

[132] F. Biraben, J. C. Garreau, L. Julien, and M. Allegrini, "A metastable hydrogen atomic beam: Construction and characteristics," *Review of Scientific Instruments*, vol. 61, no. 5, pp. 1468–1473, May 1990. [Online]. Available: http://aip.scitation.org/doi/abs/10.1063/1.1141154

[133] W. Vassen, C. Cohen-Tannoudji, M. Leduc, D. Boiron, C. I. Westbrook, A. Truscott, K. Baldwin, G. Birkl, P. Cancio, and M. Trippenbach, *Reviews of Modern Physics*, vol. 84, no. 1, pp. 175–210, Feb. 2012.

[134] C. Amsler, "Nucleon-antinucleon annihilation at LEAR," arXiv:1908.08455, 2019.

[135] H. S. Plendl, H. Daniel, T. von Egidy, T. Haninger, F. S. Hartmann, P. Hofmann, Y. S. Kim, H. Machner, G. Riepe, J. Jastrzebski, A. Grabowska, W. Kurcewicz, P. Lubinski, A. Stolarz, A. S. Botvina, Y. S. Golubeva, A. S. Iljinov, V. G. Nedorezov, A. S. Sudov, and K. Ziock, "Antiproton-nucleus annihilation at rest," *Physica Scripta*, vol. 48, no. 2, pp. 160–163, aug 1993.

[136] D. Polster, D. Hilscher, H. Rossner, T. von Egidy, F. J. Hartmann, J. Hoffmann, W. Schmid, I. A. Pshenichnov, A. S. Iljinov, Y. S. Golubeva, H. Machner, H. S. Plendl, A. Grochulska, J. Jastrzebski, W. Kurcewicz, P. Lubinski, J. Eades, and S. Neumaier, "Light particle emission induced by stopped antiprotons in nuclei: Energy dissipation and neutron-to-proton ratio," *Phys. Rev. C*, vol. 51, pp. 1167–1180, Mar 1995. [Online]. Available: https://link.aps.org/doi/10.1103/PhysRevC.51.1167

[137] E. Moser, H. Daniel, T. V. Egidy, F. Hartmann, W. Kanert, G. Schmidt, M. Nicholas, and J. Reidy, "Yields of residual nuclei after antiproton annihilation in 95mo and 98mo," *Physics Letters B*, vol. 179, no. 1, pp. 25 – 29, 1986. [Online]. Available: http://www.sciencedirect.com/science/article/pii/0370269386904296

[138] T. von Egidy, H. Daniel, F. J. Hartmann, W. Kanert, E. F. Moser, Y. S. Golubeva, A. S. Iljinov, and J. J. Reidy, "Yield of residual nuclei after antiproton annihilation in ba," *Zeitschrift für Physik A Atomic Nuclei*, vol. 335, no. 4, pp. 451–457, Dec 1990. [Online]. Available: https://doi.org/10.1007/BF01290193

[139] E. F. Moser, H. Daniel, T. Von Egidy, F. J. Hartmann, W. Kanert, G. Schmidt, E. S. Golubeva, A. S. Ilinov, M. Nicholas, and J. J. Reidy, "Residual Nuclei After Anti-proton Annihilation in Mo and Ho," *Z. Phys.*, vol. A333, pp. 89–105, 1989.

[140] S. Aghion, C. Amsler, A. Ariga, T. Ariga, G. Bonomi, P. Brunig, R. Brusa, L. Cabaret, M. Caccia, R. Caravita, F. Castelli, G. Cerchiari, D. Comparat, G. Consolati, A. Demetrio, L. D. Noto, M. Doser, A. Ereditato, C. Evans, R. Ferragut, J. Fesel, A. Fontana, S. Gerber, M. Giammarchi, A. Gligorova, F. Guatieri, S. Haider, A. Hinterberger, H. Holmestad, T. Huse, J. Kawada, A. Kellerbauer, M. Kimura, D. Krasnický, V. Lagomarsino, P. Lansonneur, P. Lebrun, C. Malbrunot, S. Mariazzi, V. Matveev, Z. Mazzotta, S. Mller, G. Nebbia, P. Nedelec, M. Oberthaler, N. Pacifico, D. Pagano, L. Penasa, V. Petracek, C. Pistillo, F. Prelz, M. Prevedelli, L. Ravelli, B. Rienaecker, O. RØhne, A. Rotondi, M. Sacerdoti, H. Sandaker, R. Santoro, P. Scampoli, M. Simon, L. Smestad, F. Sorrentino, G. Testera, I. Tietje, S. Vamosi, M. Vladymyrov, E. Widmann, P. Yzombard, C. Zimmer, J. Zmeskal, and N. Zurlo, "Measurement of antiproton annihilation on cu, ag and au with emulsion films," *Journal of Instrumentation*, vol. 12, no. 04, pp. P04 021–P04 021, apr 2017. [Online]. Available: https://doi.org/10.1088%2F1748-0221%2F12%2F04%2Fp04021

[141] E. Widmann, "Asacusa status report recent progress and plans for 2018," CERN, Geneva, Tech. Rep. CERN-SPSC-2018-003. SPSC-SR-226, Jan 2018. [Online]. Available: http://cds.cern.ch/record/2300138

[142] E. Widmann and M. Hori, "Asacusa status report recent progress and plans for ls2," CERN, Geneva, Tech. Rep. CERN-SPSC-2019-006. SPSC-SR-245, Jan 2019. [Online]. Available: https://cds.cern.ch/record/2654222

[143] T. Poikela, J. Plosila, T. Westerlund, M. Campbell, M. D. Gaspari, X. Llopart, V. Gromov, R. Kluit, M. van Beuzekom, F. Zappon, V. Zivkovic, C. Brezina, K. Desch, Y. Fu, and A. Kruth, "Timepix3: a 65k channel hybrid pixel readout chip with simultaneous ToA/ToT and sparse readout," *Journal of Instrumentation*, vol. 9, no. 05, pp. C05 013–C05 013, 2014.

[144] A. Obertelli, "PUMA: antiprotons and radioactive nuclei," CERN, Geneva, Tech. Rep. CERN-INTC-2018-023. INTC-M-018, Jun 2018. [Online]. Available: http://cds.cern.ch/record/2622466

[145] A. Boudard, J. Cugnon, J.-C. David, S. Leray, and D. Mancusi, "New potentialities of the Liège intranuclear cascade model for reactions induced by nucleons and light charged particles," *Phys. Rev. C*, vol. 87, p. 014606, Jan 2013. [Online]. Available: https://link.aps.org/doi/10.1103/PhysRevC.87.014606

[146] J. Cugnon and J. Vandermeulen, "Possibility of unusual antiproton annihilation on nuclei," *Physics Letters B*, vol. 146, no. 1, pp. 16–20, Oct. 1984. [Online]. Available: http://www.sciencedirect.com/science/article/pii/0370269384906336

[147] Cugnon, J. and Vandermeulen, J., "Antiproton and antilambda annihilations on several nucleons," *Physical Review C*, vol. 39, no. 1, pp. 181–191, Jan. 1989. [Online]. Available: https://link.aps.org/doi/10.1103/PhysRevC.39.181

[148] A. Abele, J. Adomeit, C. Amsler, C. Baker, B. Barnett, C. Batty, M. Benayoun, A. Berdoz, S. Bischoff, P. Blm, K. Braune, D. Bugg, T. Case, O. Cramer, K. Crowe, T. Degener, N. Djaoshvili, M. Doser, W. Dnnweber, D. Engelhardt, M. Faessler, P. Giarritta, R. Haddock, F. Heinsius, M. Heinzelmann, A. Herbstrith, M. Herz, N. Hessey, P. Hidas, C. Hodd, C. Holtzhauen, D. Jamnik, H. Kalinowsky, P. Kammel, J. Kisiel, E. Klempt, H. Koch, M. Kunze, U. Kurilla, M. Lakata, R. Landua, H. Matthy, R. McCrady, J. Meier, C. Meyer, L. Montanet, R. Ouared, K. Peters, B. Pick, M. Ratajczak, C. Regenfus, W. Roethel, R. Seibert, S. Spanier, H. Stck, C. Straburger, U. Strohbusch, M. Suffert, J. Suh, U. Thoma, M. Tischhuser, I. Uman, C. Vlcker, S. Wallis-Plachner, D. Walther, U. Wiedner, K. Wittmack, B. Zou, and . Zupani, "Observation of pontecorvo reactions with open strangeness: pd $\rightarrow \Lambda K^0$ and pd$\rightarrow \Sigma^0 K^0$," *Physics Letters B*, vol. 469, no. 1, pp. 276 – 286, 1999. [Online]. Available: http://www.sciencedirect.com/science/article/pii/S0370269399012253

[149] L. Kondratyuk and e. C. A. *et al.*. M.G. Sapozhnikov, "Physics at LEAR with low energy antiprotons," proceedings of the Fourth LEAR Workshop, Villars-sur-Ollon, Switzerland, 6-13 September, 1987, 1988.

[150] H. A. Torii, N. Kuroda, M. Shibata, Y. Nagata, D. Barna, M. Hori, A. Mohri, K. Komaki, and Y. Yamazaki, "Extraction of ultraslow antiproton beams and their physics application," *AIP Conference Proceedings*, vol. 796, no. 1, pp. 413–416, 2005. [Online]. Available: https://aip.scitation.org/doi/abs/10.1063/1.2130204

[151] N. Kuroda, H. A. Torii, Y. Nagata, M. Shibata, Y. Enomoto, H. Imao, Y. Kanai, M. Hori, H. Saitoh, H. Higaki, A. Mohri, K. Fujii, C. H. Kim, Y. Matsuda, K. Michishio, Y. Nagashima, M. Ohtsuka, K. Tanaka, and Y. Yamazaki, "Development of a monoenergetic ultraslow antiproton beam source for high-precision investigation," *Physical Review Special Topics - Accelerators and Beams*, vol. 15, no. 2, pp. 1–10, 2012.

[152] "ASACUSA Status Report; 2002 ed." CERN, Geneva, Tech. Rep. CERN-SPSC-2002-002. SPSC-M-674, Jan 2002. [Online]. Available: http://cds.cern.ch/record/533494

[153] "ECT* Trento: Workshop on antiproton-nucleus interactions and related phenomena," https://indico.ectstar.eu/event/41/, 2019, [Online].